The University of Maine
DigitalCommons@UMaine

Electronic Theses and Dissertations

Fogler Library

2003

A Surface Acoustic Wave Mercury Vapor Sensor

Reichl B. Haskell

Follow this and additional works at: http://digitalcommons.library.umaine.edu/etd

Part of the Electrical and Computer Engineering Commons

Recommended Citation

Haskell, Reichl B., "A Surface Acoustic Wave Mercury Vapor Sensor" (2003). *Electronic Theses and Dissertations*. 259.
http://digitalcommons.library.umaine.edu/etd/259

This Open-Access Thesis is brought to you for free and open access by DigitalCommons@UMaine. It has been accepted for inclusion in Electronic Theses and Dissertations by an authorized administrator of DigitalCommons@UMaine.

A SURFACE ACOUSTIC WAVE MERCURY VAPOR SENSOR

By

Reichl B. Haskell

B.S. University of Maine, 1997

A THESIS

Submitted in Partial Fulfillment of the

Requirements for the Degree of

Master of Science

(in Electrical Engineering)

The Graduate School

The University of Maine

August, 2003

Advisory Committee:

John F. Vetelino, Professor of Electrical and Computer Engineering, Advisor

Brian G. Frederick, Assistant Professor of Chemistry

Jeffrey C. Andle, Adjunct Professor of Electrical Engineering

A SURFACE ACOUSTIC WAVE MERCURY VAPOR SENSOR

By Reichl B. Haskell

Thesis Advisor: Dr. John F. Vetelino

An Abstract of the Thesis Presented
in Partial Fulfillment of the Requirements for the
Degree of Master of Science
(in Electrical Engineering)
August, 2003

An ST cut quartz 261MHz surface acoustic wave (SAW) delay line mercury vapor sensor was designed, fabricated, and tested. A gold sensing film was sputtered onto the delay path of a SAW device to collect mercury for detection. The sensor's ability to detect mercury was due to the strong interaction between gold and mercury, known as amalgamation. In the present work, a large number of gold films of various thicknesses were exposed to low concentrations of gaseous mercury. It was shown for thinner films (i.e. 25Å) the total amount of mercury that could be absorbed was limited; however, the response time for this film was fast and the response slope was linear with respect to mercury concentration. It was also shown that the slope responses for the thicker films (i.e. 500Å) were linear with respect to mercury concentration, but the response time and the response magnitude were significantly reduced. In the case of the thinner film, the decrease in frequency was attributed primarily to mass loading, while for the thicker film the changes in frequency were due to both mass loading and elastic stiffening. For the thick film the mass loading

response (frequency decrease) was offset by the elastic stiffening response (frequency increase). This resulted in a decrease in response slope resolution with respect to mercury concentration.

In conclusion the present work clearly indicates that a judicious choice of gold film thickness between these two thickness extremes results in a mercury sensor capable of very rapid detection of low mercury concentration levels with high resolution over a wide dynamic range.

ACKNOWLEDGMENTS

I would like to thank all the students and faculty at the Laboratory for Surface Science and Technology for all their support. I would especially like to thank my advisor, Dr. Vetelino, for the opportunity to pursue a master's degree and for helping me organize this thesis. I would also like to thank Dr. Frederick and Dr. Andle for their thorough reviews of this thesis.

I would like to thank the Maine Center for Technology and Transfer (CTT), the Department of Energy (DOE) and Sensor Research and Development Corporation (SRD) for the financial support during my masters work. I would also like to thank everyone at SRD for their technical assistance throughout this thesis. I would especially like to thank Josh Caron, Jeremy Hammond, Brent Marquis, Carl Freeman, Greg Grillo, Jason Ouellette and John Ouellette for their assistance throughout the years.

I would also like to thank Dan Stevens, Peter Morley, and especially Daryl Killip at Vectron International for giving me the motivation to complete my thesis.

Finally, I would like to thank my wife Shellie and my children Lyndsey, Ryan, and Leah for their patience and understanding.

TABLE OF CONTENTS

Chapter

LIST OF FIGURES

Chapter 1. INTRODUCTION

1.1. Background

Mercury originating from nuclear fuel and weapons production and disposal, fossil fuel combustion, waste incineration, mining operations, and a variety of industrial processes is a ubiquitous environmental pollutant found in air, soil, and groundwater. Mercury is particularly dangerous since it can bio-accumulate within the food chain and lead to irreversible neurological disorders and other health-related problems in humans. Furthermore, due to its teratogenic nature, mercury toxicity is particularly deleterious in unborn fetuses and young children [1-3].

The wide spread transportation of mercury is achieved most efficiently in its elemental form. Since mercury is an element, it can neither be created nor destroyed and elemental mercury that is released into the environment continuously cycles between the air, land, and water. Once released to the atmosphere, elemental mercury can travel thousands of miles away from emission sources and eventually find its way to coastal and inland waters by direct deposition or from watershed from terrestrial soils [1,4].

The most common forms of mercury found in water, soil, plants, and animals are inorganic mercury salts and organic forms of mercury (i.e. methylmercury). Nearly all of the mercury that works its way up the aquatic food web is methylmercury and since it is easily absorbed and not so easily removed, methylmercury is the most dangerous form of mercury in our environment.

Inorganic forms and elemental mercury are absorbed less efficiently and easily eliminated [1].

With the enactment of Title III of the 1990 Clean Air Act Amendments [5] considerable money and effort have been directed toward the development of mercury measurement techniques for stationary source emissions. Concern about the effects of mercury pollution on our environment, wildlife, and human population has driven a flurry of scientific activity into understanding the creation, transportation, control, and effects of mercury pollution from both industrial and commercial sources. Even with the completion of the EPA Mercury Study Report to Congress [1], uncertainty remains about the quantity, pathways, and effects of mercury in our environment.

Application of SAW mercury sensors as ambient, real-time monitors for elemental mercury could aid in the understanding of mercury transport from major emissions sources to the surrounding environment.

1.2. Previous Work on Mercury Microsensors

Current techniques that are used to detect mercury require a variety of elaborate separation strategies in conjunction with chromatographic, electrochemical or spectroscopic methods [6-15]. Although these techniques are sensitive (0.001pptr to 5ppb Hg), they are expensive, bulky, and inappropriate for portable, ambient monitoring; typically samples must be collected and shipped to a centralized laboratory or processing facility for analysis.

The most relevant work that has been done which might lead to a portable, ambient mercury sensor has utilized chemiresistive, resonant microcantilever, or acoustic wave technology. McNerney et al [16] demonstrated that the resistance of a thin gold film changes upon exposure to mercury due to the formation of a mercury-gold amalgam. This type of chemiresistive device utilizes a thin gold film typically shaped into a resistive serpentine pattern. (Figure 1.1) As mercury amalgamates with the gold it will cause a corresponding change in the resistance of the serpentine pattern. The rate of change of the resistance is indicative of the concentration of mercury being analyzed. McNerney's work later led to a commercial sensor produced by Jerome Instruments [17].

Bristow [18] and, later, other investigators [19-25] demonstrated that a gold-coated AT cut thickness shear mode (TSM) acoustic wave resonator (Figure 1.2a) could be used to detect mercury. A TSM device, more commonly known as a quartz crystal microbalance (QCM), is a thin disk of AT-cut quartz with faces typically metallized with gold.

Being piezoelectric, AT-cut quartz exhibits a unique coupling between its mechanical and electrical domains. When a voltage is applied across the thickness of the AT-cut crystal, it will experience a mechanical shear deformation. The maximum shear displacement occurs at the crystal faces (Figure 1.2b), making the surface of the TSM sensitive to mechanical perturbations such as mass loading, viscosity, and elasticity. Typically, an oscillator circuit is used to electrically excite the TSM resonator at either its fundamental resonant frequency or at one of its overtones.

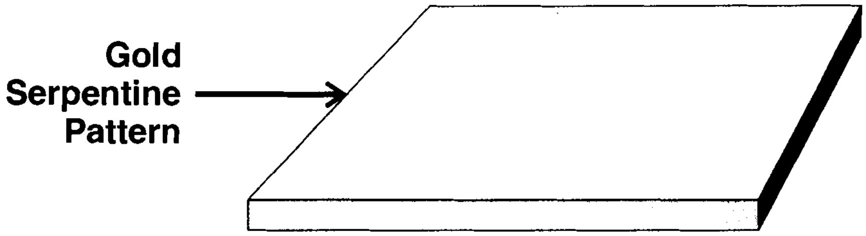

Figure 1.1 Illustration of a chemiresistive mercury sensor.

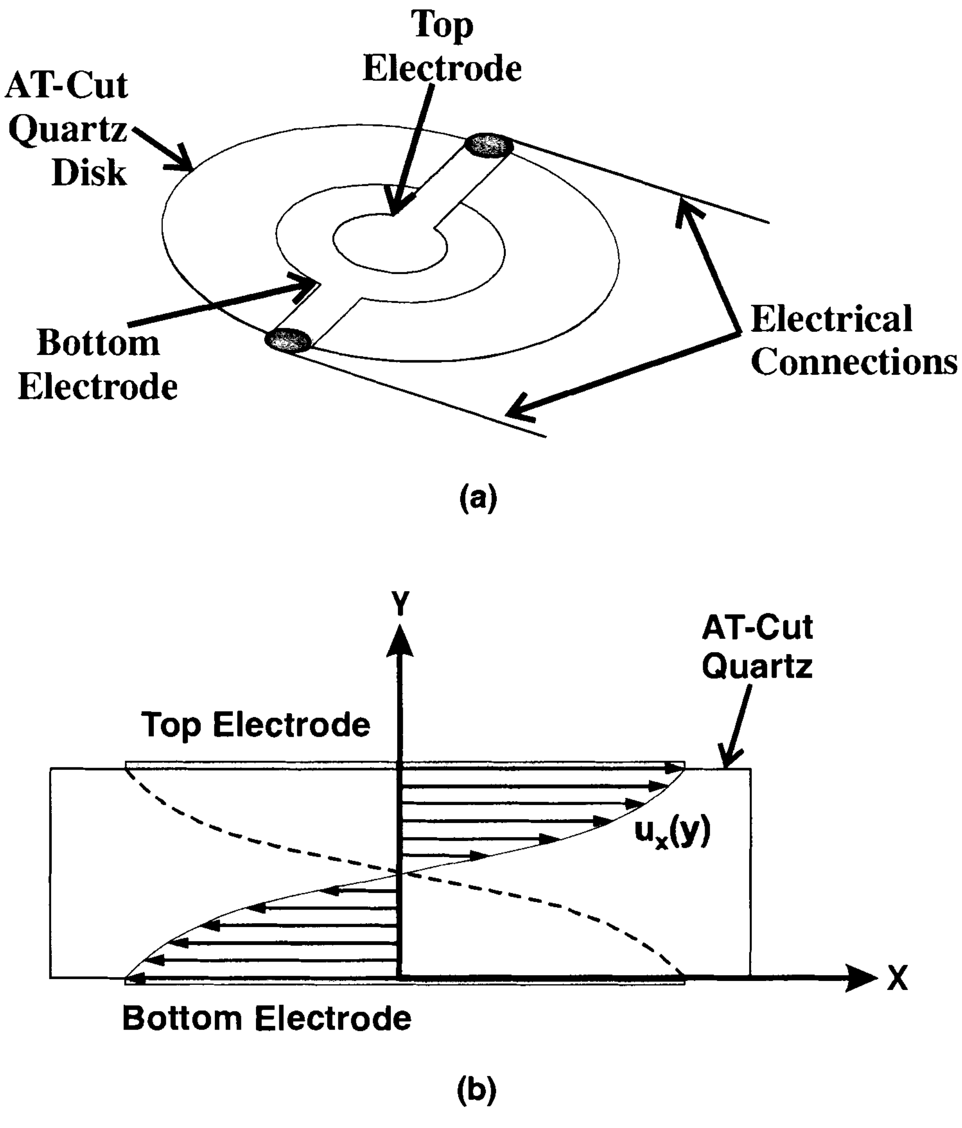

Figure 1.2 Thickness Shear Mode (TSM) mercury sensor. a) Illustration of a TSM resonator. b) Side view of the displacement profile throughout the thickness of the TSM device.

A TSM device with gold electrodes is an ideal candidate for a mercury detector. When mercury amalgamates with the gold, the added mass will cause the oscillation frequency of the device to decrease. The rate of change of the oscillation frequency is a function of the mercury concentration.

Thundat et al [26] demonstrated that a resonating gold-coated microcantilever could be used to detect low mercury concentrations (Figure 1.3). Depending on the placement of the gold film, two different modes of operation were reported. When the gold film was placed onto the silicon nitride microcantilever tip (Figure 1.3), exposure to mercury resulted in a mass loading response where the resonant frequency of the oscillating microcantilever decreased. The rate of change of the oscillation frequency was a function of the mercury concentration. When the gold film was placed onto the whole microcantilever (Figure 1.4), including where the legs attached to the chip base, exposure to mercury resulted in a bulk elastic stiffening response where the microcantilever oscillation frequency increased due to an increasing microcantilever spring constant. The change in the spring constant was caused by the changing bulk elastic properties of the gold film when exposed to mercury.

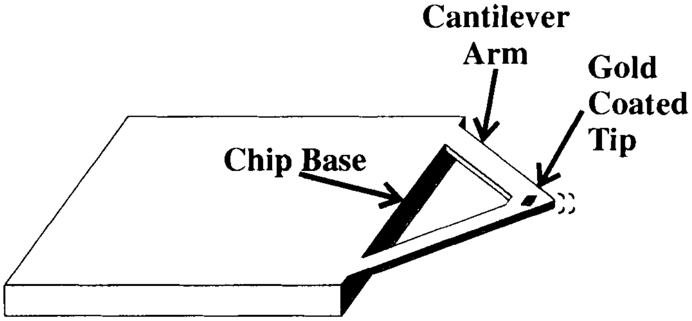

Figure 1.3 Illustration of a microcantilever mercury sensor with a gold coated tip.

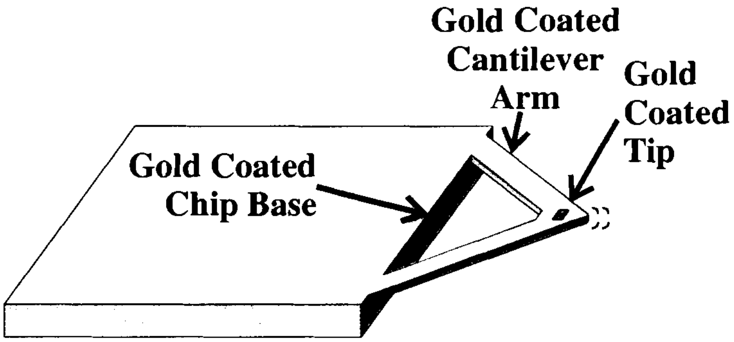

Figure 1.4 Illustration of a microcantilever mercury sensor with a gold coated arm and tip for bulk elasticity based measurements.

The rate of change of the increasing resonant frequency was a function of the mercury concentration. For the thickness range of the gold films used in that study, 200 to 500 Å, the thicker films resulted in larger responses due to bulk elastic stiffening.

Sauberlich et al [27] proposed and patented a design for a surface acoustic wave (SAW) based sensor for mercury, but never actually built or tested it. Similar work done by Andle et al in the area of aqueous mercury detection [28-31] led to the work done by Caron et al [32] who showed the first experimental proof that a SAW delay line coated with a gold film could be utilized for the detection of gaseous mercury. Further work done by Haskell et al [33], the same work presented in this thesis, demonstrated the effects of film thickness on the response of the SAW mercury sensor.

The SAW mercury sensor consists of a thin piece of piezoelectric substrate, on top of which, a pair of aluminum interdigital transducers (IDTs) are fabricated. The arrangement of the SAW structure has an input IDT, a delay path and an output IDT (Figure 1.5). Due to its stability at room temperature, ST-cut quartz is typically used for low temperature mercury detection. Similar to the

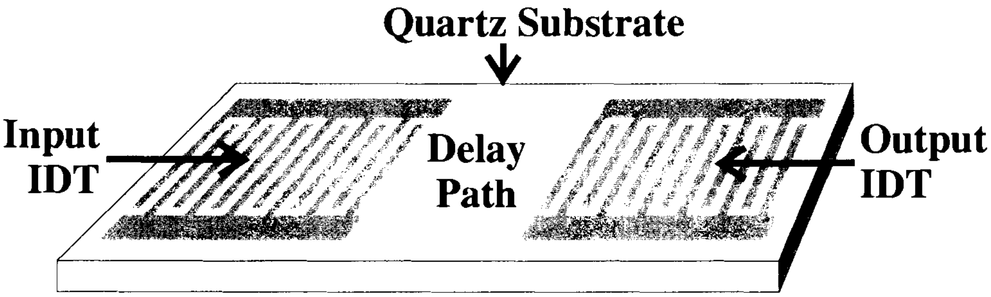

Figure 1.5 Illustration of a SAW delay line.

TSM device, a voltage applied to the input transducer will cause a mechanical deformation (Figure 1.6a). Instead of a shear deformation, a vertically polarized deformation will occur, causing a mechanical surface wave to travel from the input IDT, across the delay path to the output IDT where it gets converted back to an electrical signal (Figure 1.6b and Figure 1.6c).

Typically, the SAW is set up in an oscillator configuration where the output is amplified and fed back to the input. As long as the closed loop gain is greater than one and the phase shift around the loop is a multiple of 2π, then a standing surface acoustic wave will be generated where the resonance frequency is determined by the velocity of the surface wave in the quartz substrate and the periodic spacing of the IDTs.

The application of the SAW delay line as a mercury sensor is achieved with the placement of a thin gold film in the delay path. (Figure 1.7) When exposed to mercury, mechanical perturbations in mass and bulk elasticity will cause the velocity of the propagating wave to decrease or increase, causing a corresponding change in the oscillation frequency. The rate of change of the oscillation frequency can be correlated to the mercury concentration.

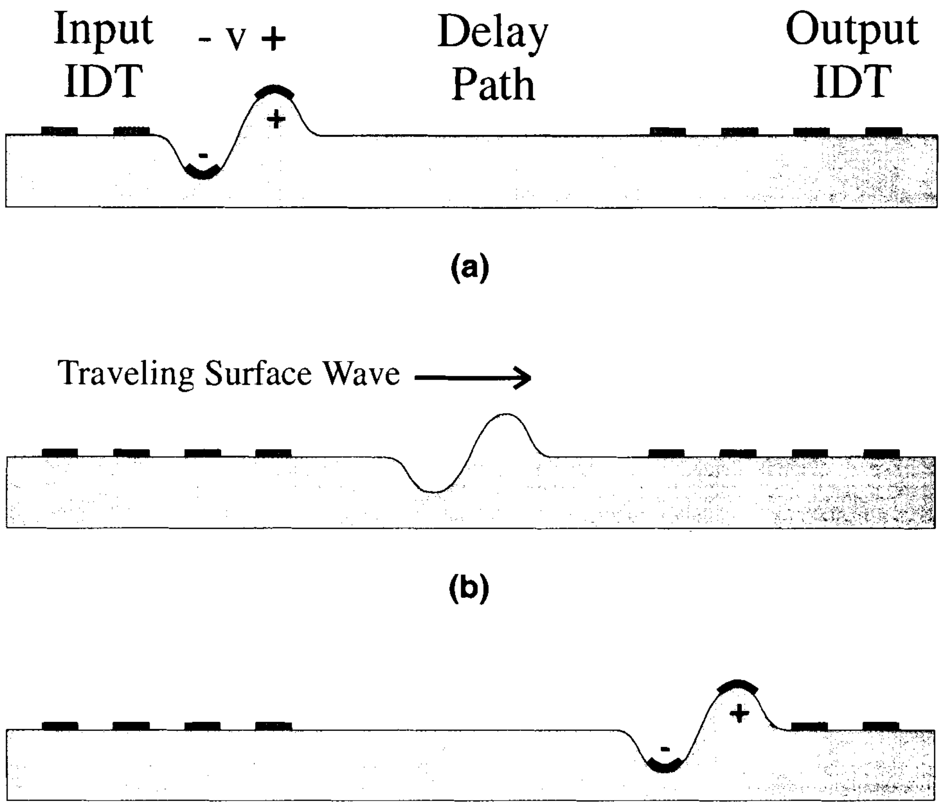

(a)

(b)

(c)

Figure 1.6 Side view illustration of a SAW delay line. a) Application of a voltage on the input IDT. b) Surface wave traveling across the delay path. c) Surface wave being received by the output IDT.

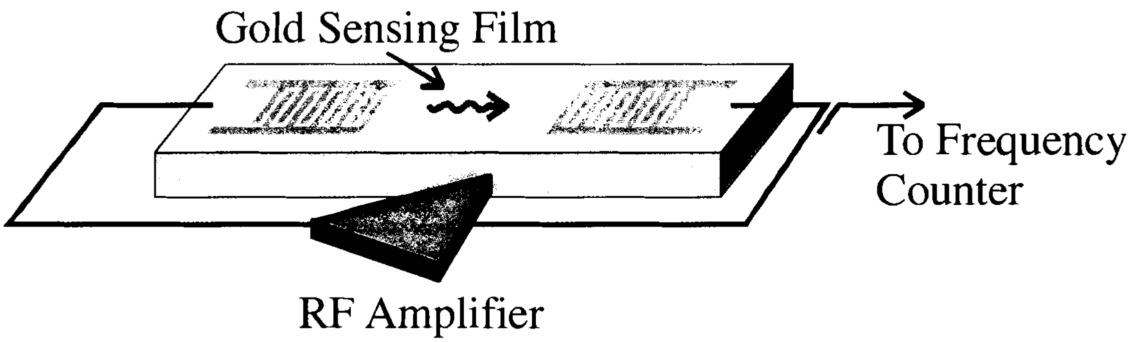

Figure 1.7 Illustration of a single delay line SAW mercury sensor setup in an oscillator configuration.

There are many advantages and disadvantages associated with these mercury microsensors when compared to the traditional spectroscopic techniques.

One major disadvantage is that microsensors tend to be less sensitive, but only because of their mode of operation. Many of the spectroscopic techniques report ultra low sensitivity [15], but this is usually achieved by pre-concentrating the mercury onto a gold trap. After some time, the trap is then heated and purged with an inert gas into the instrument where the liberated mercury can be quantified. The microsensors, on the other hand, are continuously sampling the ambient mercury levels in real time and thus the detection limit has some finite value. If the microsensors were used in conjunction with a gold trap, there is a possibility that their detection limits could be much lower.

Another disadvantage associated with microsensors has to do with the use of a gold film as a mercury collector. The adsorption of mercury onto the gold film is an integrating process where essentially all the mercury that comes into contact with the gold will stick to it indefinitely, until the gold film becomes saturated. At this point, the sensor needs to be heated to drive off the mercury. This down time associated with the cleaning process can be circumvented with the use of multiple sensing elements. Since the size of the sensing element is of the order of millimeters, the extra space taken up by additional sensors is negligible.

The final and most critical disadvantage associated with microsensors has to do with the selectivity of the gold film as a mercury collector in the presence of hydrogen sulfide. McNerney, et al [16] indicated that the thin gold film sensor responded almost as well to hydrogen sulfide as it did to mercury. In fact, Jerome Instruments sells a hydrogen sulfide detector based on the same gold film architecture as their mercury detector [17].

Advantages of microsensors are the overall size, cost, and power consumption associated with the instrument. All of the microsensors discussed are fabricated in batch quantities using standard semiconductor processing techniques. Essentially, as the number of devices per batch increases, the cost per device will go down. With the exception of the microcantilever, standard electronic packaging exists to house the various microsensors. All the support electronics and intelligence can be fabricated on small printed circuit boards and the overall instrument size can be miniaturized into a portable, hand-held instrument that will cost thousands of dollars less than their competing spectroscopic competitors.

1.3. Purpose of the Analysis

The purpose of this thesis was to develop a SAW-based gaseous mercury detector and to demonstrate its ability to detect mercury. In order to achieve this goal, a great deal of engineering development, fabrication, and testing was necessary.

First, a large number of sensor modules (i.e. dual delay line SAW chip, heater, RTD, oscillator circuits, and gas chamber) needed to be fabricated and fully characterized. In addition, temperature control support electronics were designed, assembled, and characterized to give calibration curves that could be used by a test computer to precisely control the temperature.

In order to fully characterize the mercury sensor's ability to detect mercury, a mercury delivery system and corresponding control circuitry for interfacing with a computer needed to be designed, built, and calibrated. Preliminary testing revealed the SAW device was sensitivity to pressure fluctuations caused by the valve switching in the mercury delivery system thus a new sampling method had to be developed.

Finally, once all various parts of the experiment were in place, the sensors were tested and fully characterized upon exposure to low level concentrations of gaseous mercury.

1.4. Organization

This thesis contains five chapters of which the Introduction is the first. Chapter 2 explains the theory of operation of the SAW mercury sensor. Beginning with section 2.1, the operation of a SAW delay line is presented. Section 2.2 focuses on the experimental SAW device and the conditions necessary to create a SAW delay line oscillator. Section 2.3 discusses the gold film as a sensing layer followed by section 2.4 which presents a simple model for the mechanical perturbation effects encountered by the gold-coated SAW device.

Chapter 3 gives an explanation of the experimental setup used to evaluate the SAW mercury sensor. Section 3.1 gives a brief overview of chapter 3, while section 3.2 describes the design of a mercury delivery system used to evaluate the SAW mercury sensor. Section 3.2 also discusses the sampling system used to deliver the mercury gas and how it can improve the sensor response. Section 3.3 covers the packaging of the SAW sensor. It details the layout of the SAW sensing element, the heater, the resistive thermal device (RTD), oscillator circuits, and gas chamber. Section 3.4 details the design of the oscillator circuit. Section 3.5 explains the microheater and support circuitry, while section 3.6 discusses the RTD and temperature measurement circuitry. Section 3.7 concludes with the data acquisition and control.

Chapter 4 presents the results of the testing on the SAW mercury sensor and demonstrates the effect of the gold film thickness on the sensor response. Section 4.1 defines the testing procedure used to evaluate all the SAW mercury sensors. Section 4.2 examines the observed response magnitude and slope as a function of the gold film thickness. Section 4.3 presents the response magnitude and slope as a function of concentration and section 4.4 is a discussion of the results.

Finally chapter 5 summarizes the thesis, provides conclusions, and presents some possible future research directions.

Chapter 2. THEORY OF OPERATION OF THE MERCURY SENSOR

This chapter explains the theory of operation of the SAW mercury sensor. The generation and propagation of a simple SAW is reviewed and the layout of the split finger design and its advantages are discussed. The experimental SAW delay line is presented and the conditions required for oscillation are explained. The use of a gold film as a sensing element is then discussed. Finally, a simple model explaining the gold film/mercury interaction and its effect on SAW velocity is presented.

2.1. The SAW Delay Line

A simple SAW delay line with uniform transducers is shown in Figure 2.1. The delay line consists of an input interdigital transducer (IDT), a delay path and an output interdigital transducer (IDT). When a sinusoidal voltage is applied to the input IDT, a spatially varying electric field is generated which is determined by the periodic spacing of the IDT structure. This in turn produces a mechanical

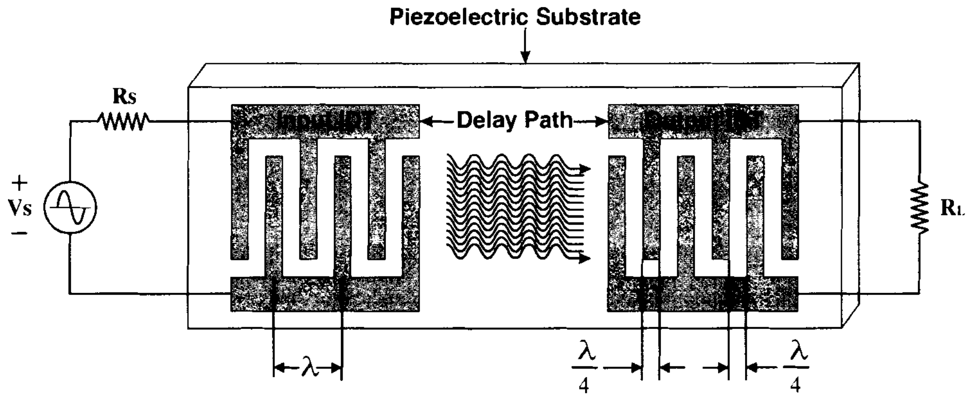

Figure 2.1 An illustration of a simple delay line structure.

displacement resulting in a surface wave being propagated from the input IDT, across the delay path to the output IDT where it gets converted back to an electrical signal. The wavelength of the SAW is determined by the IDT spacing (Figure 2.1) and the velocity is determined by the piezoelectric substrate and orientation. Since the wavelength and the velocity of the SAW are fixed, the design frequency of the SAW is determined by

$$f_{SAW} = \frac{v_{saw}}{\lambda} \qquad (2.1)$$

where v and λ are the velocity and the wavelength of the propagating SAW, respectively.

In order for there to be efficient coupling of electrical energy into mechanical energy, the frequency of the sinusoidal voltage should be close to the design frequency of the SAW. Signals that are not close to the design frequency get attenuated, resulting in very little signal being received at the output. Signals that are close to the design frequency are efficiently coupled into mechanical energy, propagated across the delay path and converted back into electrical energy with very little loss.

In reality, the simple IDT is a bidirectional structure which means that the generated surface waves will propagate in both directions away from the input IDT. Therefore, one half of the input power is propagated across the delay path, while the other half of the input power is propagated toward the end of the substrate. This results in a ½ power loss (3dB) per IDT or a total of 6dB insertion loss for a simple IDT delay line structure.

Other second-order effects can cause additional losses and/or create noise in the frequency response of the SAW delay line [34-35]. One of the most significant of these effects is called the triple-transit response. When a surface wave travels across the delay path, the output transducer can produce a reflected wave, which travels back across the delay path. This reflected wave can then be reflected once again by the input IDT where it propagates across the delay path to the output IDT. The reflected wave thus travels across the substrate surface three times before it gets converted back into an electrical signal by the output IDT. This triple-transit effect can result in significant rippling in the frequency amplitude and phase response.

One way to reduce this triple-transit response is to design the electrode structure to cancel out reflections. The electrode structure utilized in this thesis work accomplishes this with a split-finger transducer, also called a double-electrode transducer, shown in Figure 2.2 .

The split-finger transducer utilizes pairs of shorted electrodes that are $\lambda/8$ wide with a $\lambda/8$ spacing in between them. The uniqueness of this structure is in the way that reflected surface waves from a pair of shorted electrodes will cancel each other out. The electrically shorted fingers are 90° apart in phase for a traveling surface wave. When an incident wave travels across the first finger of the shorted pair, part of the wave is reflected and travels in the opposite direction. When the incident wave continues, traveling a distance of 90° in phase to the second finger of the shorted pair, a little bit more of the wave is reflected. The second reflected wave has to travel an additional 90° in phase to be in the

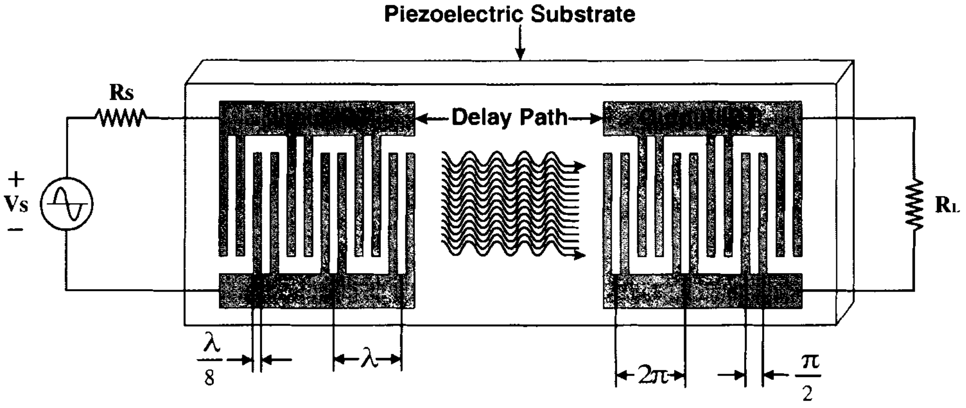

Figure 2.2 Split-finger transducer SAW delay line.

same location as the first reflected wave, but now the second reflected wave is 180° out of phase with the first reflected wave. The two reflected waves will cancel each other resulting in a significant reduction of the triple-transit response.

2.2. The Experimental SAW Delay Line Oscillator

The SAW sensing element used for this thesis work was originally designed by Dr. Jeffrey C. Andle for Sensor Research and Development Corp. The structure is a 261 MHz split-finger dual delay line structure fabricated on a 0.5 mm thick ST-quartz substrate (Figure 2.3). There are two delay lines, one of which is left bare and is typically used as a reference. The other delay line is coated with a 0.050" (~106λ) wide gold sensing film. Electrical contacts parallel to the delay path allow the measurement of the gold film conductivity.

For a 261 MHz ST-quartz SAW delay line, the acoustic wavelength is approximately 12μm. For a split-finger transducer with a 50% finger width to space ratio, this corresponds to 1.5μm line widths and spaces. Each IDT is

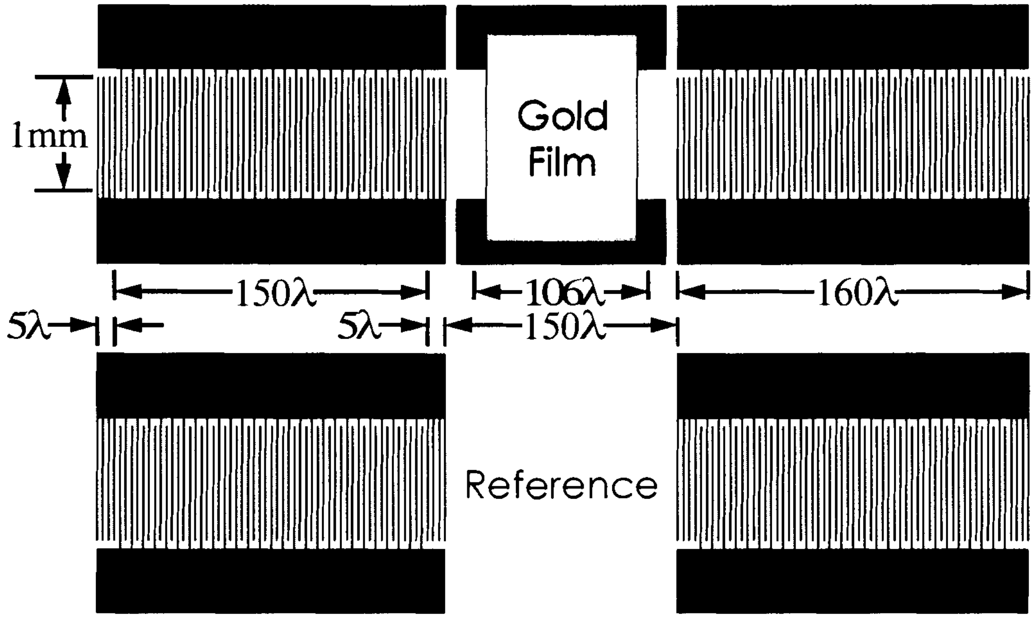

Figure 2.3 261MHz SAW dual delay line sensing element design parameters.

160λ wide, but 5λ on each end of the IDT are guard electrodes to reduce end effects [34]. The delay path is 150λ wide and the acoustic aperture is 1mm wide.

Figure 2.4 shows the frequency response of a 261MHz split-finger delay line. As shown, the delay line has a 3dB bandwidth slightly less than 1 MHz with a little over 2π radians of phase shift. Depending on the gold film thickness and the quality of the SAW device, insertion losses ranging from 13 to 16dB were typically encountered.

The simplest way to set up the SAW delay line is to place it in a loop with an amplifier to create an oscillator configuration. Two conditions must be met in order for the delay line to oscillate. First, the closed loop gain must be greater than or equal to one. This is easily accomplished by setting the amplifier gain slightly greater than the loss at the center frequency of the device. This will limit the oscillation frequency to the vicinity of the SAW design frequency.

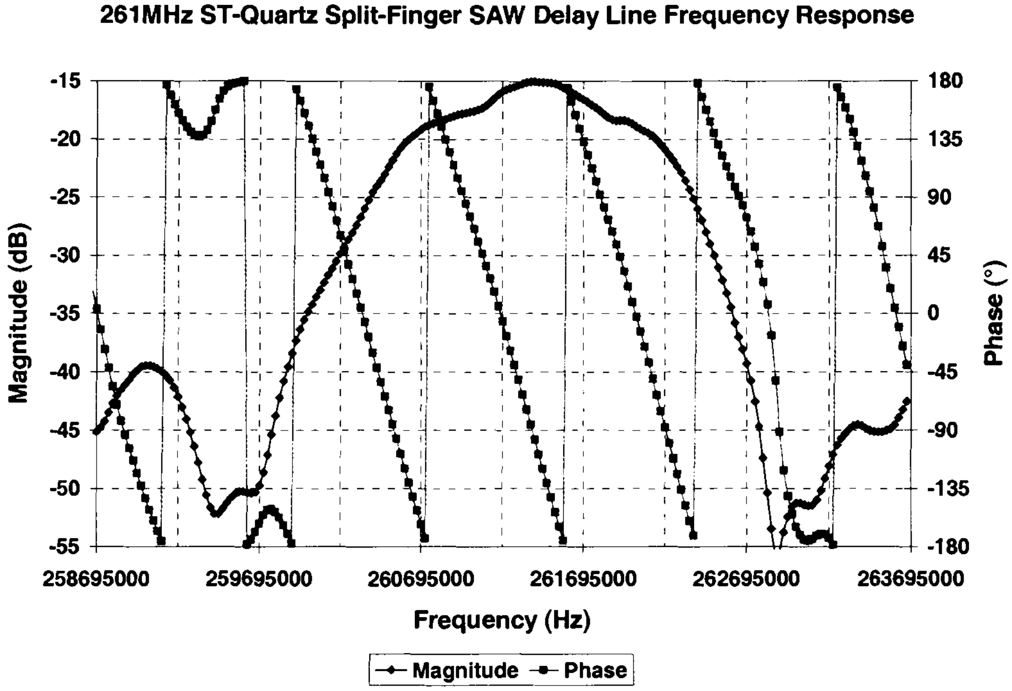

Figure 2.4 Measured Frequency Response of a 261MHz Split-Finger SAW Delay Line.

The second condition requires the total phase shift around the loop to be a multiple of 2π. Since, the phase shift through the amplifier, components, and traces is fixed, the oscillation frequency will be determined by whatever phase is necessary to make the total loop phase a multiple of 2π. By carefully setting the amplifier gain and component phase, the circuit can be made to oscillate at only one single frequency.

2.3. The Gold Film as a Sensing Layer

The SAW has been shown to be sensitive to both electrical and mechanical properties of a sensing film [36-37]. Changes in conductivity, mass, and elasticity will cause a corresponding change in the oscillation frequency of a

SAW delay line oscillator. For the case of a metal sensing layer, the electrical properties of the film can be neglected since the conductivity of the metal film will be well out of the range of sensitivity of the SAW device [38]. For the gold films utilized in this thesis, the resistances ranged from 8 to 500mΩ for the film dimensions shown in the previous section.

The SAW mercury sensor's ability to detect mercury is due to the strong interaction between the gold film and mercury, known as amalgamation. Upon sorption of mercury onto and into the gold film, perturbations in the film mass and viscoelastic properties induce corresponding changes in the propagation of the SAW. In general, mass accumulation of mercury onto and into the gold film will result in a corresponding decrease in the oscillation frequency, while increases in the stiffness of the mercury/gold amalgam will result in increases in oscillation frequency.

For the mass loading scenario, the amount of observed frequency shift will depend mainly on the adsorption of mercury onto the surface area of the gold film. We can calculate the amount of expected frequency shift for a monolayer of mercury sticking to the surface of the gold sensing film by assuming that the mercury atoms are stacked side by side on the surface of a flat gold film with no surface morphology.

The diameter and area of one mercury atom are $d = 342 \cdot 10^{-9} mm$ and $a = 1.17 \cdot 10^{-13} mm^2$, respectively. The total number of mercury atoms in 1mm^2 of surface area is then found by dividing 1mm^2 of surface area by the area of one mercury atom.

$$\#\,atoms = \frac{1mm^2}{1.17 \cdot 10^{-13} mm^2} = 8.55 \cdot 10^{12} atoms$$

The number of Hg atoms/mm^2 is then $A_{Hg} = 8.55 \cdot 10^{12} atoms / mm^2$ and the mass of Hg/mm^2, M_{Hg}, can then be found by

$$M_{Hg} = \frac{A_{Hg} \cdot MW_{Hg}}{N_a}, \tag{2.2}$$

where MW_{Hg} is the molecular weight of mercury and N_a is Avagadro's number. Doing the calculation we get $M_{Hg} = 2.85 ng / mm^2$.

The mass sensitivity, S_m, for an X-propagating ST-quartz SAW delay line is reported to be $S_m = 0.132 \cdot f_0^2$ in units of $Hz \cdot mm^2 / ng$ [39], where f_0 is design frequency of the SAW in units of MHz. The expected mass loading frequency shift, Δf_m, is then given by,

$$\Delta f_m = -\kappa \cdot S_m \cdot M_{Hg}, \tag{2.3}$$

where κ is the ratio of the gold film width, W_{film}, over the IDT center-to-center distance, W_{center}. As shown in Figure 2.3 of the previous section $W_{film} = 106 \cdot \lambda$ and $W_{center} = 310 \cdot \lambda$ gives us a value of $\kappa = 0.342$ and an expected frequency shift of $\Delta f_m = -8764 Hz = 33.6 ppm$. For the gold sensing films utilized in this thesis work, frequency shifts ranging from 6,000Hz (23ppm) to 12,000Hz (46ppm) were observed.

For the elastic stiffening scenario, the amount of increasing frequency shift will depend on the gold film thickness. Work done by D'Amico et al [40] demonstrated the significance of palladium metal film thickness on the amount of observed elastic stiffening response to hydrogen in a nitrogen carrier gas. Using a 76MHz Pd coated YZ-$LiNbO_3$ delay line operated at room temperature; they showed that the frequency change was dominated by elastic stiffening and had a quasi-exponential relationship with respect to the Pd sensing film thickness. For a 1% H_2 in N_2 concentration, Pd sensing film thicknesses of 1900, 3800, and 7600Å resulted in shifts in frequency of 14, 25, and 120ppm, respectively. Comparing this to an equivalent ST-quartz SAW delay line and noting that the coupling coefficient is approximately 100X less results in expected frequency shifts of 0.14, 0.25, and 1.2ppm, respectively for an ST-quartz hydrogen sensor.

Comparing this to the mercury responses presented in this thesis (23 to 46ppm), this doesn't seem like a significant amount of response due to stiffening, but it is speculated that the mercury/gold interaction will result in much greater elastic stiffening especially for the thicker gold sensing films. Unfortunately, literature describing the elastic properties of mercury/gold amalgam as a function of mercury concentration is difficult to find, but knowing that mercury has been utilized in silver-based dental amalgam alludes to the potential for significant elastic stiffening of mercury as it forms an alloy with the gold sensing film.

If this is the case then the net sensor response will be a superposition of two very different response mechanisms, one due to mass loading and another due to elastic stiffening. For both thin and thick films the response will be due mostly to mass loading, while for the thicker range of films presented in this thesis, the response will be a superposition of mass loading and elastic stiffening.

2.4. A Simple Model for Mechanical Effects

The behavior of the SAW mercury sensor can be modeled using simplified perturbation theory [36-38]. This method results in a simple closed-form expression describing SAW frequency fluctuations due to perturbations of the mechanical and electrical properties of an overlay film.

In the present case, it can be assumed that electrical perturbations to the highly conductive gold film have a negligible effect on the device frequency. Mechanical perturbations, on the other hand, including changes in film mass and elasticity, can have a significant impact. The fractional change in oscillation frequency due to mass and elasticity perturbations can be expressed using the Tiersten formula [41],

$$\frac{\Delta f}{f} = -\kappa f h\left[k_1\left(\rho - \frac{\mu}{v_0^2}\right) + k_2\rho + k_3\left(\rho - \frac{4\mu}{v_0^2}\frac{\lambda+\mu}{\lambda+2\mu}\right)\right] \qquad (2.4)$$

where κ is the fractional coverage of the gold film over the IDT center-to-center distance, f is the nominal operating frequency, h is the film thickness, ρ is the film density, k_i are the normalized particle velocities in the x_i direction, v_0 is the nominal SAW velocity, and λ and μ are the Lamé constants of the film. Examining the equation closely, one can see that the mass-induced frequency variations are embodied in the ρ terms, while the elasticity-induced changes are embodied in the terms containing λ and μ.

It is apparent from Equation 2.4 that increases in film mass result in a decrease in oscillation frequency, while increases in mechanical stiffness result in the opposite behavior. In the case of mercury amalgamation to a thin gold film, both of these situations arise. However, the interaction can be modeled as two parallel regions, the film surface where mass loading dominates, and the bulk where elasticity effects are much more pronounced.

It's worth noting that since mass loading is dependent on the available surface area, the amount of observed mass loading will change as the available surface area changes with respect to the gold film thickness. It has been pointed out that the shape of the gold islands as the film thickness approaches a continuous gold film is most likely hemispherical in shape [42-44]. If this is the case, then the available surface area will not be a linear function of the gold film thickness as the gold film becomes continuous. This is shown pictorially in Figure 2.5.

In the first case, (A), the film is so thin that the cohesive gold forms hemispherical "islands", rather than a continuous thin film. Case (B) shows a film which is maximized for surface area, but not quite continuous. This thickness will be denoted as $h_{\max}$. Case (C) shows a film which is just continuous with a slightly reduced surface area. This thickness will be denoted as h_c. Case (D) shows a film which is very continuous with the surface area much less than that of $h_{\max}$. The surface of case (D) is relatively smooth compared to that of the non-continuous films. Finally, (E) shows a much thicker continuous gold film with approximately the same surface area and smoothness as (D).

A plot of the available gold film surface area as a function of the gold film thickness is shown in Figure 2.6. For extremely thin films that form

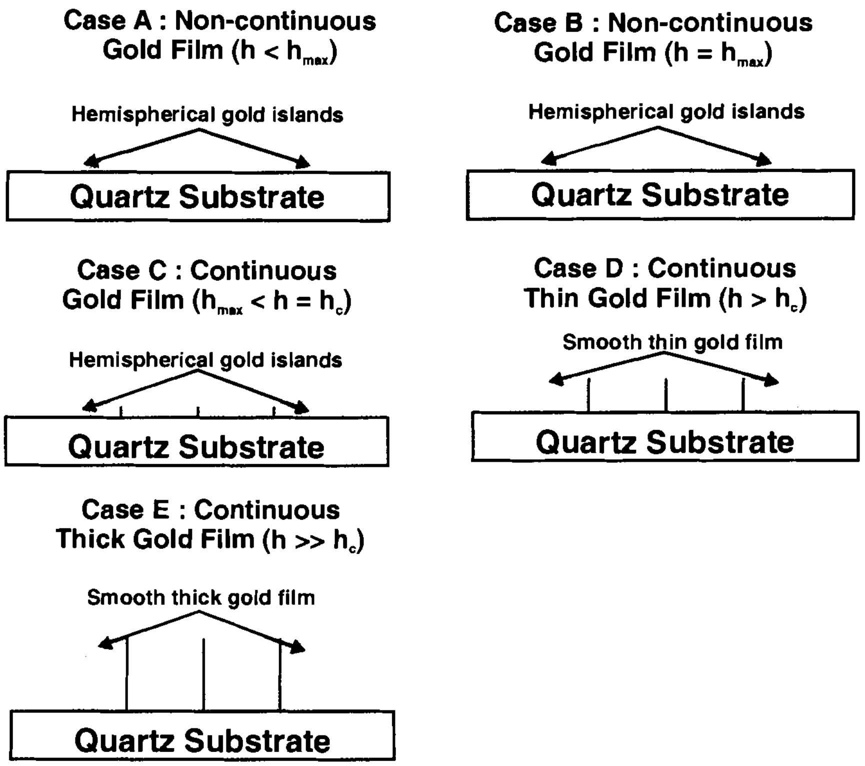

Figure 2.5 Gold film structure as a function of film thickness. The first film (A) is thin and non-continuous, the second film (B) is thin and non-continuous with maximized surface area, the third film (C) is just continuous with a slightly reduced surface area, the fourth film (D) is more continuous with even less surface area, and the last film (E) is thick with approximately the same surface area as the thinner continuous film (D).

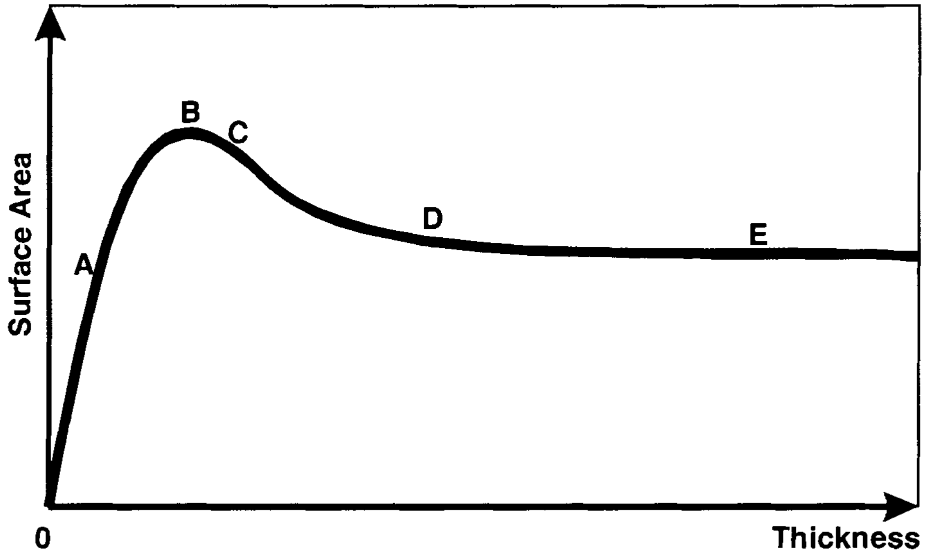

Figure 2.6 Gold film surface area as a function of gold film thickness.

hemispherical islands, case (A), the surface area increases as the film thickness increases. When the gold film thickness reaches $h_{\max}$, case (B), the hemispherical gold islands are just touching each other and the available gold film surface area is maximized. This results in the peak in the curve shown in Figure 2.6. Increasing the film thickness slightly greater than $h_{\max}$ case (C), results in the gold islands coming together to create a continuous film at a thickness of h_c. For case (C), there is a reduction in the available surface area. A further increase in film thickness, case (D), results in a decrease in the available surface area. At this point the surface of the gold film is relatively smooth and flat. Finally, when the film is much greater than h_c, case (E), the available surface area is almost the same as the available surface area for case (D).

For all of these cases, the surface mercury thickness at saturation is assumed to be constant, so that the total mass of mercury as a function of gold film thickness is proportional to the available gold film surface area. In this film region, the mass of the adsorbed mercury dominates the frequency change in the sensor. This is shown pictorially in Figure 2.7.

For extremely thin films which form islands, the surface area, and therefore mass of surface mercury, increases as the film thickness increases. Thus, over this range, $0 < h < h_{\max}$, increasing thickness will result in increased adsorption.

A slight increase in film thickness greater than $h_{\max}$ results in the gold islands coming together to create a continuous film at a thickness of h_c.

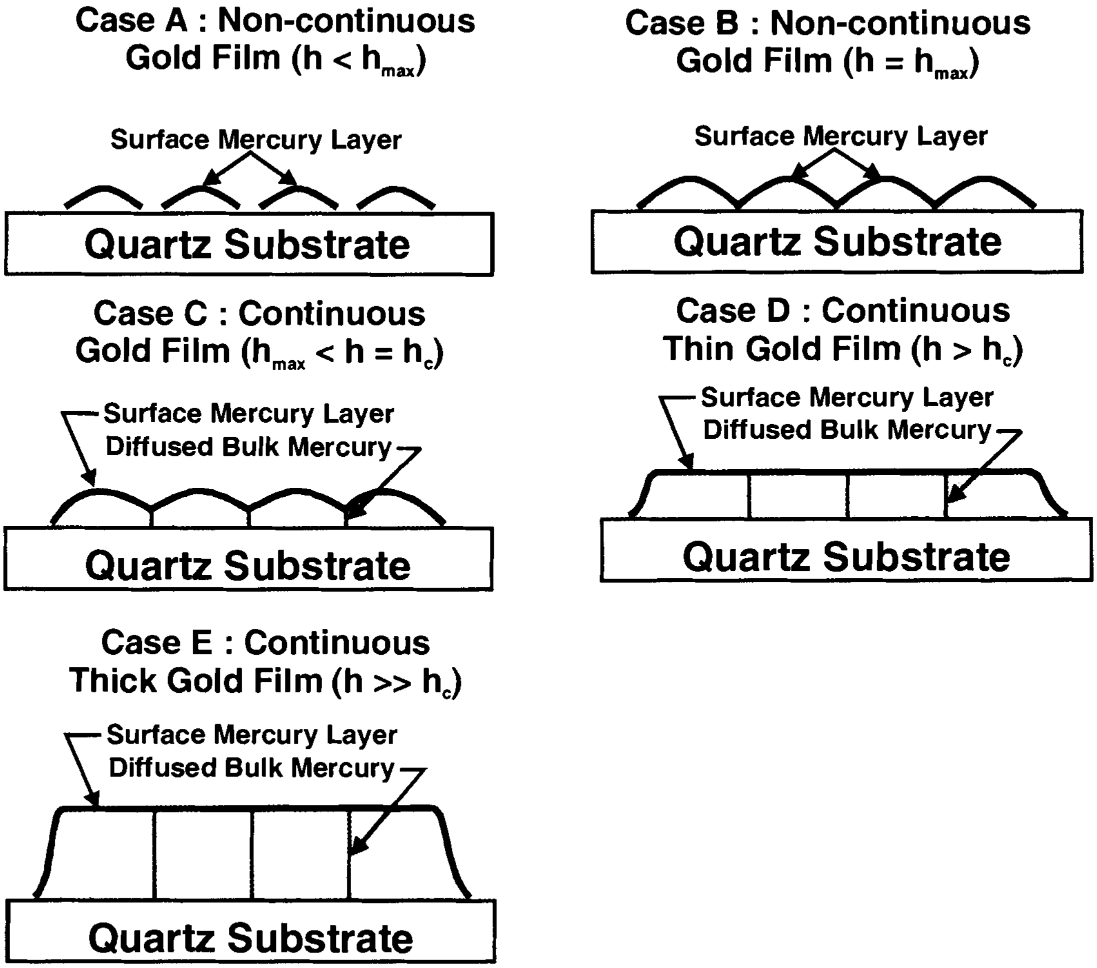

Figure 2.7 Mercury covered gold films as a function of film thickness. All films have approximately the same coverage of surface mercury. The first film (A) is thin and non-continuous, the second film (B) is thin and non-continuous with maximized surface area, the third film (C) is just continuous with a slightly reduced surface area, the fourth film (D) is more continuous with even less surface area, and the last film (E) is thick with approximately the same surface area as the thinner continuous film (D).

However, there is a slight reduction in the film surface area and a corresponding reduction in the mass of surface mercury. Over this range, $h_{\max} < h < h_c$, increasing thickness will result in decreased adsorption.

As the film thickness continues to increase to just above h_c, the surface area continues to decrease as the gold islands collapse into each other. Over this range, $h > h_c$, increasing film thickness results in decreased adsorption.

For thicker films, on the other hand, the surface mercury layer remains essentially constant. Thus, for $h >> h_c$ sensitivity to the surface mercury layer is virtually unaffected by increasing thickness.

The second region important in the model under development is the bulk of the film. It has been shown previously that mercury can penetrate a gold film to a depth, h_p, of several thousand angstroms [45]. In this regime, $0 < h < h_p$, the relatively small concentration of absorbed mercury increases mass only slightly, but dramatically increases the film stiffness. Because mechanically-induced frequency changes are proportional to the film thickness, h, (Equation 2.4), this effect will be more pronounced as thickness increases.

Considering both film regions in parallel, the surface mercury layer and the amalgam bulk, one would expect to see increasing sensitivity to mercury for increasing thicknesses up to $h_{\max}$, due to mass loading effects of the increased surface area outweighing the elasticity effects of increased bulk volume. For films in the range of $h_{\max} < h < h_c$, one would expect to see a decreasing sensitivity trend due to the reduced gold film surface area and corresponding reduced surface adsorption of mercury. In this range, elasticity effects would be just beginning due to the onset of a continuous film. For films thicker than h_c, up to a thickness of h_p, however, one would expect a decreasing sensitivity trend, due to the only slight increase in film mass being offset by the increase in stiffness. Figure 2.8 plots these trends for the mass loading and stiffening effects alone, as well as the net response from both effects simultaneously.

It is important to note that the model presented considers only the steady-state response magnitude. It is likely that the surface mercury layer approaches steady-state much more quickly than the bulk of the film, which relies on slower diffusion processes to reach steady-state. Thus, a dynamic model may be significantly more complicated than its steady-state counterpart, and pre-steady-state response slopes may not follow the same trend as steady-state response magnitudes.

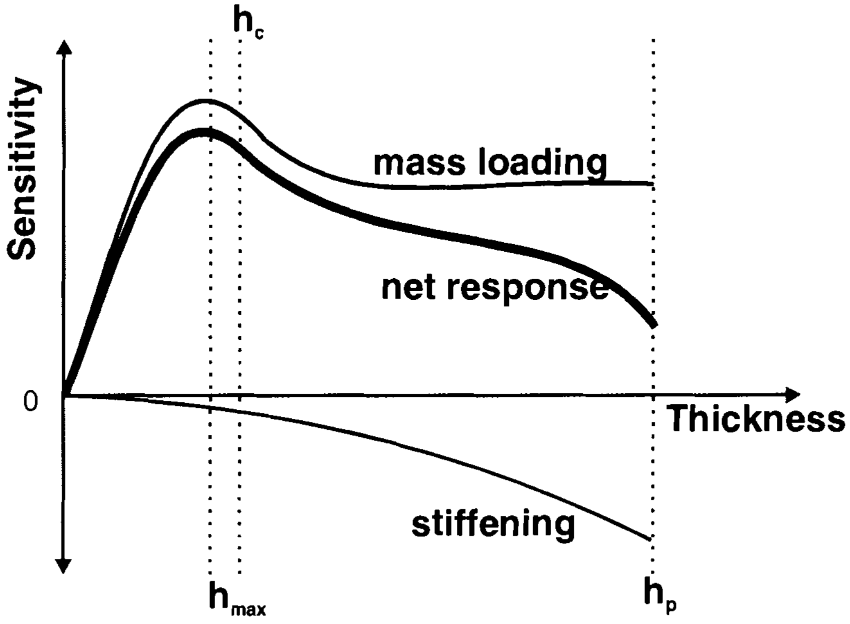

Figure 2.8 Expected sensitivity of SAW mercury sensor for mass loading, elastic stiffening, and both effects simultaneously as a function of film thickness.

Chapter 3. EXPERIMENTAL SETUP

3.1 Overview

The development and testing of a SAW mercury sensor requires numerous key subsystems. There are many physical and electrical components, which as a whole, make up the mercury sensor and the instrumentation used to characterize the sensing element's ability to detect mercury. Figure 3.1 is a functional block diagram showing all the various components and how they interact with each other.

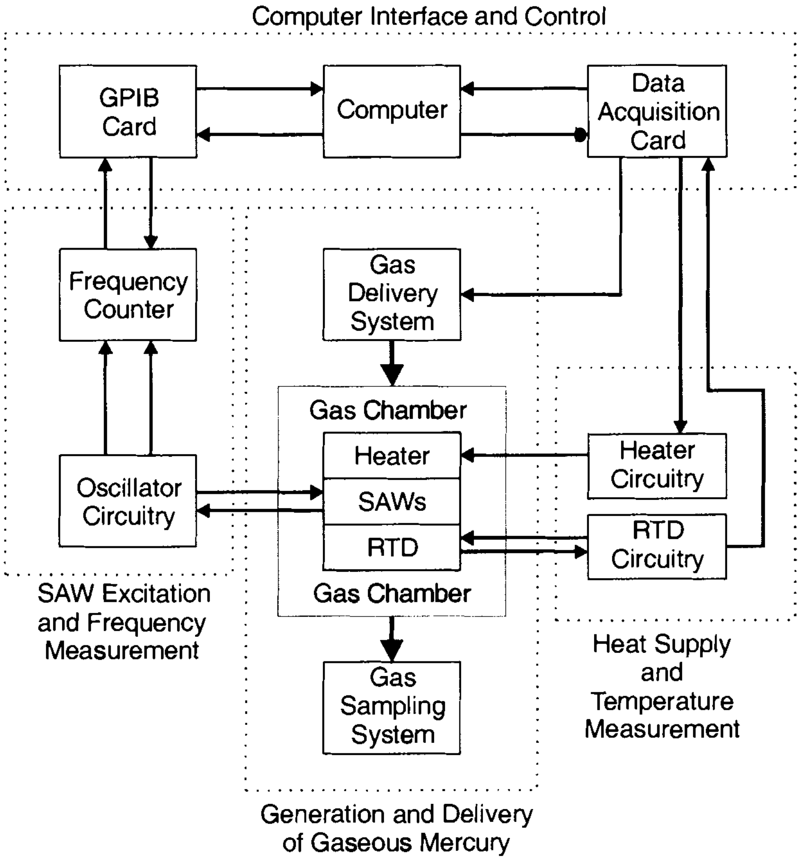

Figure 3.1 Block diagram of the experimental setup.

The following sections expand on Figure 3.1, breaking up the experimental setup into 6 sections (not including the overview section). Section 3.2 concentrates on the generation and delivery of gaseous mercury. Section 3.3 follows with a discussion of the packaging of the mercury sensor, including the sensing element, the heater, the resistive thermal device (RTD), the oscillator electronics and the gas chamber. Section 3.4 details the design of the oscillator circuit. The design of the microheater and the heater driver circuitry are covered in section 3.5. Section 3.6 follows with details on the RTD and the associated temperature measurement circuitry. Finally, section 3.7 summarizes all the previous sections by describing how the whole experimental setup is controlled and monitored with the data acquisition and control system.

3.2 The Mercury Delivery and Sampling System

To characterize the SAW mercury sensor, a gaseous mercury delivery system was designed and constructed. This was achieved using a Dynalcal® mercury permeation source, two VICI Metronics U-shaped glass tube heat exchangers, an OMEGA® temperature controlled oven, two Cole Parmer y-valves and two Cole Parmer 1000 sccm mass flow controllers as shown in Figure *3.2*.

The generation of gaseous mercury was accomplished by using a calibrated mercury permeation source. The source was made from a short section of silicon rubber permeable tubing that was filled with liquid mercury and plugged at both ends. The source was kept at a constant temperature of 50°C in a temperature-controlled oven. At this temperature, the mercury permeated through the walls of the silicon rubber tubing at a rate of 48ng/min.

To create a concentration of gaseous mercury, a controlled flow of dry nitrogen was fed into the U-shaped glass tube heat exchanger. The nitrogen was heated to 50°C by the glass beads and then passed over the permeation source, thus creating a concentration of gaseous mercury out the other end of the U-tube. Concentrations of mercury ranging from 20 ppb to 100 ppb were created by varying the flow rate of nitrogen across the permeation source from 292 sccm to 59 sccm, respectively. The second U-tube without a permeation source was used to create an identical control gas free of mercury.

The flow direction of the two gas streams was controlled by two y-valves connected by a tee. When the y-valves were turned "off" the mercury free

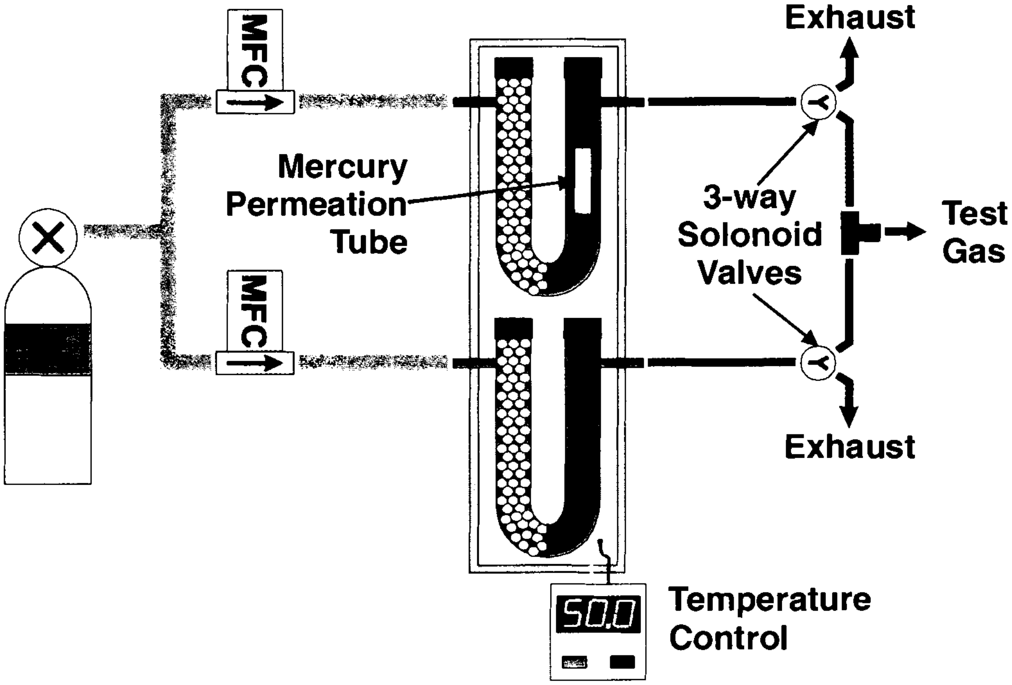

Figure 3.2 Schematic of the mercury delivery system.

nitrogen was fed to the output of the delivery system while the gaseous mercury was exhausted. When the y-valves were turned "on", the gaseous mercury was fed to the output of the delivery system while the mercury-free nitrogen was exhausted.

Fully automated control of the mercury delivery system was accomplished by interfacing the mass flow controllers and the y-valves to a data acquisition card installed in a computer. The mass flow controller set points were supplied by an analog voltage between 0 and 5 volts corresponding to flows of 0 to 1000 sccm. The states of the y-valves were set by a digital voltage fed into a solenoid driving circuit connected to the two y-valves.

Since varying flow rates are necessary to generate different concentrations of mercury, an independent means of exposing the sensor to the test gas was needed. A manually adjusted slip stream sampling method was developed to control the flow of sample gas precisely across the sensing element.

If you were to connect the output of the coupled y-valves directly to the inlet of the mercury sensor, you would observe a varying baseline which is dependent on the flow rate of gas through the delivery system. Figure 3.3 shows some experimental measurements on the dependence of a mercury sensor's baseline on the flow rate of mercury-free nitrogen flowing out of the mercury delivery system.

As can be seen in Figure 3.3, every time the mercury delivery system changed flow to create a new concentration, the mercury sensor experienced a

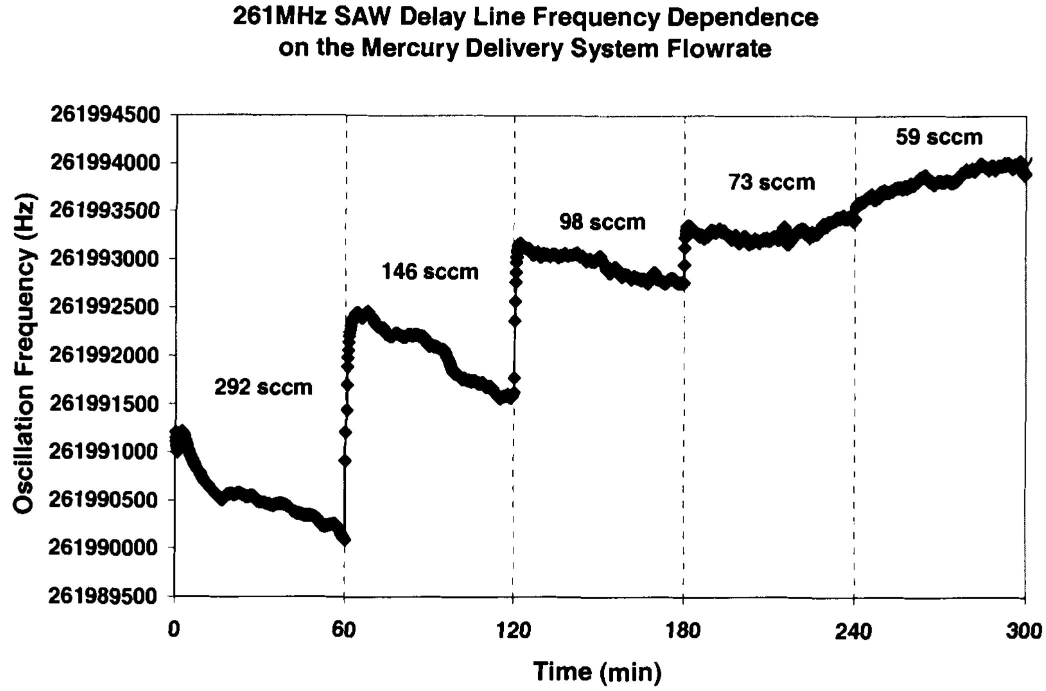

Figure 3.3 Sensor's dependence on the delivery system's flow rate.

change in the baseline oscillation frequency. Some of this dependence could be reduced by using a properly designed dual delay line to measure difference frequency, but it is always a good idea to try to reduce the sensor's dependence on any environmental factor other than the measurand of interest.

To reduce the sensor's dependence on the delivery system's flow rate, a slip stream sampling method was utilized, as shown in Figure 3.4. The output of the delivery system was connected to an additional tee, where one side of the tee was exhausted and the other side of the tee was connected to the input of the mercury sensor. The output of the mercury sensor was then connected to the input of a Cole Parmer 100 sccm mass flow controller. Finally, the output of the mass flow controller was connected to a dc brushless pump. The mass flow

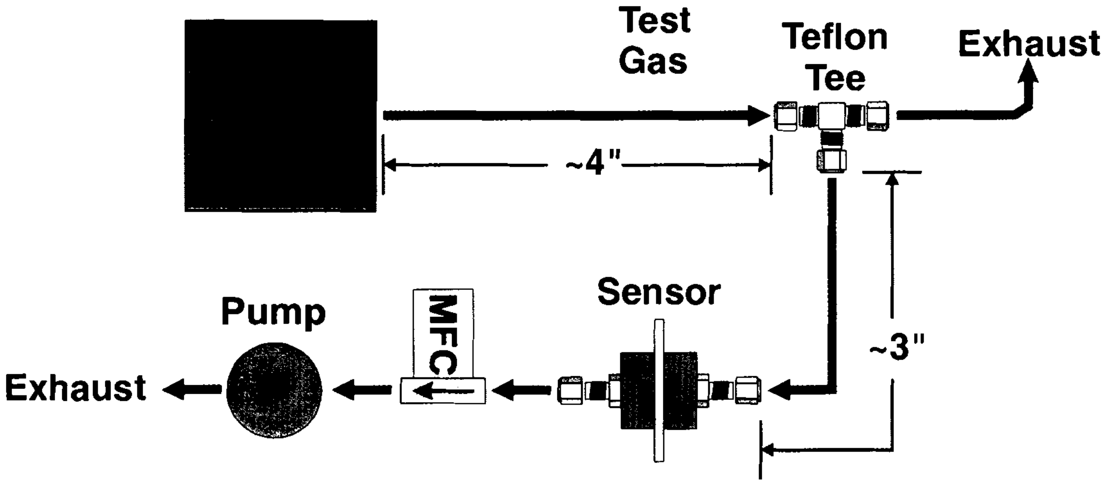

Figure 3.4 Slip stream sampling method. All tubing was Teflon® 1/8" outer diameter with a 1/16" inner diameter.

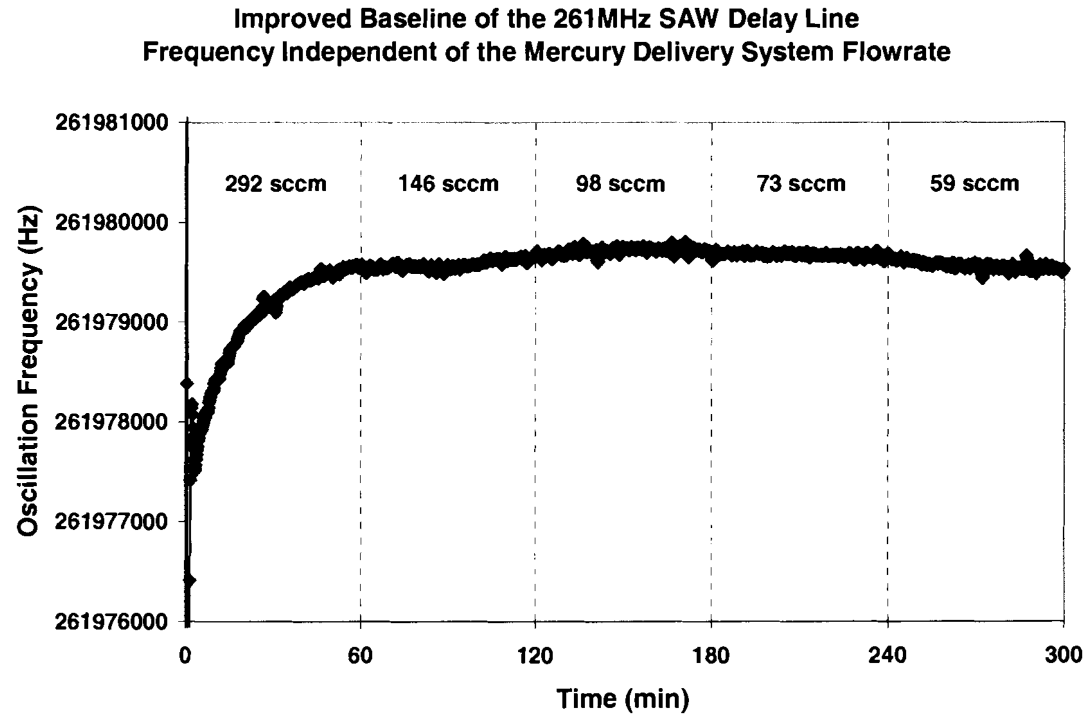

Figure 3.5 Sensor's improved baseline independent of the delivery system's flow rate.

controller measured differential pressure between its input and output and controlled the sample mass flow across the sensor to 50 sccm. Any additional flow at the tee connector was exhausted.

After incorporating the slip stream sampling system, the sensor's baseline became much more stable and independent of the flow rate used to generate varying concentrations of mercury. Figure 3.5 demonstrates the improved baseline.

Finally, the mercury delivery system was calibrated by placing a gold trap in place of the sensor to collect numerous samples of various concentrations of mercury. The mercury samples were measured using a Brooks Rand Cold Vapor Atomic Fluorescence Spectrometer (CVAFS) and the delivery system was shown to be within 10% of the expected mercury concentration.

3.3 The SAW Sensor Packaging

The following section describes the packaging of the SAW mercury sensor with all the components necessary for exciting the SAW, maintaining the operating temperature, and delivering the test gas to the sensing element.

The SAW sensing element with the heater, resistive thermal device (RTD), and oscillator circuitry are shown in Figure 3.6. A square through hole was cut out of a brass rf circuit board to provide a thermally isolated area to mount the heater, RTD and sensing element. A 15Ω microheater fabricated on a thin piece of alumina substrate was used as both a heating element and a support structure. Using a parallel gap welder, the microheater was attached to the

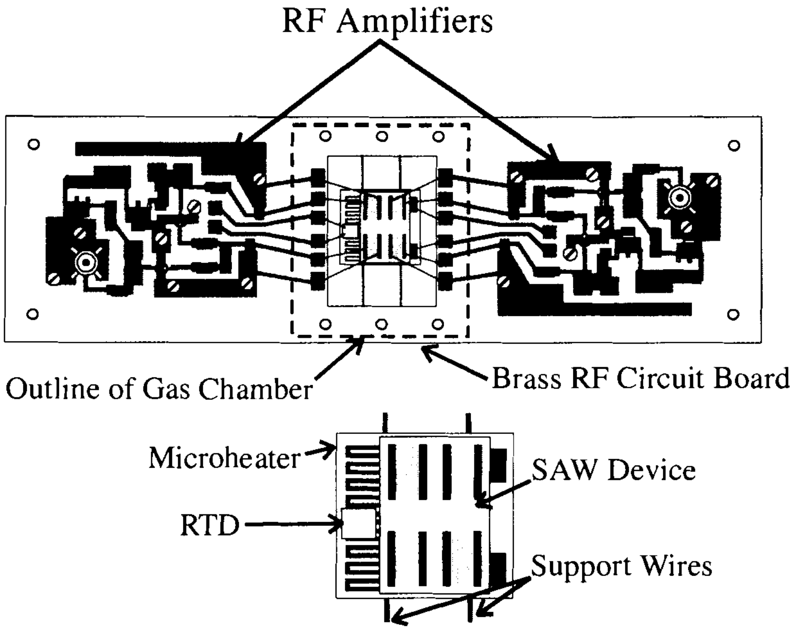

Figure 3.6 Layout of the heater, RTD, sensing element and the rf oscillator.

brass-backed rf circuit board using platinum wires. The sensing element and a 100Ω RTD were then mounted to the surface of the heater using a high temperature ceramic-based adhesive. The heater and RTD wires were parallel gap welded to the circuit board, while the rf SAW connections were made with an ultrasonic wedge bonder using 25μm aluminum bonding wire.

A two-piece, Teflon® gas chamber was mounted to the top and bottom of the circuit board around the sensing element (Figure 3.7). The gas chamber was designed to direct the inlet gas onto the top surface of the sensing element, around the sides of the sensing element, heater, and RTD and finally out the center of the bottom half of the gas chamber. Once the sensor was assembled and protected within the Teflon® gas chamber, the oscillator circuits were assembled and wires for the power supply, heater driver circuit and temperature measurement circuit were attached.

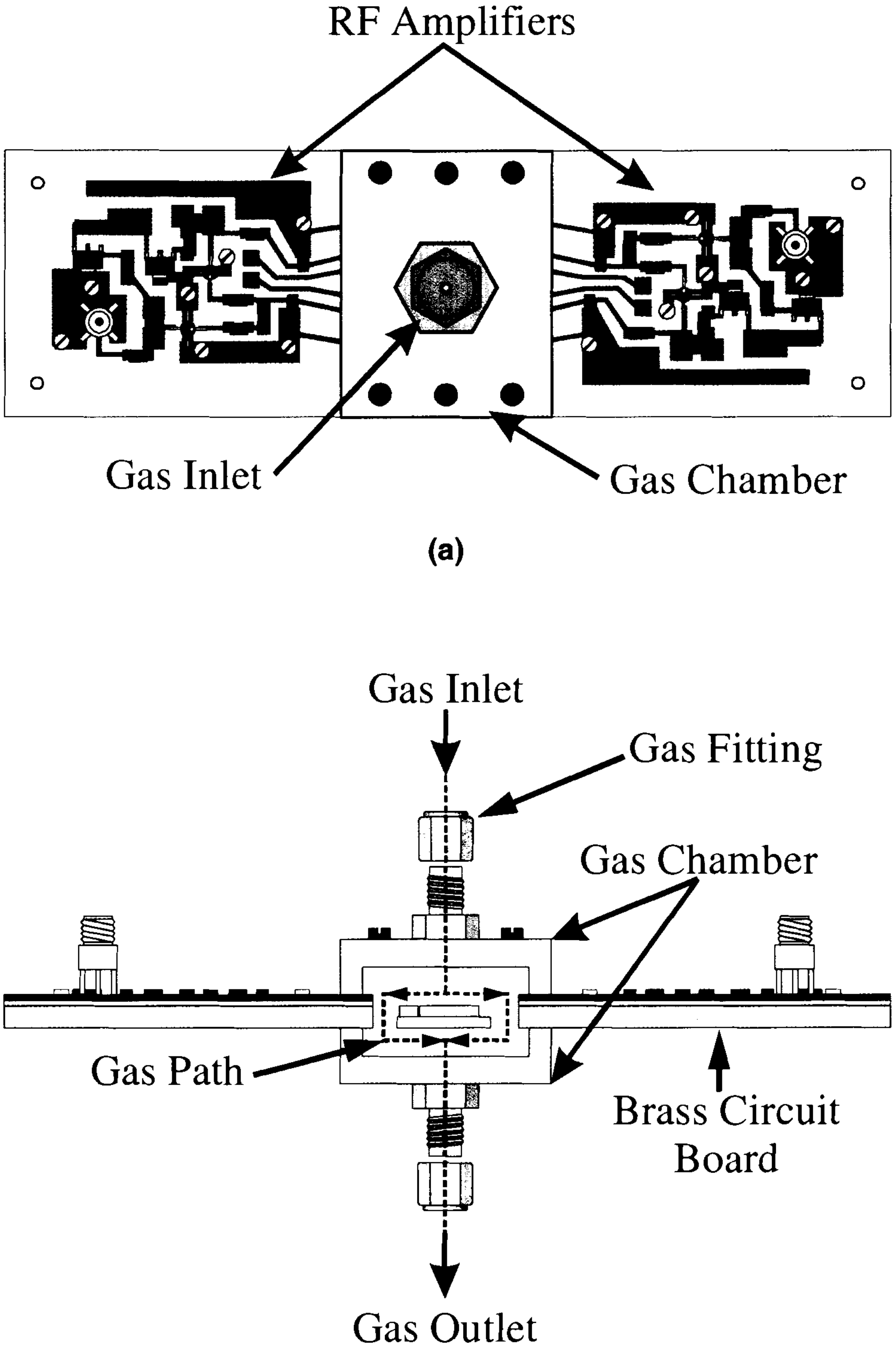

(a)

(b)

Figure 3.7 Illustration of the mercury sensor platform with the gas chamber. (a) Top view of the mercury sensor. (b) Side view of the mercury sensor gas chamber and gas flow path.

3.4 The Oscillator Circuitry

The oscillator circuit used on each of the delay lines is shown in Figure 3.8. The circuit was centered around two Mini-Circuits® MAR-6 amplifiers. The first, U1, was used as positive feedback for the delay line, while the other, U2, was used to provide a buffered signal to the frequency counter.

U1 was biased with a 5V regulator through the 100Ω potentiometer, R2, and the 100nH inductor, L1. Inductor L1 was an RF choke, while the 10nF capacitors, C1 and C2, were used as DC blocking capacitors preventing the rest of the oscillator loop from seeing the DC bias. The 2.2pF capacitors, C5 and C6, were used to shunt higher order modes and high frequency electromagnetic feed through.

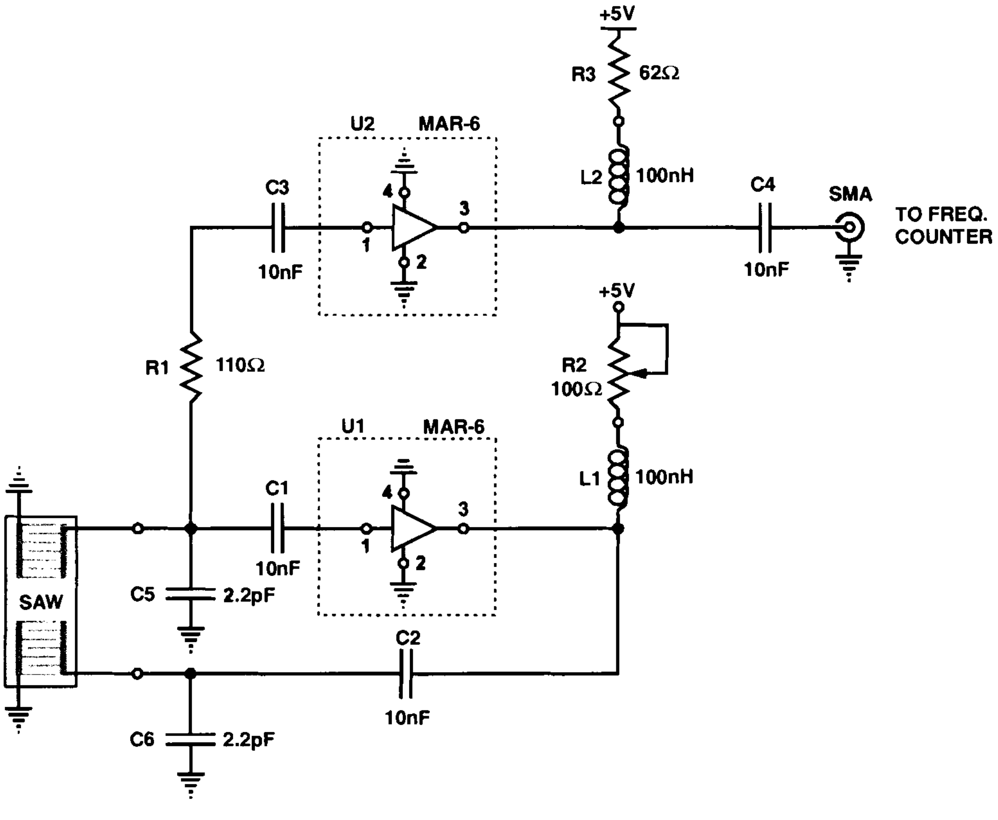

Figure 3.8 Schematic of the SAW oscillator.

The gain of amplifier U1 was set by the DC input current at pin 3, which was determined by the resistor R2. Stated earlier in section 2.2, insertion losses ranging from 13 to 16dB across the delay line required different values of gain to satisfy the oscillation requirements. Additional losses due to mercury/gold interactions and the fact that the amplifier was a source of phase shift causing the delay line not to oscillate at its peak frequency increased the gain requirements as well. To simplify the choice of R2, a 100Ω potentiometer was used to allow adjustment of the gain from 11 to 20dB.

The second amplifier, U2, was used to provide a buffered sample of the oscillator signal to the frequency counter. Amplifier U2 was coupled to the oscillator loop through the 110Ω resistor, R1. Similar to U1, U2 was biased with a 5V regulator through the 62Ω resistor, R2, and the 100nH inductor, L2. The gain of U2 needed only to be strong enough for the frequency counter to detect and had no bearing on the function of the oscillator. The inductor L2 and the capacitors C3 and C4 served the same purposes as inductor L1 and capacitors, C1 and C2, respectively. Finally, the output of the buffer amplifier was coupled to the frequency counter through capacitor C4 and the SMA connector.

3.5 The Microheater and the Heater Driver Circuitry

The microheater used for heating the SAW device was a custom made chrome serpentine pattern fabricated on top of a polished alumina substrate. (Figure 3.9) The design of the heating element was based upon two factors, the size of the SAW device and the heater driver circuitry.

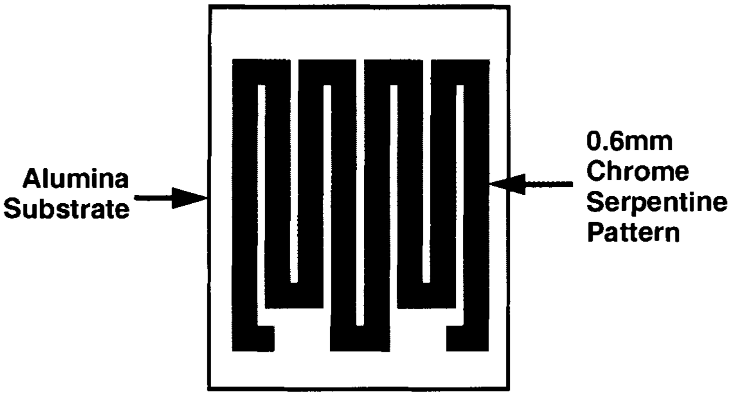

Figure 3.9 Chrome serpentine microheater.

A low resistance heater value was desired to reduce the power supply requirements of the heater control circuitry. Higher resistance heaters require higher driving voltage and lower current to achieve a certain amount of power, or heating, while lower resistance heaters require lower driving voltage and higher current to achieve that same amount of power. Low voltage, high current power supplies are typically cheaper and more common than high voltage power supplies, so the resistance of the heater was chosen to be 15Ω.

The footprint of the SAW device and the RTD required the heater to be 0.275 x 0.35" and the serpentine pattern was designed to have 51.6 mm pattern length and a 0.6 mm line width. The 15 Ω resistance value was achieved with a 10,000 Å chrome metal thickness. The resulting voltage requirements as a function of temperature that a heater driver circuit would need to supply are shown in Figure 3.10. At 300°C just below 14 volts were required by the microheater.

The circuit used to power the microheater is shown in Figure 3.11. An

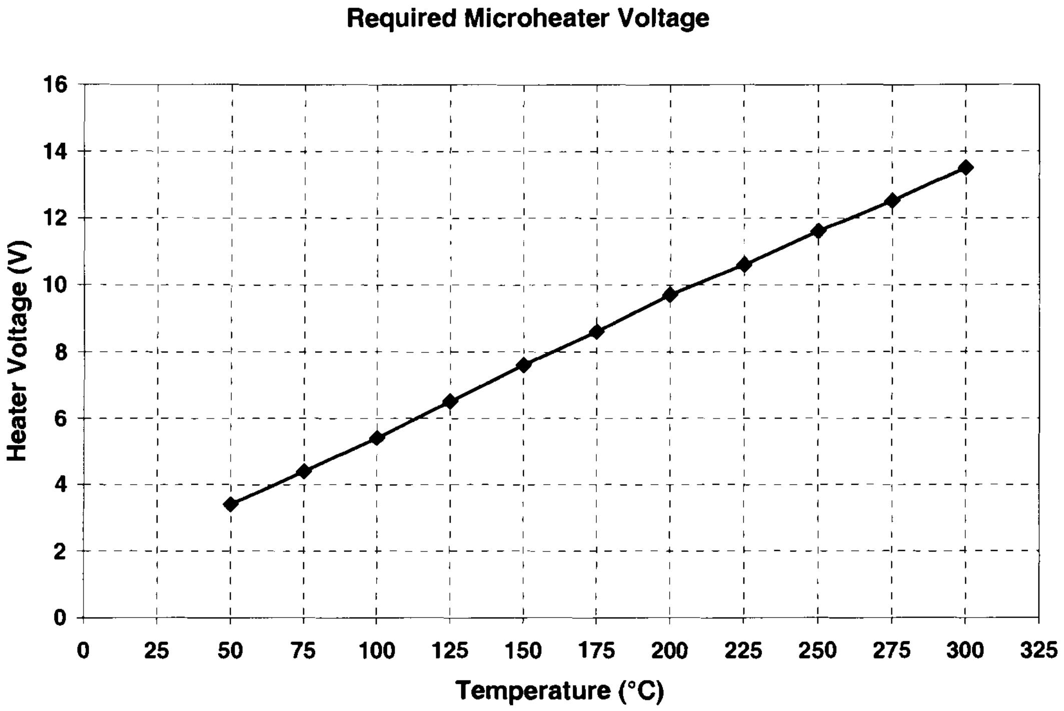

Figure 3.10 Required driving voltage for the microheater.

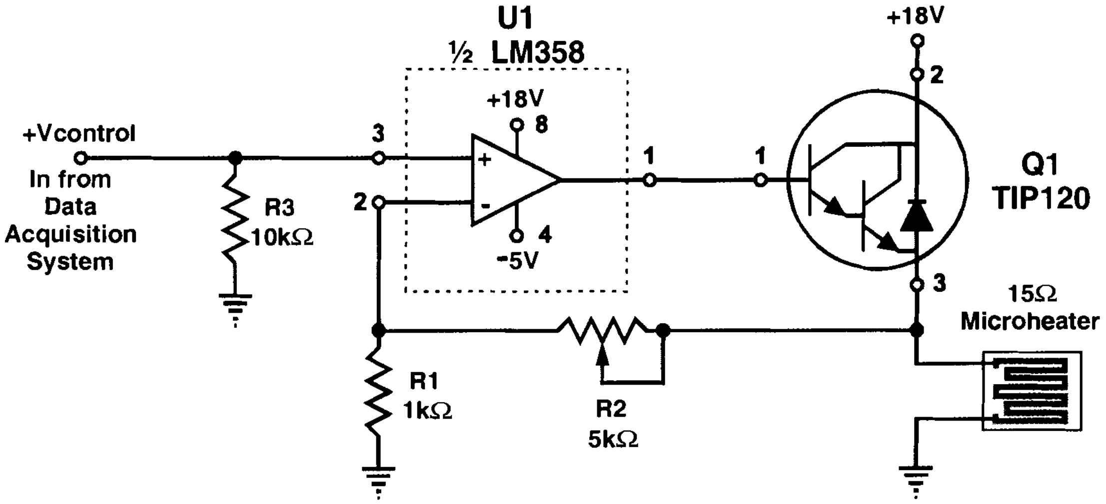

Figure 3.11 Schematic of the heater driver circuit.

opamp, U1, and a Darlington transistor, Q1, were setup in a high current, non-inverting amplifier configuration. The gain of the amplifier was determined by the resistors, R1 and R2, where the emitter voltage tied to the microheater was equal to (1+ R2/R1)Vcontrol.

The input voltage, Vcontrol, was a 0 to 5V analog voltage sent by a data acquisition card in the computer. The potentiometer, R2, was adjusted to create a gain of 3, thus setting the maximum possible heater voltage to 15 volts. This gave the heater a temperature range of 0 to slightly greater than 300°C.

The resistor, R3, was used to tie the input of the opamp to a fixed reference point. It's worth noting that without R3, the input of the opamp would be floating when the computer was shut off. This typically resulted in the heater circuit instantaneously driving the heater with its maximum voltage. Thermal gradients and stresses due to fast heating of the quartz substrate usually result in the substrate cracking, ruining the sensing element. When the computer was shut off, R3 caused Vcontrol to go to zero, disabling the heater and protecting the sensing element.

3.6 The RTD and the Temperature Measurement Circuitry

The temperature measurement was achieved with an OMEGA® 100Ω platinum RTD wired into a 100Ω bridge circuit signal conditioned with an instrumentation amplifier. The temperature versus RTD resistance profile is shown in Figure 3.12. The range of the RTD circuitry was chosen to be 0 to 5 volts corresponding to a temperature range of 0 to 500°C, respectively.

The temperature measurement circuitry is shown in Figure 3.13. The RTD was placed into a 100Ω bridge circuit biased with 0.5 volts supplied by U1 set up in a voltage follower configuration. The 10kΩ potentiometer, R1, was used to set the bridge bias voltage to 0.5 volts. The RTD had a resistance of 100Ω at 0°C, so the signal voltage produced by the 100Ω bridge circuit was 0 volts at 0°C. At 500°C the RTD would have a resistance of 287.6Ω, as determined by Figure 3.12, and the bridge circuit would theoretically produce a signal voltage of ½[287.6/(287.6 + 100)] - ½[100/(100 + 100)] = 121mV. The signal voltage was fed into the instrumentation amplifier, U2, and the gain was set to approximately 41.3 by the 5kΩ potentiometer, R5. The amplifier's output voltage across the 10kΩ resistor, R6, was fed into a data acquisition card installed in the computer. Since the RTD's resistance versus temperature relationship was known (Figure 3.12), the temperature measurement circuit's output voltage could be determined as a function of the RTD temperature.

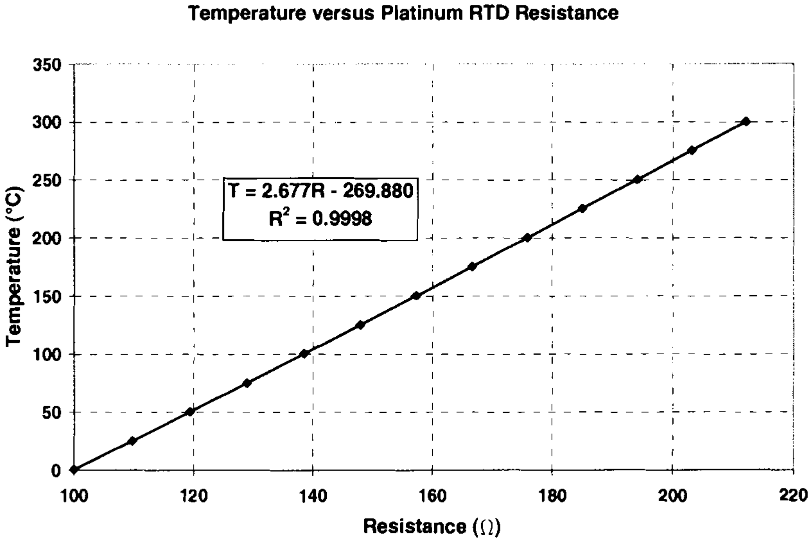

Figure 3.12 Plot of temperature versus RTD resistance.

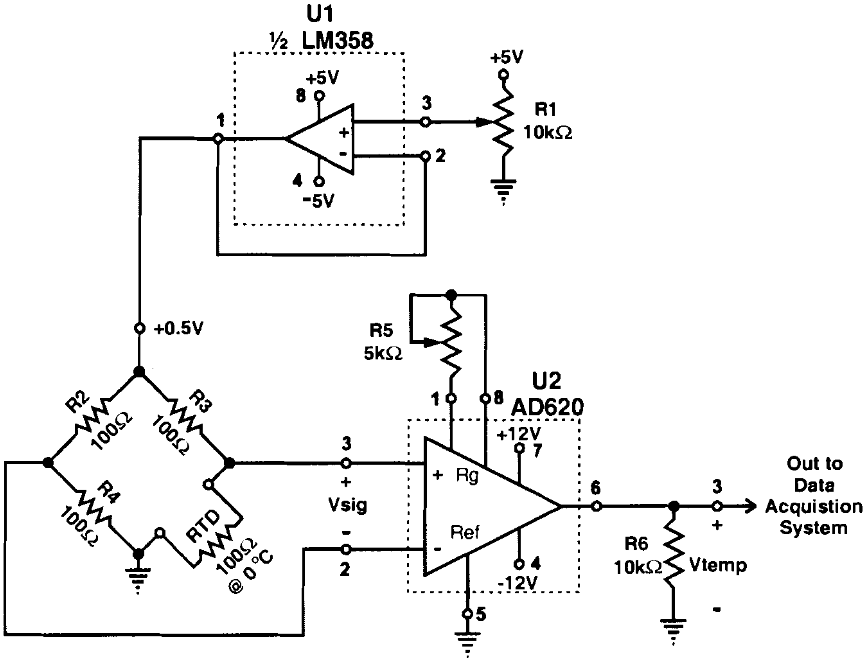

Figure 3.13 Schematic of the RTD temperature measurement circuit.

3.7 Data Acquisition and Control

The temperature control, mercury delivery system control, and data acquisition were accomplished by using a C++ program running on a 200 Mhz computer. The computer was equipped with a National Instruments data acquisition card for measuring and sending digital and analog signals. The computer was also equipped with a National Instruments GPIB card for interfacing to a HP3109 frequency counter. Figure 3.14 shows how the computer was interfaced to the support electronics, mercury delivery system, and measurement equipment.

The sensing element's operating temperature was maintained with the microheater, the heater driver circuitry, the RTD, and the temperature

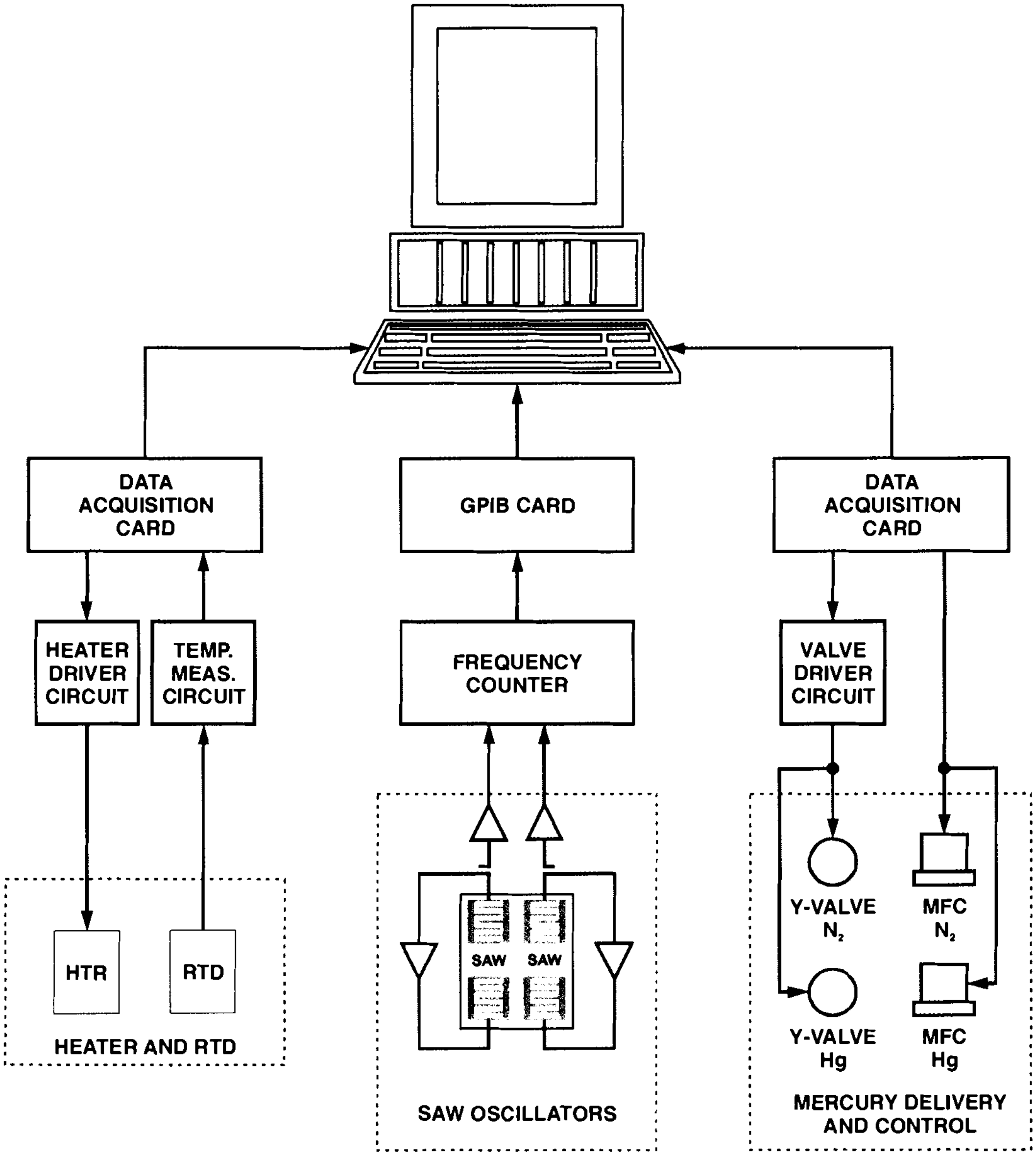

Figure 3.14 Schematic of the control of the experimental setup.

measurement circuitry. The 0 to 5 volt analog signal from the temperature measurement circuit was read by the data acquisition card installed in the computer. The computer used an equation which converted the measured voltage into a temperature. It then used a PID algorithm to determine a new voltage set point (between 0 and 5V) which was sent out via the data acquisition card to the heater driver circuit.

The control of the mercury delivery system was accomplished with the data acquisition card using one digital and two analog outputs. Each mass flow controller required a 0 to 5 volt analog voltage from the card corresponding to a flow set point of 0 to 1000 sccm. The digital output was sent to a y-valve switching circuit which applied a momentary 12 volt signal to open the y-valves and then dropped the voltage down to 5 volts to keep them open. The circuit switched both y-valves at the same time, thus toggling the flows of the two gases between the exhaust and the output of the mercury delivery system.

Finally, the oscillation frequencies of the two SAW delay lines were measured using a Hewlett Packard HP3109 high frequency counter that interfaced to the computer with a GPIB card.

Chapter 4. EXPERIMENTAL RESULTS

This chapter discusses the experimental data acquired with the SAW mercury sensor. Beginning with section 4.1, the testing protocol used to evaluate the sensors is explained. The data processing and the evaluation procedures are also described. Next, section 4.2 examines the response magnitude and slope for the SAW mercury sensor as a function of the gold film thickness. Section 4.3 follows up with a close examination of the response slope as a function of the mercury concentration. Finally, section 4.4 summarizes the data with a discussion of the results.

4.1. The Testing Protocol

Eight SAW mercury sensors, each with a different gold film thickness, were exposed to various concentrations of mercury. The gold film thicknesses were 25, 50, 75, 100, 200, 300, 400 and 500Å of gold on top of 50Å tungsten adhesion layers. The tungsten and gold films were deposited in the same deposition run using DC and RF magnetron sputtering, respectively. The mercury gas concentrations were chosen to be 20, 40, 60, 80 and 100 ppb mercury in nitrogen. The operating temperature of the SAW delay line was chosen to be 50°C throughout the testing sequence, except to desorb mercury from the gold film in between gas exposures. Figure 4.1 shows the SAW temperature and mercury concentration profiles for the testing sequence used.

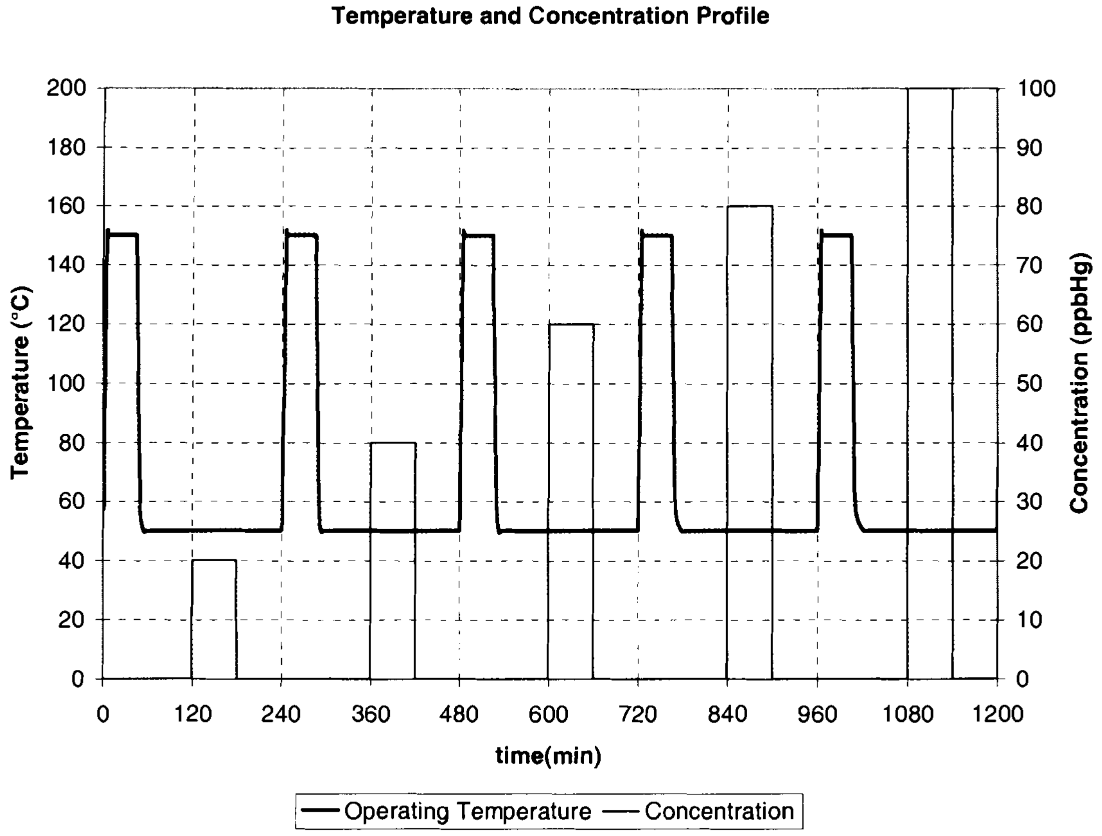

Figure 4.1 Temperature and concentration profile for all the gold film thicknesses tested.

First the sensor was heated to 150°C for 45 minutes to drive off any mercury that may have been amalgamated with the gold film. Next the sensor was given 1 hour and 15 minutes to cool down to 50°C and to establish a baseline. The sensor was then exposed to the gaseous mercury for 1 hour and finally the sensor was allowed to recover in mercury-free nitrogen for another hour. The four-hour testing sequence was repeated for each additional concentration tested. Thus for a total of 5 concentrations levels, the total time required was 20 hours.

To ensure the mercury concentrations were stabilized at the time of exposure, the delivery system mass flow rates were set at the beginning of each four-hour sequence. This gave the delivery system two hours to equilibrate prior to each exposure.

Figure 4.2 shows a 75Å gold coated SAW response as an example of a typical general SAW response profile. The general response profiles were then put through a 23 point Savitzky-Golay smoothing routine to clean up the data and then a first derivative algorithm was used to calculate the slope of the response [46-47]. Each general response profile and general response slope profile was then broken up into 4 hour intervals to allow the independent qualitative evaluation of each gas concentration profile.

Due to the large quantity of plots, only the 100ppb mercury response magnitude and response slope curves are shown in the next section. For

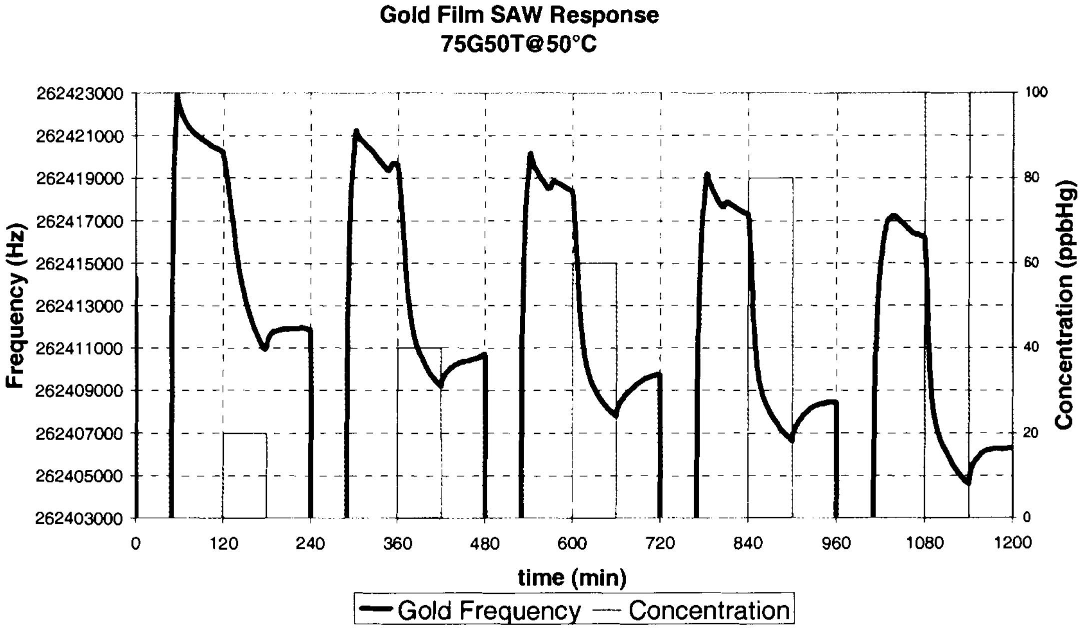

Figure 4.2 A typical general gas response profile for a 75 angstrom gold-coated mercury sensor.

completeness, the whole set of data is given in the Appendix. The qualitative shapes of the responses across the whole range of gold film thickness were similar for all the concentrations tested. The 100ppb mercury responses were chosen because the effects of mass loading and elasticity were amplified due to the larger concentration of mercury. The next section, however, does contain summary plots of response magnitude and slope as a function of gold film thickness for all the concentrations tested.

4.2. Response Magnitude and Slope vs. Thickness

Sensor response magnitude and slope curves for eight gold film thicknesses (i.e. 25, 50, 75, 100, 200, 300, 400 and 500Å) exposed to 100 ppb mercury at 50°C are shown in Figures 4.3 to 4.10. The 25Å gold film, shown in Figure 4.3, responded most quickly, with a maximum negative slope of 1.01 kHz/min, but was also the quickest to become saturated at only 5.8 kHz of frequency shift after one hour of exposure. For the 50Å gold film shown in Figure 4.4, the one hour response magnitude was considerably larger at approximately 10.4 kHz of frequency shift, while the maximum negative response slope became slightly smaller at approximately 0.95 kHz/min. For the 75Å gold film, shown in Figure 4.5, the largest one hour response magnitude occurred with roughly 11.5 kHz of frequency shift. The maximum negative slope for this thickness was approximately 0.99 kHz/min. For the 100Å gold film shown in Figure 4.6, both the one hour response magnitude and maximum negative slope became smaller at 10.7 kHz and 0.85 kHz/min, respectively. This decreasing sensitivity trend continued for further thickness increases from 200 to 500Å as shown in Figures 4.7 to 4.10.

Figure 4.11 summarizes the data from the previous 100 ppb Hg response curves. Looking carefully, it is obvious that for the 100 ppb Hg exposure, the largest response magnitude occurred with the 75Å gold film. The 75Å film also had the 2nd largest response slope followed closely by the 50 and 100Å gold films.

In fact, for all the concentrations tested (Figures 4.11 to 4.15), the 25Å gold film produced the largest maximum negative response slopes and the smallest one hour response magnitudes.

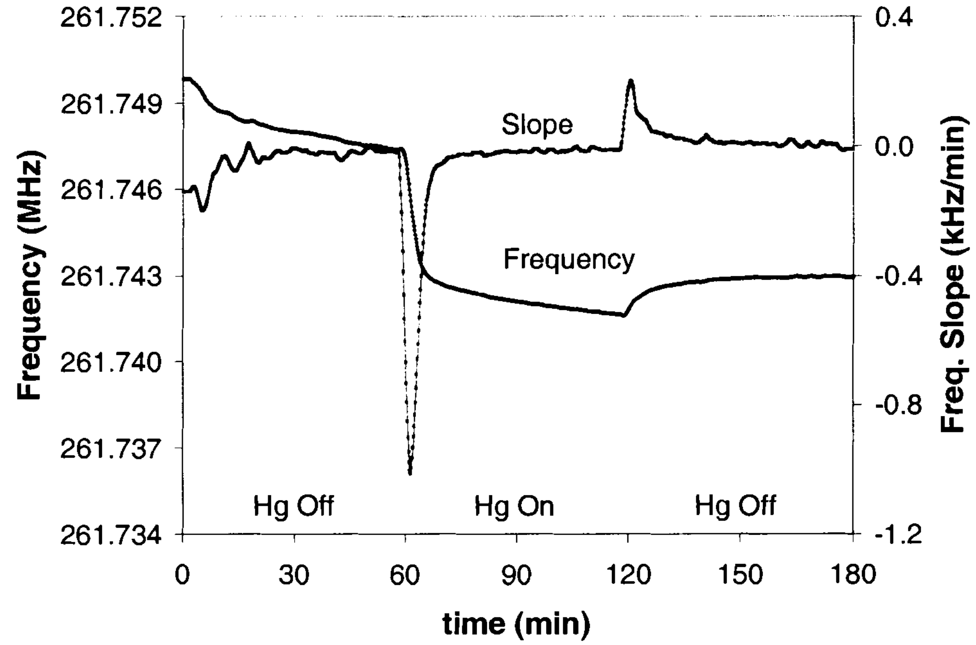

Figure 4.3 Response magnitude and slope for the 25Å gold film to 100 ppb Hg at 50°C.

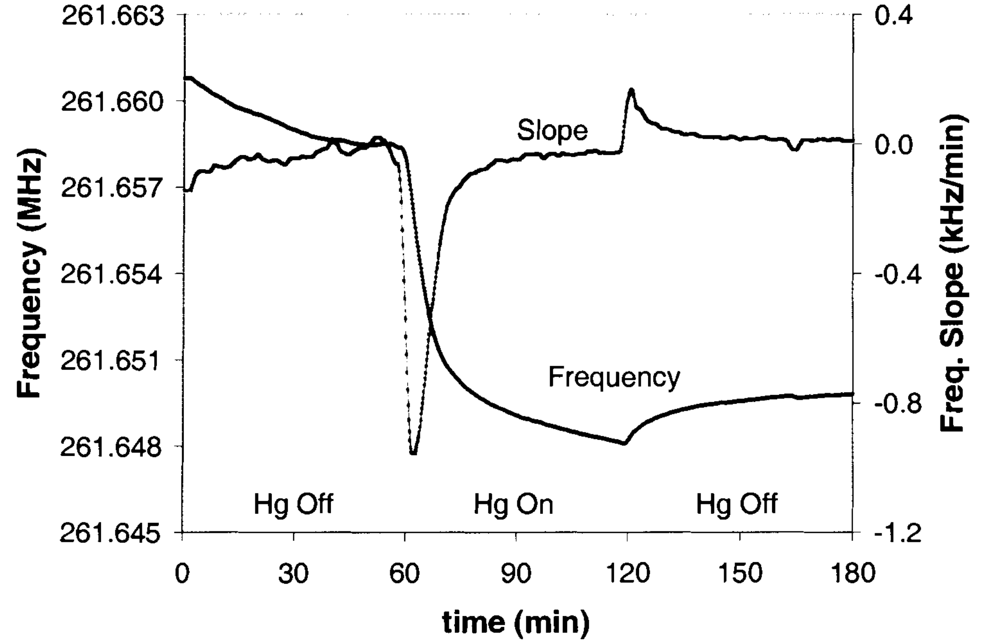

Figure 4.4 Response magnitude and slope for the 50Å gold film to 100 ppb Hg at 50°C.

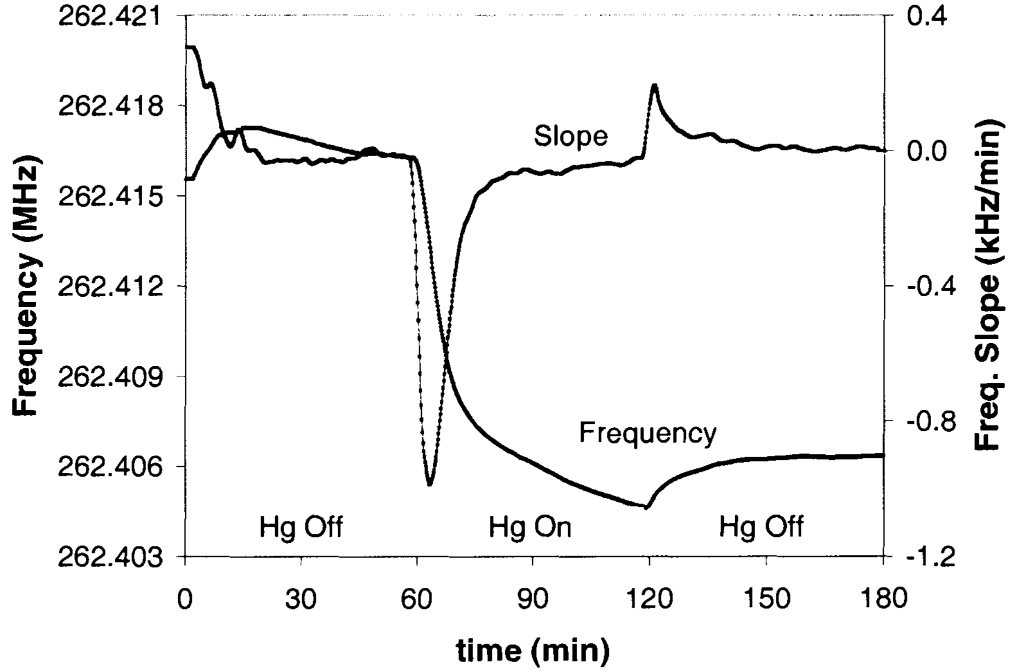

Figure 4.5 Response magnitude and slope for the 75Å gold film to 100 ppb Hg at 50°C.

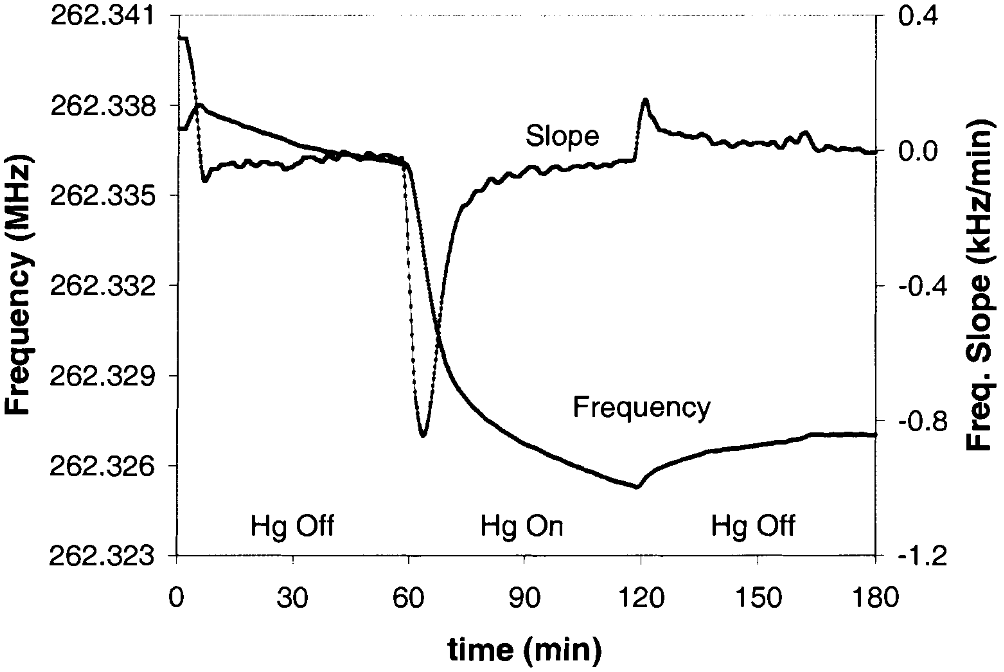

Figure 4.6 Response magnitude and slope for the 100Å gold film to 100 ppb Hg at 50°C.

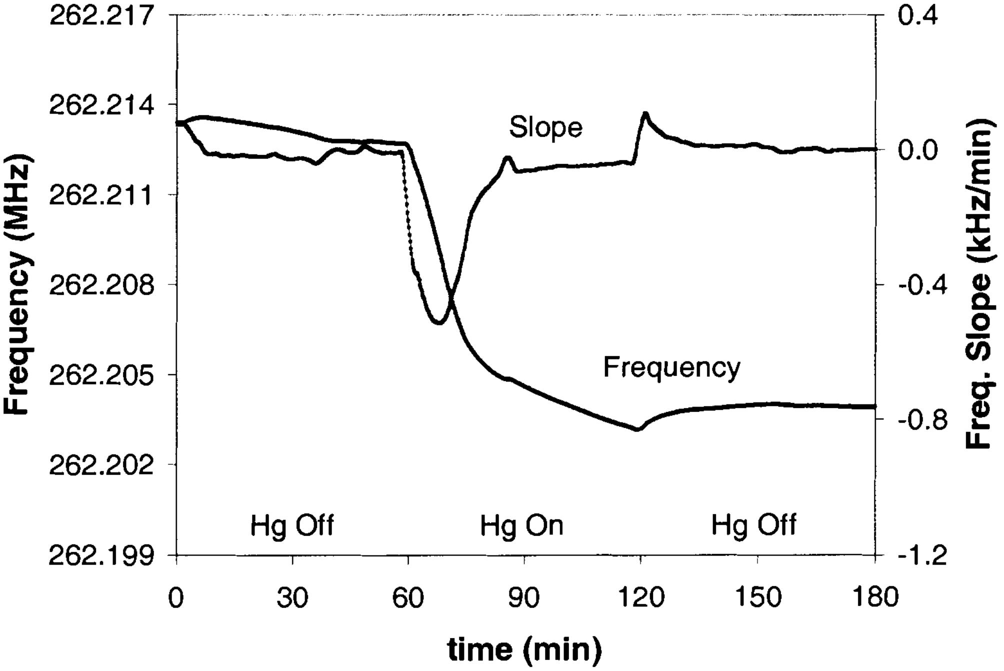

Figure 4.7 Response magnitude and slope for the 200Å gold film to 100 ppb Hg at 50°C.

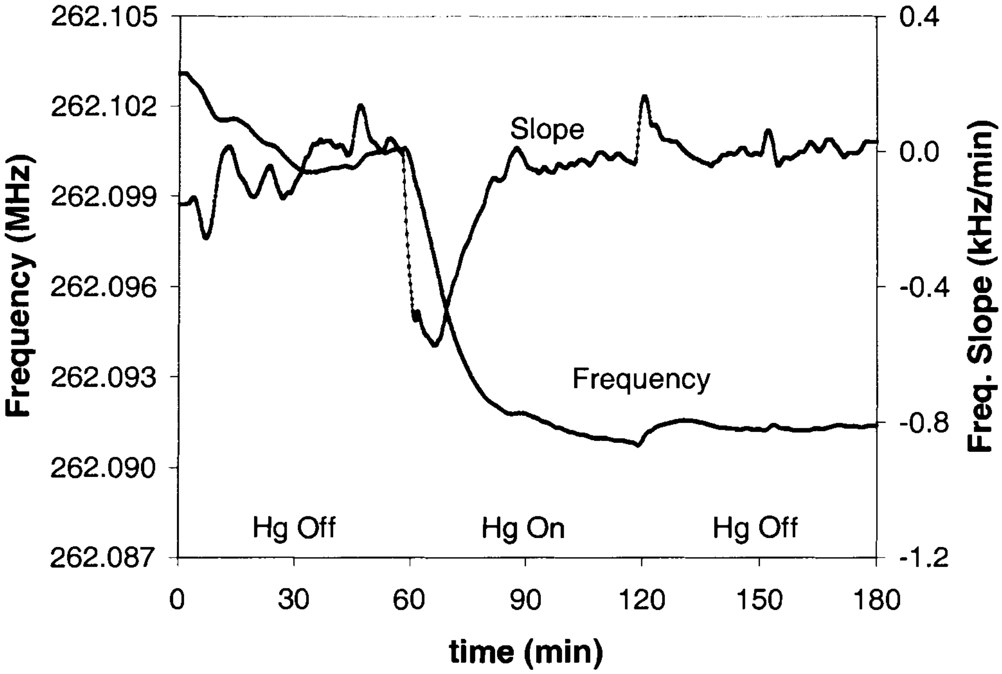

Figure 4.8 Response magnitude and slope for the 300Å gold film to 100 ppb Hg at 50°C.

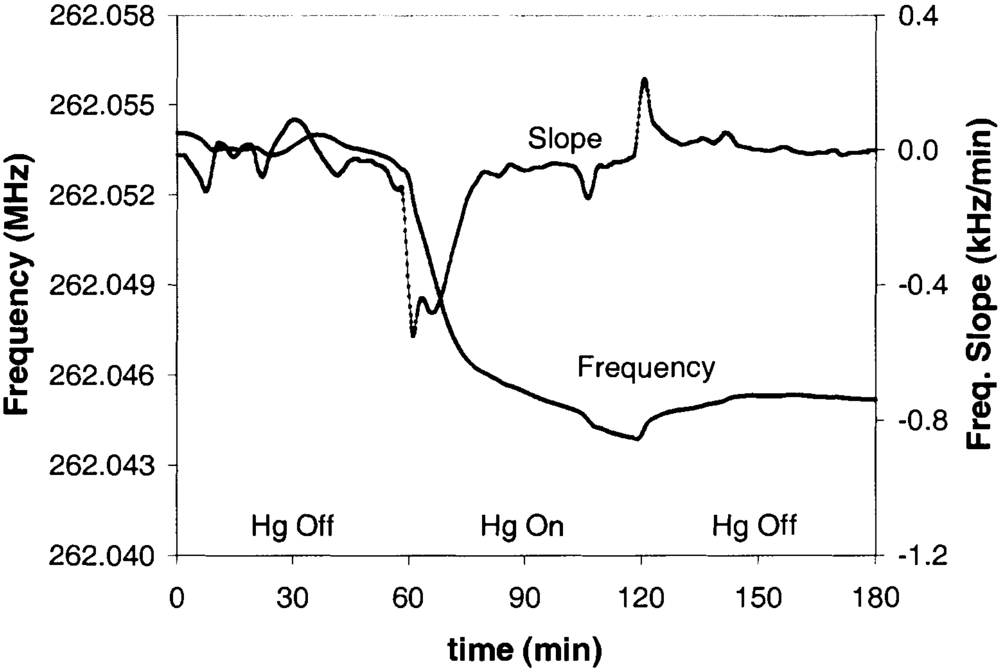

Figure 4.9 Response magnitude and slope for the 400Å gold film to 100 ppb Hg at 50°C.

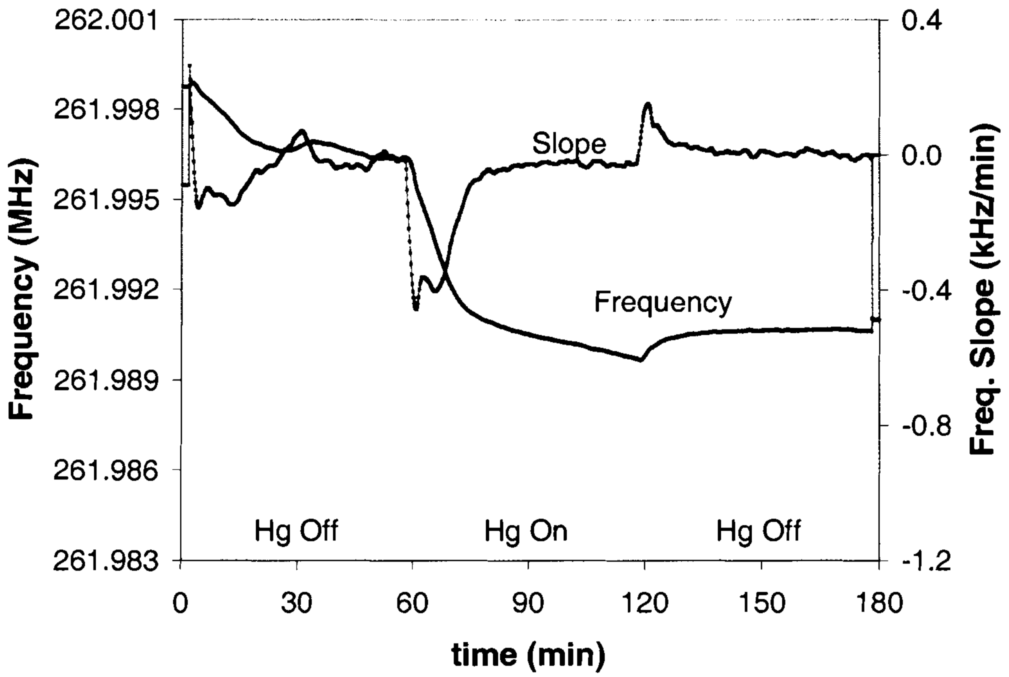

Figure 4.10 Response magnitude and slope for the 500Å gold film to 100 ppb Hg at 50°C.

For the 20 ppb Hg exposures (Figure 4.12) the largest one hour response magnitude and the 2nd largest maximum negative response slope occurred for the 100Å gold film. For the 40 and 80 ppb Hg summary plots (Figures 4.13 and 4.15, respectively) once again the 75Å film produced the largest one hour response magnitude. The 200Å film produced the largest one hour response magnitude for the 60 ppb Hg exposures (Figure 4.14). For the 40, 60, and 80 ppb Hg summary plots, the data showed the trend of decreasing response slope as a function of gold film thickness.

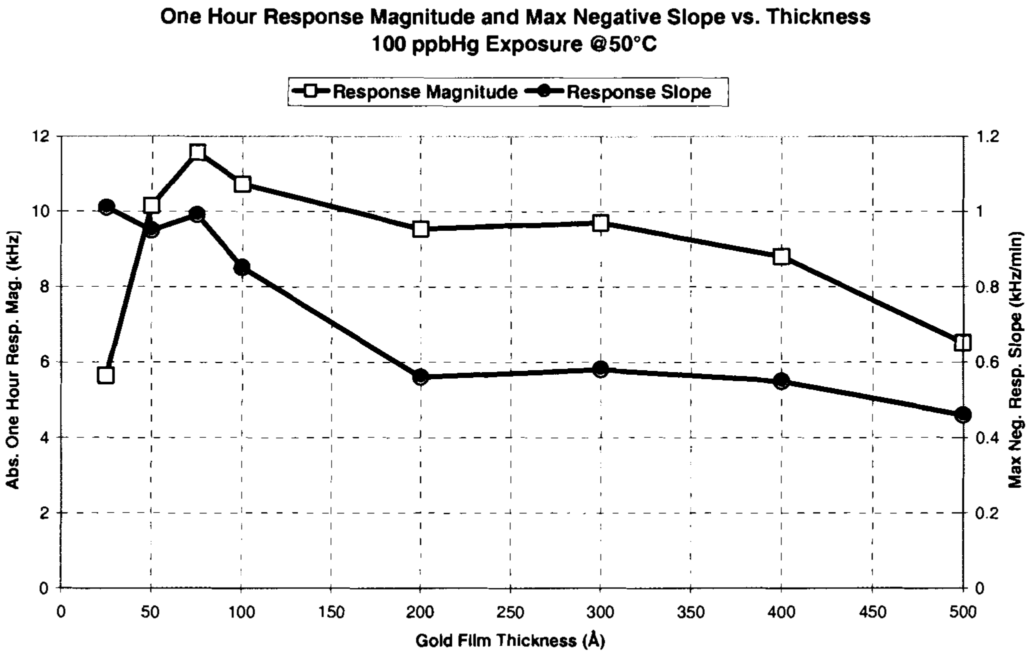

Figure 4.11 Absolute response magnitude and maximum negative slope as a function of gold film thickness for 100 ppb Hg at 50°C.

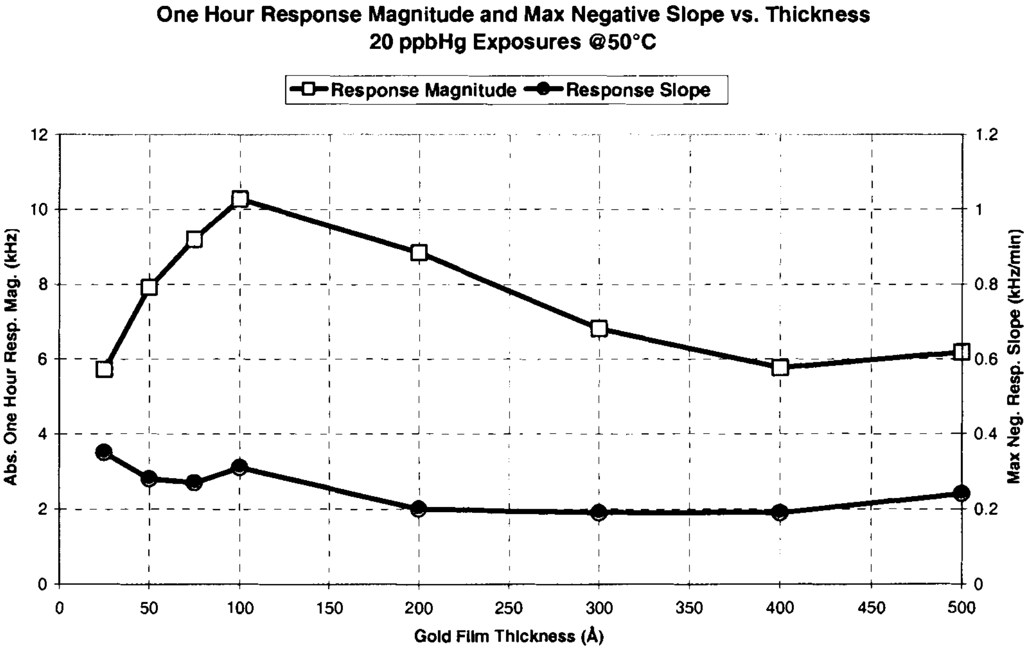

Figure 4.12 Absolute response magnitude and maximum negative slope as a function of gold film thickness for 20 ppb Hg at 50°C.

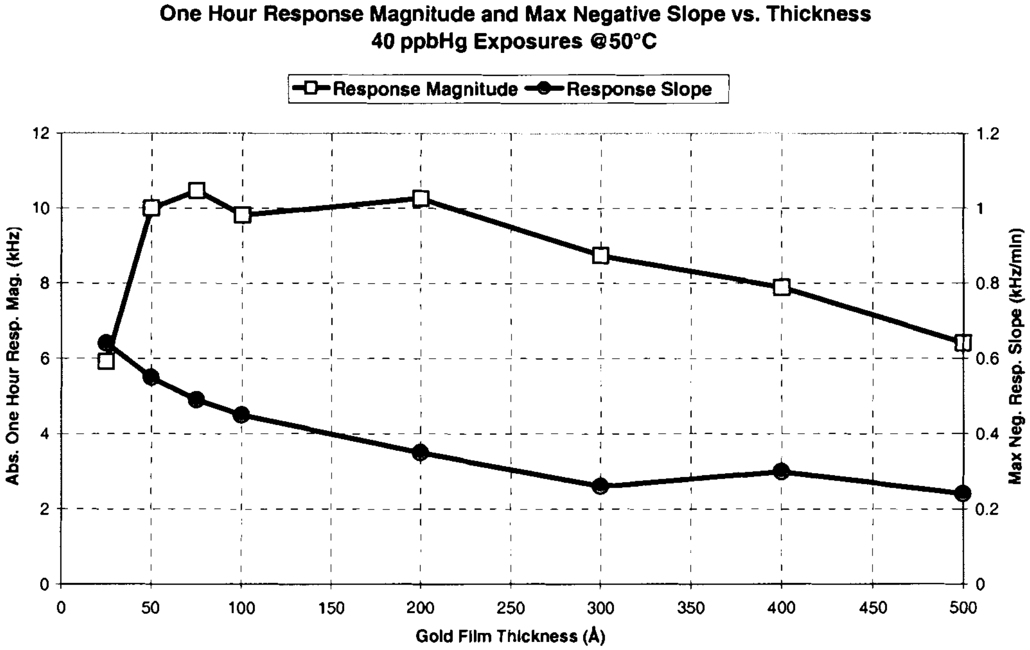

Figure 4.13 Absolute response magnitude and maximum negative slope as a function of gold film thickness for 40 ppb Hg at 50°C.

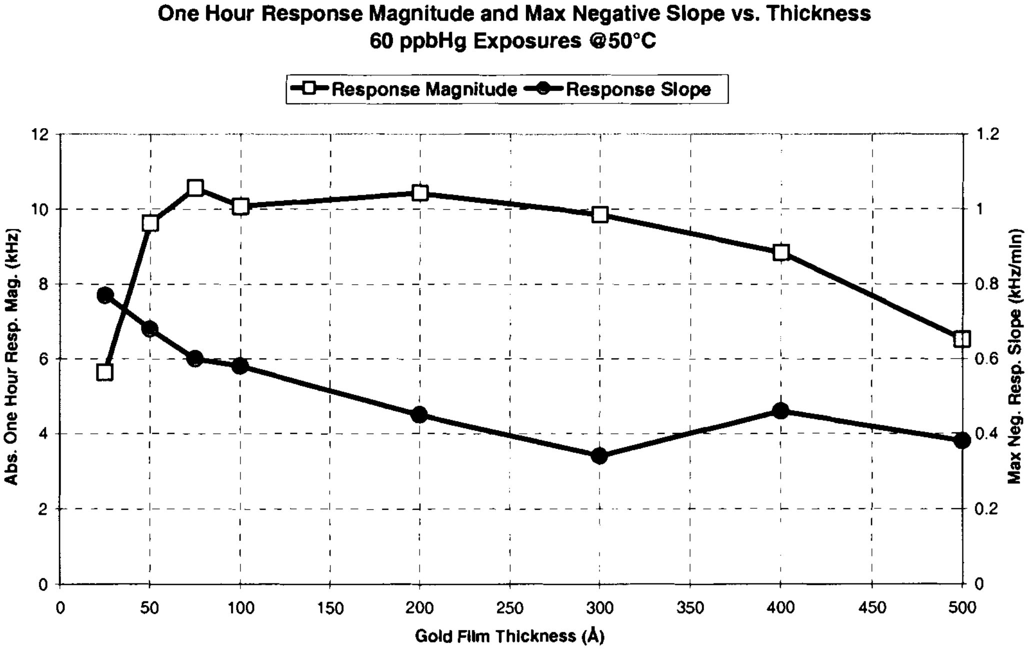

Figure 4.14 Absolute response magnitude and maximum negative slope as a function of gold film thickness for 60 ppb Hg at 50°C.

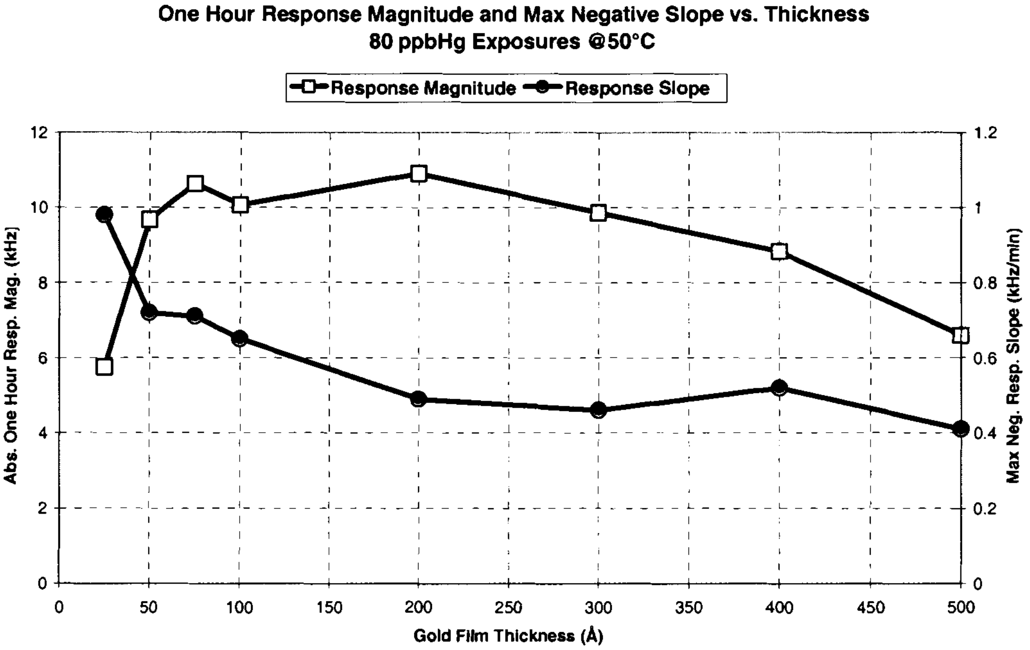

Figure 4.15 Absolute response magnitude and maximum negative slope as a function of gold film thickness for 80 ppb Hg at 50°C.

4.3. Response Magnitude and Slope vs. Concentration

Figure 4.16 shows the 25Å response magnitudes for all the concentrations tested, while Figure 4.17 shows the response slopes. Although very sensitive with plenty of response slope, the 25Å film became saturated very quickly. Even after only 30 minutes of exposure (Figure 4.17) it was impossible to tell one concentration's response curve from another.

Figure 4.18 shows the 75Å response magnitudes for all the concentrations tested, while Figure 4.19 shows the response slopes. You can see that there is still plenty of response slope with the useful lifetime of the sensor being significantly extended. This is demonstrated by the larger response magnitudes and the wider response slope peaks, especially for the lower concentrations of mercury.

Figure 4.20 shows the 500Å response magnitudes for all the concentrations tested, while Figure 4.21 shows the response slopes. First, there was a drastic reduction in the response magnitude and the smoothness of the shape of the response. This was further stressed by the limited response slopes and the presence of double peaks in the response slope curves.

Figure 4.22 is a summary plot showing the variation in maximum negative response slope as a function of concentration for each thickness. Both the 25 and 75Å films had a measurement resolution of 8.3 (Hz/min)/ppb Hg, while the 500Å film had only 3.1 (Hz/min)/ppb Hg.

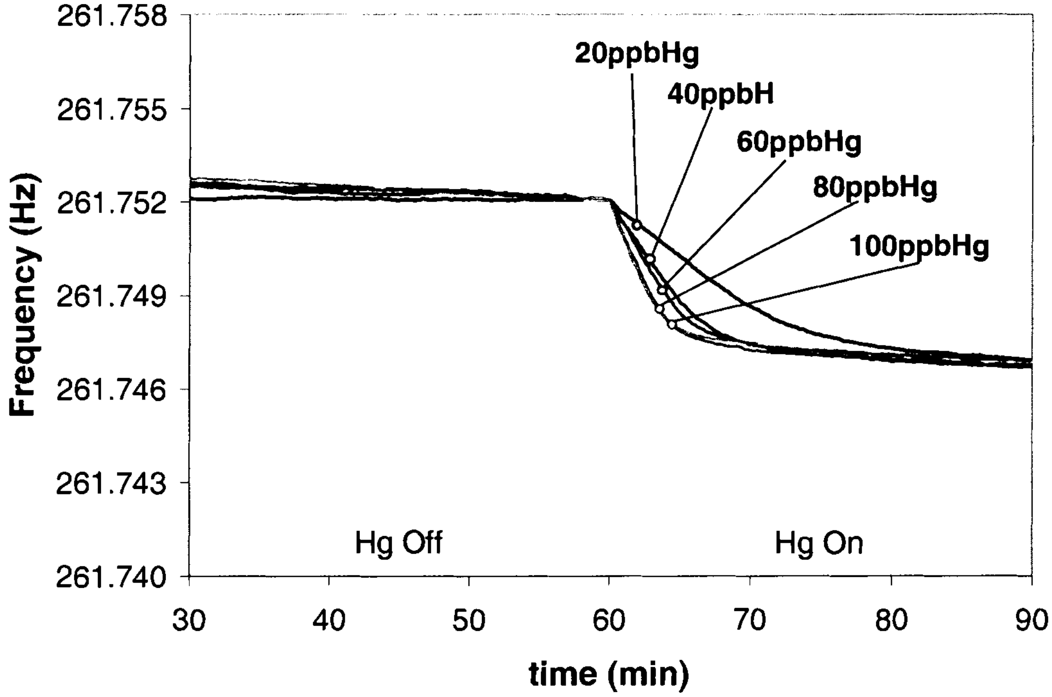

Figure 4.16 Response magnitudes for the 25Å gold film exposed to 20, 40, 60, 80, and 100 ppb Hg at 50°C.

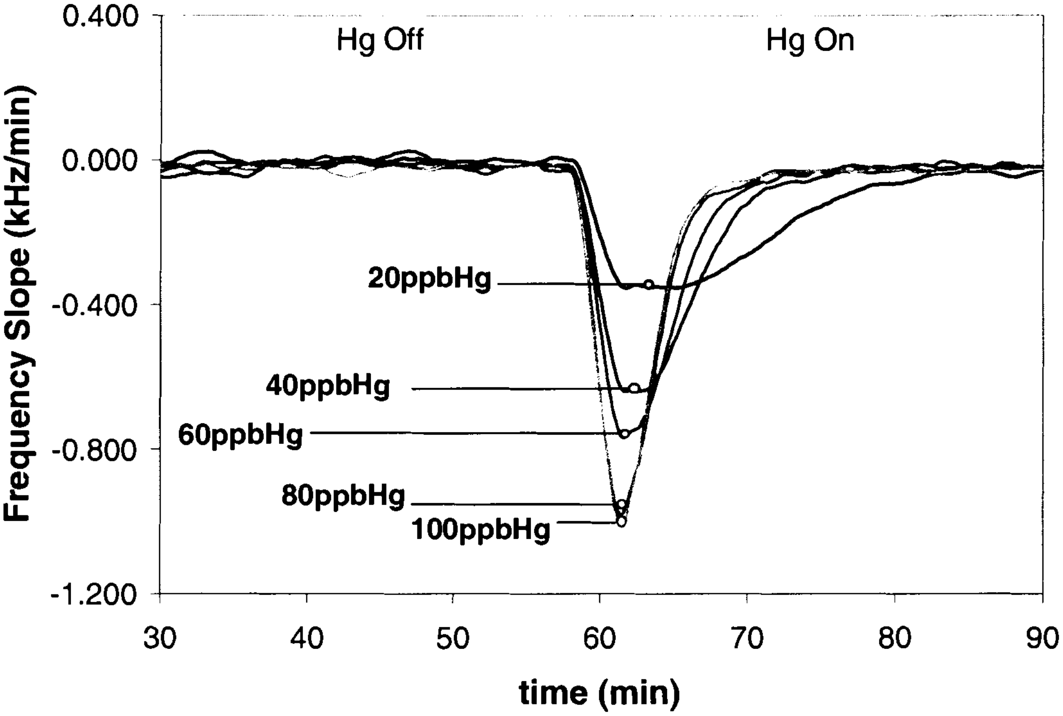

Figure 4.17 Response slopes for the 25Å gold film exposed to 20, 40, 60, 80, and 100 ppb Hg at 50°C.

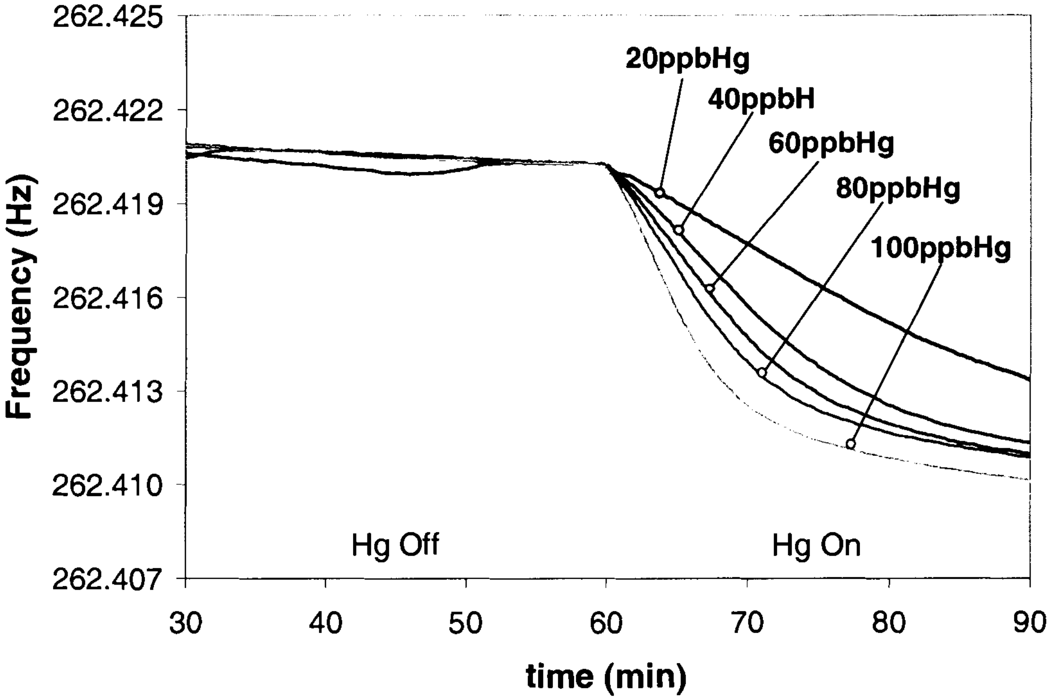

Figure 4.18 Response magnitudes for the 75Å gold film exposed to 20, 40, 60, 80, and 100 ppb Hg at 50°C.

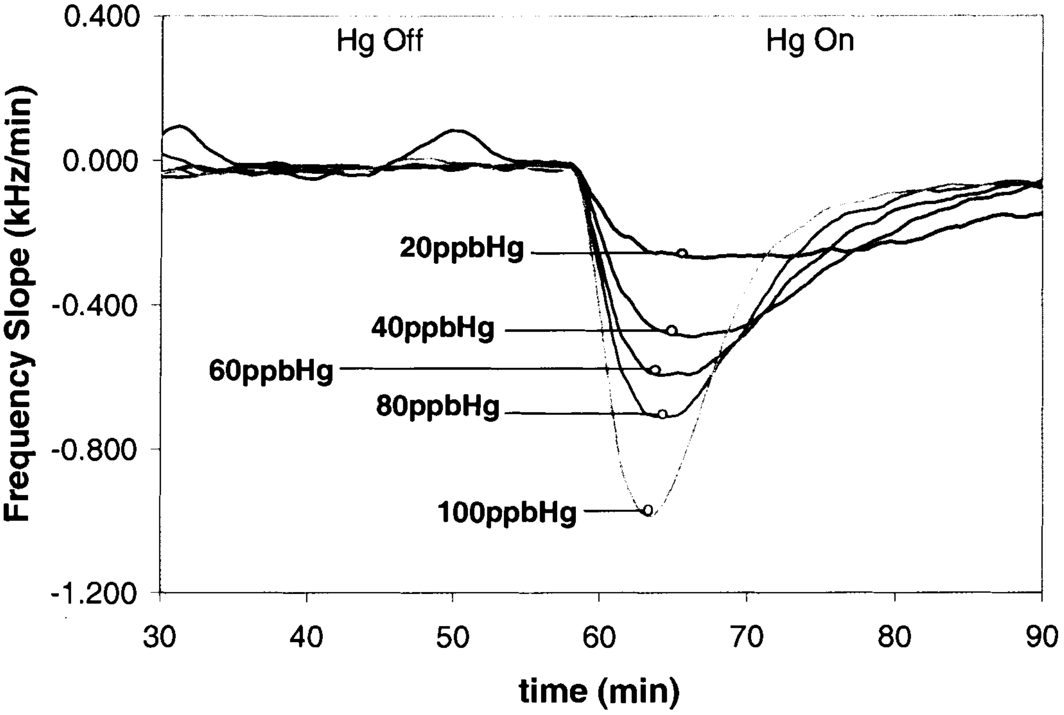

Figure 4.19 Response slopes for the 75Å gold film exposed to 20, 40, 60, 80, and 100 ppb Hg at 50°C.

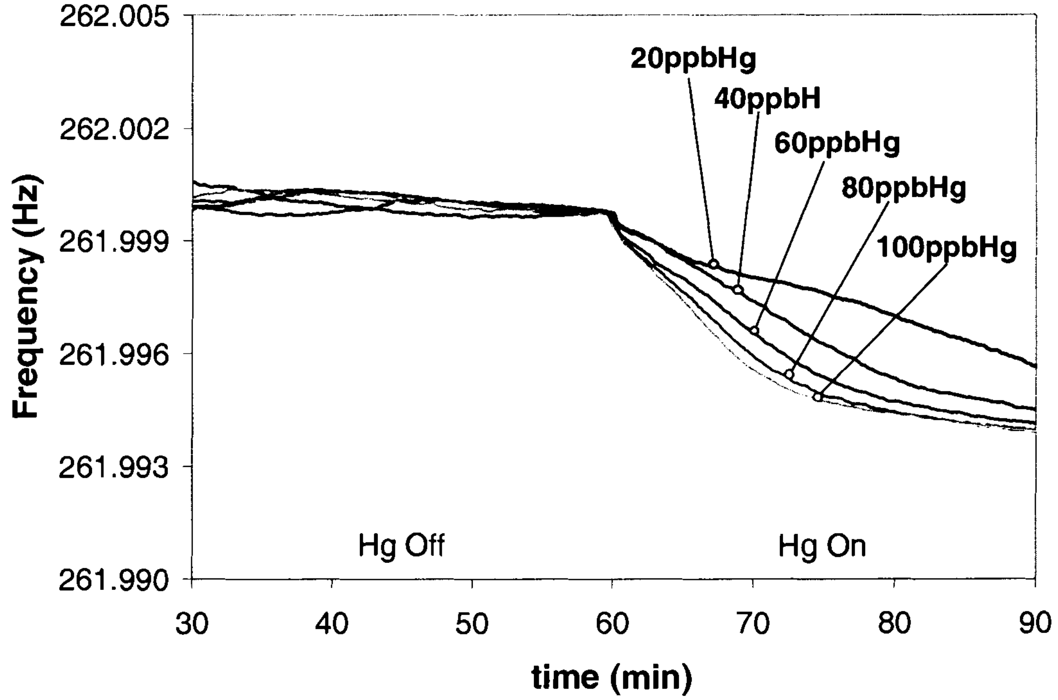

Figure 4.20 Response magnitudes for the 500Å gold film exposed to 20, 40, 60, 80, and 100 ppb Hg at 50°C.

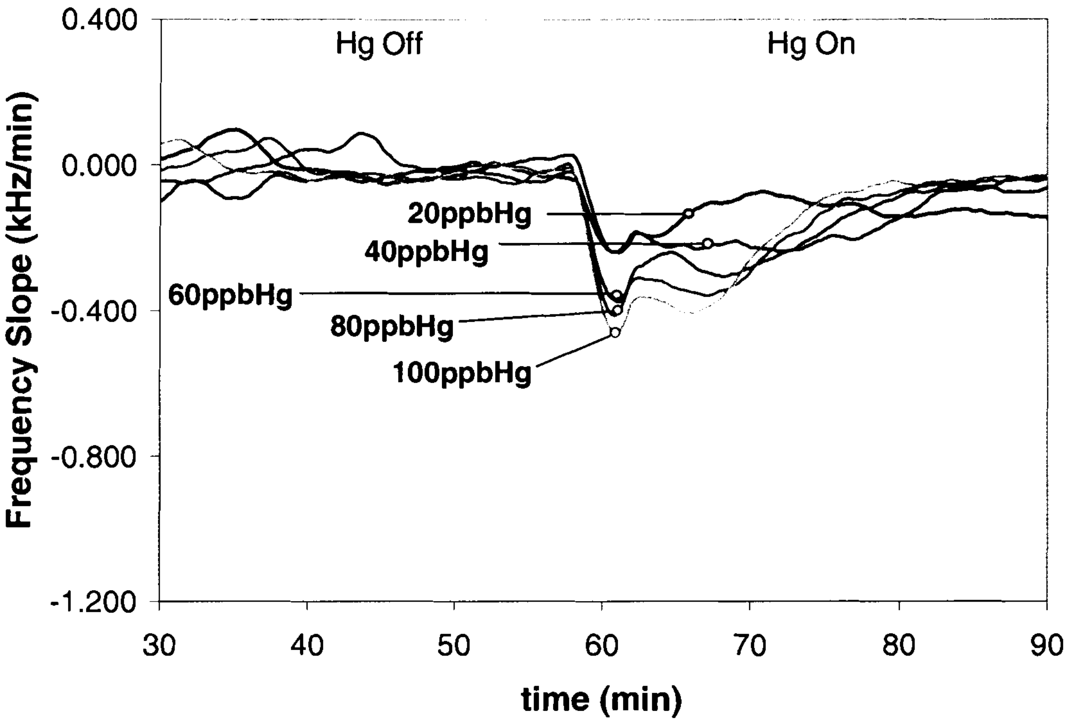

Figure 4.21 Response slopes for the 500Å gold film exposed to 20, 40, 60, 80, and 100 ppb Hg at 50°C.

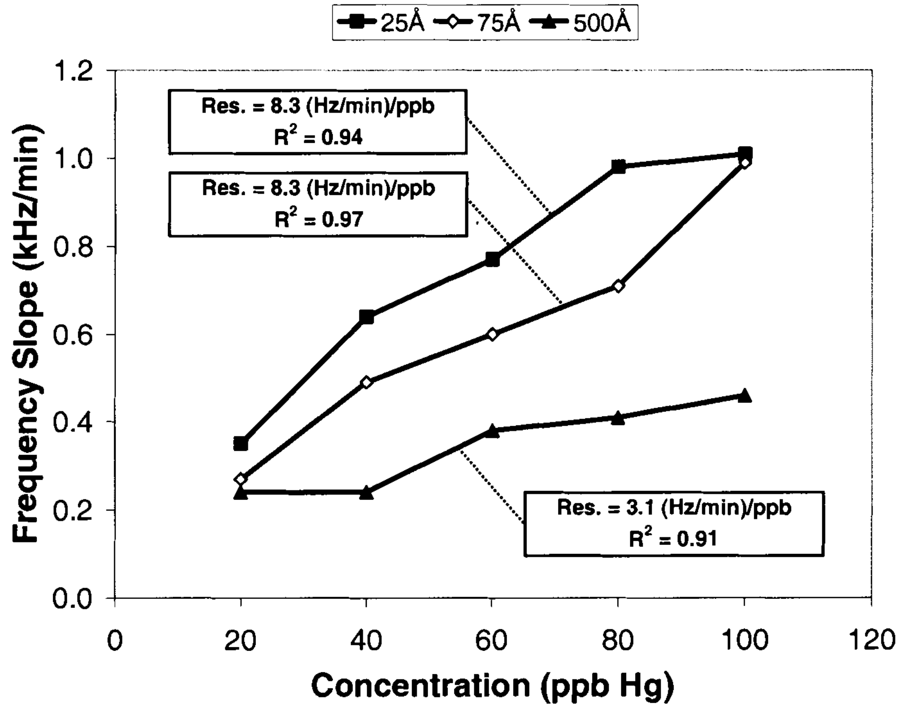

Figure 4.22 Absolute maximum negative response slope as a function of concentration for 25, 75, and 500Å gold films at 50°C.

4.4. Discussion of the Results

Upon exposure to mercury, the SAW response was driven by the changing mechanical properties of the gold film. For all the film thicknesses the response was dominated by mass loading, as witnessed by the decrease in oscillation frequency (Figures 4.3 to 4.10). The thicker films (200 to 500Å) had an additional stiffening effect that reduced the overall magnitude and slope response.

Looking at the summary curves for the response magnitude and slope as a function of thickness (Figures 4.11 to 4.15), some general trends are obvious. Evaluating the response slope first, we see that the response slope as a function of thickness decreased from 25 to 200Å and then leveled off up to 500Å. This would suggest that as the gold film thickness increased, the accessibility of the mercury to the available gold surface decreased. This was most likely related to the packing structure of the gold film as a function of gold film thickness. In the range of 200 to 500Å, the gold films were continuous and the structures of the gold films were probably very similar.

Looking at the response magnitude as a function of gold film thickness, we see that it dramatically increased going from 25 to somewhere in the range of 75 to 100Å, where it peaked. A slight further reduction in response magnitude followed by a general leveling off occurred for films in the range of 100 to 300Å. Finally, for the thickest films in the range of 300 to 500Å, the response magnitude was significantly reduced even more.

For the first range of film thicknesses, 25 to 100Å, we can most likely attribute the increasing sensitivity trend to the increased mass loading (surface adsorption) due to the growing surface area. Hemispherical growth of the gold islands as the film thickness increases would result in a maximum sensitivity peak corresponding to the moment when the hemi-spherical islands are just touching each other (Figure 2.7 : Case B). This film thickness, $h_{\max}$, corresponds to a film thickness in the range of 75 to 100Å. Also for this range, elastic stiffening would be minimal for a non-continuous film.

For the second range of film thicknesses, 100 to 300Å, a slight increase in film thickness resulted in a further decrease in sensitivity. As the hemi-spherical gold islands come together and become continuous there is a further reduction in the available surface area resulting in a reduction in mass loading (surface adsorption). Leveling off of the sensitivity indicates that the available surface area had become constant or in other words, the surface structure was very similar for the film thicknesses in the upper part of that range. Elastic stiffening, is just starting to come into play for the upper part of this range and could account for additional loss is sensitivity.

For the last range of film thicknesses, 300 to 500Å, the majority of the response is still due to mass loading, but it is accompanied by a detrimental elastic stiffening response. It is believed that the surface structure and therefore, surface area available for mass loading is relatively constant for films in the range of 200 to 500Å. If this is the case, then the additional loss in sensitivity must be due to elastic stiffening. Also, for the thicker films, the further reduction in response magnitude did not coexist with a corresponding decrease in the response slope as a function of gold film thickness. This suggests that elastic stiffening may have been responsible for the reduction of response magnitude.

The sensor's ability to detect mercury concentration was demonstrated for the 25, 75, and 500Å gold films shown in Figure 4.22. Technically, any gold film thickness could be used to quantify mercury concentration once a slope vs. concentration curve is obtained. Practically, the accuracy of the sensor is determined, in part, by the measurement resolution (change in slope as a function of concentration). As shown, the 25 and 75Å gold films yielded a measurement resolution of 8.3 (Hz/min)/ppb Hg, while the 500Å film yielded a much smaller resolution of 3.1 (Hz/min)/ppb Hg. However, because of the smaller thickness, the useful lifetime of the 25Å gold film was limited.

This is further demonstrated by Figure 4.23, where the 25Å gold film slope vs. concentration is plotted for different amounts of time into the exposure. After 2.5 minutes of exposure to mercury, the slope as a function of mercury was fairly linear, with a measurement resolution of 6.8 (Hz/min)/ppb Hg, but it appears that the 100ppb Hg data point was moving away from the linear line already. After 5.0 minutes of exposure, only the 20ppb Hg data point was still on the original linear line and the sensor was useless for concentrations above 20ppb Hg. After 7.5 minutes, the sensor was completely useless for any concentration of mercury greater than 20ppb Hg.

Figure 4.24 shows the 50Å gold film slope vs. concentration for different amounts of time into the exposure. After 2.5 minutes of exposure, the slope as a function of concentration was linear with a measurement resolution of 8.1 (Hz/min)/ppb Hg, but still suffered from a limited useful lifetime. After 5.0 minutes of exposure, only concentrations between 20 to 40 ppb Hg were reliably determined. After 7.5 minutes of exposure only the 20ppb Hg exposure was reliably determined.

Figures 4.25 and Figures 4.26 show the 75 and 100Å gold film slope vs. concentration plots, respectively. For the 75Å gold film, the measurement resolution was 8.7 (Hz/min)/ppb Hg, while for the 100Å film the resolution was slightly reduced to 6.4 (Hz/min)/ppb Hg. For both gold film thicknesses, the whole range of concentrations up to 100ppb Hg was determined fairly accurately up to 5 minutes into the exposure. After 7.5, 10, and 15 minutes of exposure only concentrations 60ppb Hg and below, 40ppb Hg and below, and 20ppb Hg and below were determined, respectively.

The 500Å gold film slope vs. concentration plots are shown in Figure 4.27. The whole range of concentrations were determined up to 7.5 minutes of exposure and even after 10 minutes of exposure concentrations 80ppb Hg and below were determined. Unfortunately, the measurement resolution was only 2.6 (Hz/min)/ppb Hg, which limited how accurately the lower concentrations of mercury could be determined.

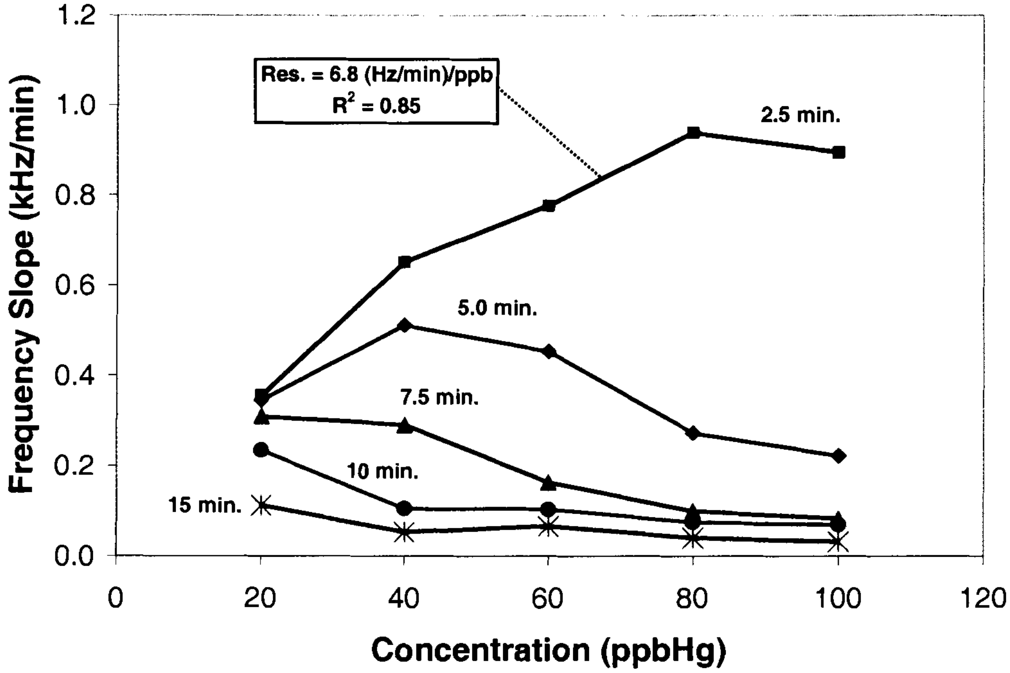

Figure 4.23 Absolute negative response slope as a function of concentration for the 25Å gold film with times of 2.5, 5, 7.5, 10, and 15 minutes into the exposure.

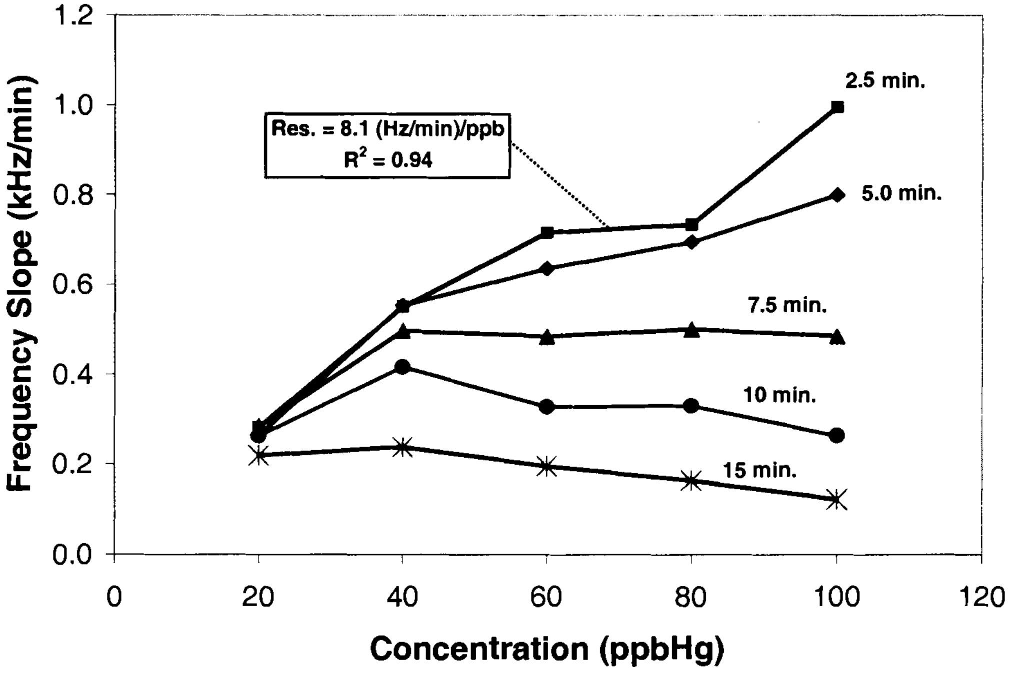

Figure 4.24 Absolute negative response slope as a function of concentration for the 50Å gold film with times of 2.5, 5, 7.5, 10, and 15 minutes into the exposure.

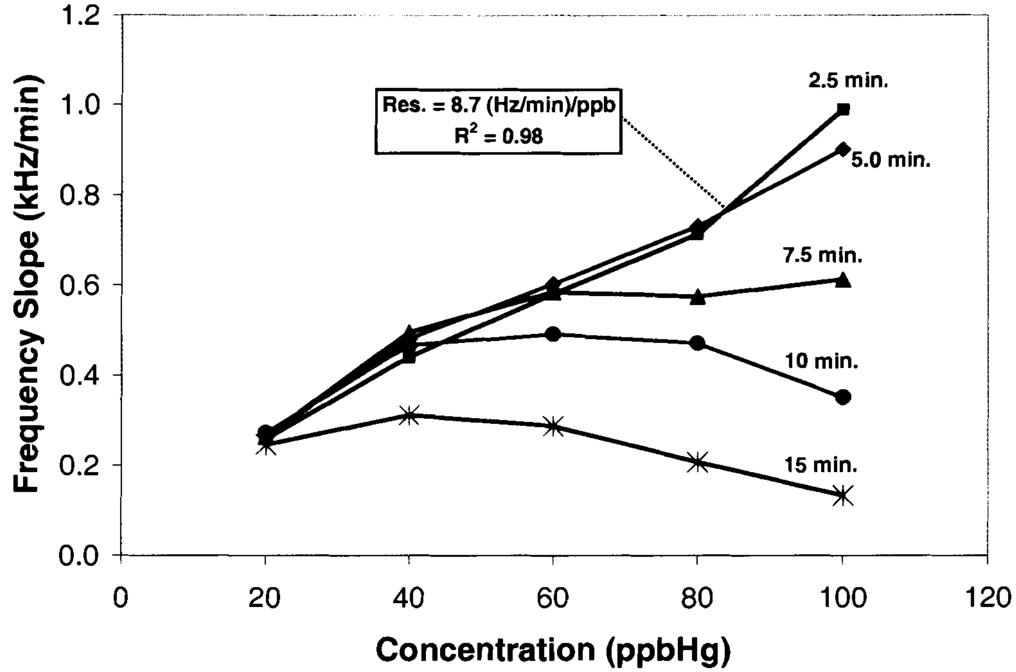

Figure 4.25 Absolute negative response slope as a function of concentration for the 75Å gold film with times of 2.5, 5, 7.5, 10, and 15 minutes into the exposure.

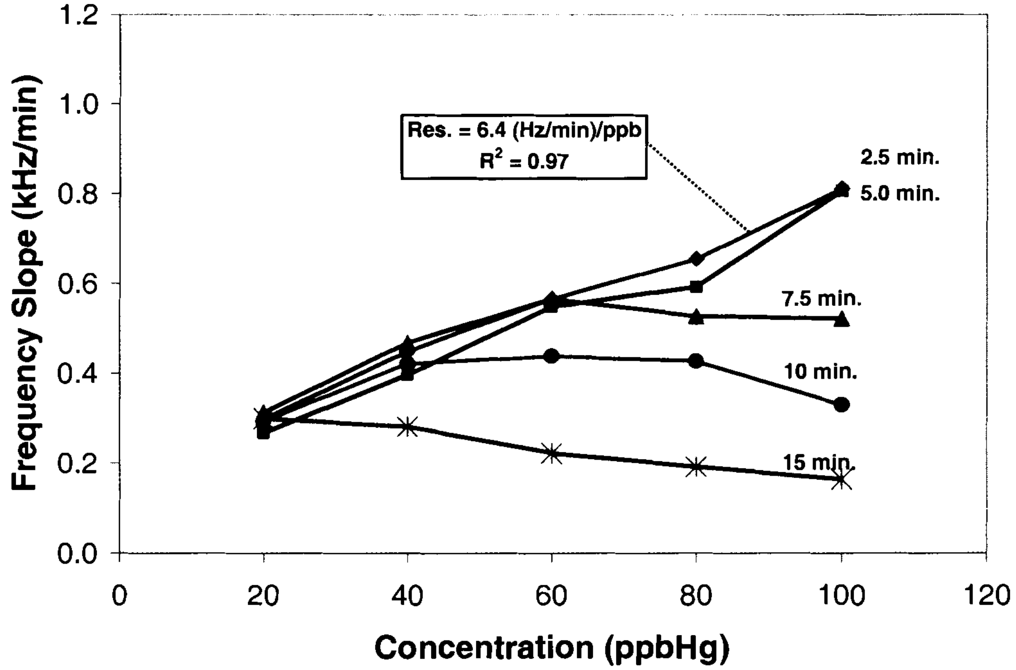

Figure 4.26 Absolute negative response slope as a function of concentration for the 100Å gold film with times of 2.5, 5, 7.5, 10, and 15 minutes into the exposure.

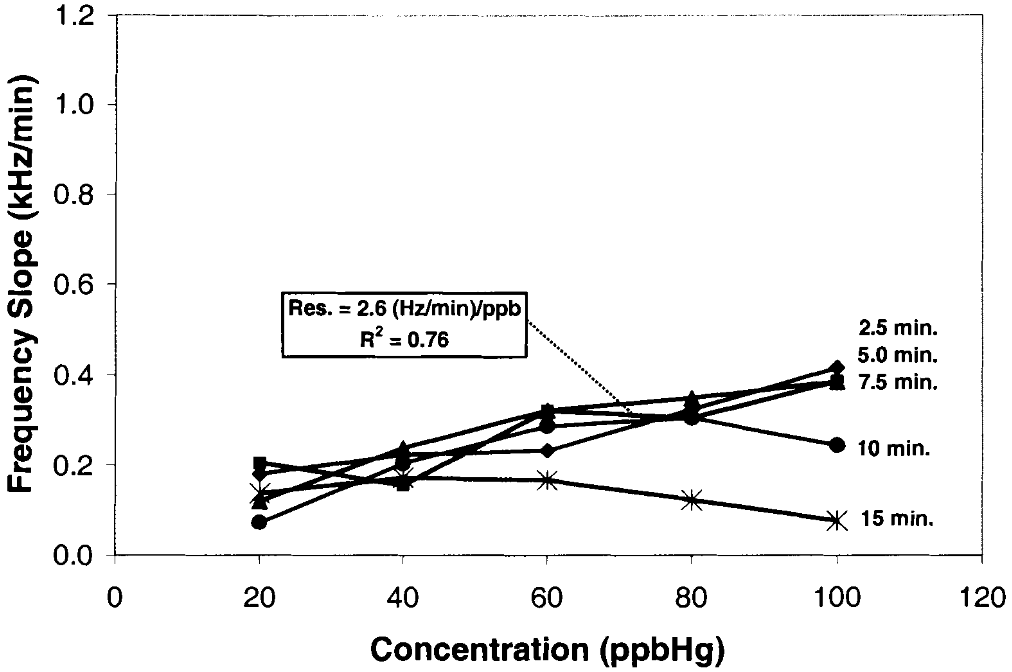

Figure 4.27 Absolute negative response slope as a function of concentration for the 500Å gold film with times of 2.5, 5, 7.5, 10, and 15 minutes into the exposure.

Chapter 5. SUMMARY, CONCLUSIONS AND FUTURE WORK

5.1. Summary

A SAW-based sensor for the detection of gaseous mercury has been described. In Chapter 1, the impact of mercury pollution was reviewed and the need for an ambient, real-time monitor for elemental mercury was defined. Then, a detailed review of the history and operation of the various mercury microsensors was presented, along with the advantages and disadvantages of using them.

Chapter 2 described the operation of the SAW mercury sensor. First the physical layout and the operation of a simple delay line was presented. Following, the split-finger transducer was introduced as a means of reducing a second-order effect called the triple-transit response. Next the experimental SAW delay line design parameters were illustrated and the conditions necessary for creating an oscillator configuration were described. The use of a thin gold film as a sensing mechanism for mercury was reviewed and the mechanical perturbations experienced by the SAW were explained. Based on these mechanical perturbations, a simple model was developed to explain the overall trend in the mercury sensor's responses as a function of the gold film thickness.

Chapter 3 described in detail the experimental setup surrounding the SAW sensing element. The design and construction of the gaseous mercury delivery system were illustrated and thoroughly explained. A sampling method for exposing the SAW sensor to gaseous mercury was presented and shown to reduce the sensor's sensitivity to flow rate changes and pressure spikes caused by the mercury delivery system. The packaging of the SAW mercury sensor with all the components necessary for exciting the SAW, maintaining the operating temperature, and delivering the test gas to the sensing element was then described. Next the oscillator circuitry was illustrated and its operation was explained. The micro-heater, the RTD, and their corresponding circuits were shown and their operation was discussed. Finally, a data acquisition system was described showing how the various parts of the experimental setup were interfaced and controlled.

Chapter 4 presented the experimental results acquired with the SAW mercury sensor. The experimental testing protocol was laid out, and the procedure for processing and evaluating the data was explained. Following, a detailed evaluation of the response magnitude and slope as a function of the gold film thickness was presented and summarized. Similarly, a qualitative and quantitative analysis of the response magnitude and slope, as a function of the mercury concentration, ensued. Finally, a discussion of the results revealed the pros and cons of the various film thicknesses tested and determined the optimum film thickness for the SAW mercury sensor.

5.2. Conclusions

Utilizing perturbation theory for mechanical effects, it is known that the SAW is sensitive to both mass loading (frequency decrease) and elastic stiffening (frequency increase). The experimental results presented in this thesis have demonstrated that both of these effects are present and the extent of each of these effects has a strong dependence on the gold film thickness. In general, for thinner films the response was dominated by the mass loading response, while for thicker films the net response was a superposition of both mass loading and elastic stiffening.

For a sensing film from 25 to somewhere in the range of 75 to 100Å, the response magnitude was dominated by mass loading and increased with respect to the gold film thickness, while the stiffening response was found to be negligible. For a sensing film in the range of 100 to 300Å, the response magnitude was still dominated by mass loading, but significantly reduced. For sensing films in the range of 200 to 500Å, the majority of the response magnitude was still attributed to mass loading, but an accompanying stiffening response resulted in a reduction in the overall response.

The explanation of this behavior is relatively straightforward, and a simple model was developed to explain the sensor response. For thin films which form hemispherical gold islands, the surface area, and therefore mass of surface mercury, increased with respect to the film thickness. The maximized surface area occurs when the hemispherical gold islands are just touching each other. Over this range, $0 < h < h_{\max}$, where $h_{\max}$ corresponds to the film with maximized surface area in the range of 75 to 100Å, increasing thickness will result in increased adsorption.

For a slightly thicker film, $h > h_{\max}$, the mass loading (surface adsorption) is reduced as the hemispherical gold islands grow into each other resulting in a reduction in the available surface. Over this range, $h > h_{\max}$, where h corresponds to a film in the range of 100 to 300Å, increasing thickness will result in an initial decrease followed by a leveling in the amount of adsorption.

For $h >> h_{\max}$, corresponding to a film in the range of 300 to 500Å, the surface mercury layer remains essentially constant and the sensitivity to the surface mercury layer is unaffected by increasing thickness.

Within the bulk of the film, the small amount of absorbed mercury increases mass only slightly, but dramatically increases the film stiffness. For the thinner films (25 to 300Å) the amount of stiffening is negligible, but for the thicker films (300 to 500Å) the amount of stiffening significantly reduces the overall sensor response.

The net sensor response is a superposition of mass loading (surface adsorption) and elastic stiffening (diffusion into the bulk). The sensitivity increases for increasing thicknesses up to $h_{\max}$, due to mass loading effects of the increased surface area outweighing the elasticity effects of increased bulk volume, while the sensitivity decreases for increasing thickness for films in the range of 300 to 500Å, due to the only slight increase in film mass being offset by the increase in stiffness.

Observation of the response slope across the whole range of thicknesses also demonstrated some thickness dependence. The rate at which the mercury absorbed onto the gold film surface decreased with respect to the film thickness as it approached and became a continuous film. The packing structure of the gold films should become much tighter and less accessible as they become continuous, accounting for the reduction in the absorption rate.

For films larger than this continuous film thickness (100 to 200Å), the absorption rate was found to be almost constant up to 500Å. One would expect the structures of the films in the range of 200 to 500Å to be very similar, accounting for the almost constant absorption rate across the upper range of film thicknesses tested.

Evaluation of the response slope as a function of mercury concentration showed some very interesting results as well. First, it can be stated that any gold film thickness could have been used to detect mercury because all the film thicknesses demonstrated fairly good linearity for the response slope as a function of mercury concentration. The limitations, however, were determined by the measurement resolution (change in slope as a function of concentration) and the useful lifetime of the sensor.

For the 25Å gold film, the measurement resolution was good at 8.3 (Hz/min)/ppb Hg, but the lifetime was short due to the limited amount of gold surface area. Even after only 2.5 minutes of exposure, 100 ppb Hg exposure could not be resolved. On the other hand, the 500Å gold film had a long lifetime, but the additional stiffening effect degraded the measurement resolution to only 3.1 (Hz/min)/ppb Hg. This severely reduced the accuracy to which the concentration could be determined.

The best combination of lifetime and measurement resolution was achieved with the 75 and 100Å gold films. For the 75Å gold film, the measurement resolution was 8.7 (Hz/min)/ppb Hg, while for the 100Å film the resolution was only slightly reduced to 6.4 (Hz/min)/ppb Hg. For both gold film thicknesses, the whole range of concentrations up to 100ppb Hg could be determined fairly accurately up to 5 minutes into the exposure. Even after 7.5 minutes of exposure, concentrations of 60 ppb Hg and below could be determined.

In conclusion, this thesis has demonstrated that the SAW delay line combined with a gold sensing film is an excellent means of detecting and quantifying low concentrations of gaseous mercury. By selecting a gold film thickness in the range of 75 to 100Å, the lifetime and measurement resolution are optimized by maximizing the mass loading response, while minimizing the elastic stiffening effect.

5.3. Future Work

A great deal of work still needs to be done in the areas of engineering, chemistry, and surface science in order to fully understand the mechanisms behind the operation of the SAW mercury sensor. Also, a carefully designed set of experiments could truly demonstrate the full capabilities of the SAW mercury sensor across a much wider range of concentrations.

The first task should be the layout of a temperature compensated dual delay line structure. Previous work to create a dual delay line SAW sensor has proven to be difficult due to the fact that the turnover temperature of the SAW will shift down in frequency when a metal is deposited onto its delay line [48]. For the mercury sensor, the best dual delay line solution is to deposit identical materials with identical thicknesses in such a way that only the sensor delay line will be exposed to the mercury. First a gold film should be deposited onto the reference delay line. Next, a SiO_2 passivation layer should be deposited over both the reference and sensor delay lines. Finally, another gold film with the same thickness as the reference should be deposited onto the sensor delay path on top of the SiO_2 passivation layer. This method ensures that both delay lines have identical materials and turnover temperatures, while only allowing the sensor delay line to be exposed to the gaseous mercury [49].

Additionally, a RTD on the top surface and a heater on the bottom surface of the dual delay line SAW could simplify the packaging considerably. Other improvements could be made to shrink the overall size of the sensor packaging and also the gas chamber.

In the area of surface science, it would be a great advantage if the gold sensing films could be studied using atomic force microscopy (AFM), scanning tunneling microscopy (STM), and Auger spectroscopy. AFM and STM could help in identifying how the film structure will change as a function of the film thickness and deposition methods. Knowing this information prior to gaseous mercury exposure could be instrumental to understanding why one sensor response is better or different than another. After exposure to mercury, the various gold films could be evaluated with Auger spectroscopy to qualitatively determine the penetration depths of the mercury as well as the relative amounts with respect to the whole set of sensing films.

Understanding the chemistry involved in the mercury/gold interaction may give insight into understanding the shape of the sensor responses. Looking closely at the magnitude responses shown in Figures 4.3 to 4.10, the responses actually have two very distinctive slopes. The first, initial, slope is most likely a factor of the mass loading caused by the adsorption of mercury onto the gold surface, while the much slower secondary slope is most likely driven by the diffusion of mercury into the bulk of the gold film. Research into the literature for constants related to the adsorption and absorption of mercury onto and into gold could be compared to the time constants extracted from the sensor responses.

Finally, the sensor needs to be more thoroughly characterized. Once again, various film thicknesses should be utilized (25 to 2000Å) across a much wider temperature range (25 to 150°C) and much wider concentration range (1, 10, 100, and 1000 ppb Hg). A carefully designed set of experiments may give significant insight into the mercury/gold interaction as a function of thickness, temperature, and concentration.

For example, the data presented in this thesis demonstrated that mass loading was the dominant mechanism for all the gold film thicknesses tested at 50°C, while elastic stiffening was present for films 200Å and greater. If the operating temperature was reduced to room temperature, could we expect the level of mass loading to increase and the level of elastic stiffening to decrease? If the operating temperature was increased to 100°C, could we expect the level of mass loading to decrease and the level of elastic stiffening to increase? And finally, if we tested a high enough concentration, utilized the appropriate film thickness, and maintained an optimum operating temperature could we achieve a SAW mercury sensor response that was dominated by elastic stiffening resulting in an increasing frequency response?

Clearly, there is a significant amount of work that still needs to be done in the areas of surface science and chemistry in addition to the engineering in order to fully understand the mechanisms behind the SAW mercury sensor.

BIBLIOGRAPHY

1. United States Environmental Protection Agency, "Mercury Study Report to Congress", EPA-452/R-97-003, Dec. 1997.

2. S.G. Gilbert, K.S. Grant-Webster, “Neurobehavioral Effects of Developmental Methylmercury Exposure”, *Environ Health Perspect.*, 103(Suppl 6), 1996.

3. P.M. Rodier, “Vulnerable Periods and Processes during Central Nervous System Development”, *Environ Health Perspect.*, 102(Suppl 2), 1994.

4. T.D. Brown, D.N. Smith, R.A. Hargis, W.J. O’Dowd, “Mercury Measurement and Its Control: What We Know, Have Learned, and Need to Further Investigate”, *Critical Review: J. Air & Waste Manage. Assoc.*, PP 1-97, 1999.

5. Clean Air Act Amendments of 1990(CAA), section 112(n)(1)(B).

6. R. Puk, J. Weber, “Critical Review of Analytical Methods for Determination of Inorganic Mercury and Methylmercury Compounds”, *Appl. Organometallic Chem.*, 8, 293, 1994.

7. R.D. Jones, M.E. Jacobson, R. Jaffe, J. West-Thomas, C. Arfstrom, A. Alli, “Method Development and Sample Processing of Water, Soil, and Tissue for the Analysis of Total and Organic Mercury by Cold Vapor Atomic Fluorescence Spectrometry”, 80, 1285, 1995.

8. M. Aceto, A. Foglizzo, E. Mentasti, G. Sacchero, C. Sarzanini, “Mercury Speciation in Biological Samples”, 60, 1-13, 1995.

9. M. Schintu, F. Jean-Caurant, J-C. Amiard, “Organo-mercury Determination in Biological Reference Materials: Application to a Study on Mercury Speciation in Marine Mammals off the Faoe Islands”, *Ecotox. Envir. Safety*, 24, 95, 1992.

10. S. Rapsomanikis, M. Andreae, “New Speciation Approaches in the Biogeochemical Cycles of Organometallics in the Environment”, *Intern. J. Envir. Chem.*, 49, 43, 1992.

11. R. Puk, J. Weber, “Determination of Hg(II), CH_3Hg, $(CH_3)_2Hg$ and $(C_2H_5)_2Hg$ by Hydride Generation, Cryogenic Trapping and Atomic Absorption Spectrometric Detection”, *Anal. Chem. Acta.*, 292, 175, 1994.

12. J.W. Robinson, “Atomic Spectroscopy”, 2nd Ed., Marcel Dekker, Inc., 1996.

13. V. Sychra, V. Svoboda and I. Rubeska, “Atomic Fluorescence Spectoscopy”, Van Nostrand Reinhold Company Ltd, 1975.

14. W. G. Schrenk, “Analytical Atomic Spectroscopy”, Plenum Press, 1975.

15. W.L. Clevenger, B.W. Smith, and J.D. Winefordner, “Trace Determination of Mercury: A Review”, *Critical Reviews in Analytical Chemistry,* 27(1):1-26, 1997.

16. J.J. McNerney, P.R. Buseck and R.C. Hanson, “Mercury Detection by Means of Thin Gold Film”, *Science*, 178, 611, 1972.

17. Jerome Division of Arizona Instruments, Product Literature.

18. Q. Bristow, “An Evaluation of the Quartz Crystal Microbalance as a Mercury Sensor for Soil Gases”, *J. Geochem. Expl.*, 55, 1972.

19. E.P. Scheide, J.K. Taylor, “Piezoelectric Sensor for Mercury in Air”, *Environmental Science and Technology*, 8, 1097, 1974.

20. E.P. Scheide, J.K. Taylor, “A Piezoelectric Crystal Dosimeter for Monitoring Mercury Vapor in Industrial Atmospheres”, *Am. Ind. Hygiene Ass. Journal*, Dec. 1975.

21. E.P. Scheide, R.B.J. Warner, “A Piezoelectric Crystal Mercury Monitor”, ibid, 745, Sept., 1978.

22. E.P. Scheide, “The Piezoelectric Crystal Mercury Dosimeter”, *Research Frontier*, 47, Jan. 1977.

23. G.G. Guilbault, E.P. Scheide, “Determination of Nanogram Quantities of Mercury in Water with a Gold-Plated Piezoelectric Crystal Detector”, *Anal. Chem. Act.*, 130, 141, 1981.

24. A.N. Mogilevski, A.D. Mayorov, N.S. Stroganova, D.B. Stavrovski, I.P. Galkina, L. Spassov, D. Mihailou, R. Zahariera, “Measurement of the Concentration of Mercury Vapor in Air through a Piezoresonance Method”, *Sensors and Actuators A* 28, 35, 1991.

25. L. Spassov, D.Y. Yankov, A.N. Mogilevski, A.D. Mayorov, “Piezoelectric Sorption Sensor for Mercury Vapors in Air Using a Quartz Resonator”, *Rev. Sci. Instru.* 64, 225, 1993.

26. T. Thundat, E.A. Wachter, S.L. Sharp, R.J. Warmack, “Detection of Mercury Vapor Using Resonating Microcantilevers”, *Appl. Phys. Lett.*, 66, 13, 1995.

27. R. Sauberlich, P. Petter, W. Buff, B. Wall, N. Nindel, “Method and Device for the Concentration of Mercury in Gases”, Patent 00268530A1, Deutsche Demokratische Republik, 1989.

28. J. Andle, J. Munson, R. Roderick, L. French, M. Schweyer, J. Vetelino, C. Watson, J. Foley, A. Bruce, M. Bruce, “Electromechanical Piezoelectric Sensors for Trace Ionic Contaminants”, *IEEE Transactions on Ultrasonics, Ferroelectrics, and Frequency Control*, 45 (5), 1408-1415, 1998.

29. M. Schweyer, J. Andle, D. McAllister, and J. Vetelino, “An Acoustic Plate Mode Sensor for Aqueous Mercury”, *Sensors and Actuators B*, 35-36, 170, 1996.

30. J. Andle, M. Schweyer, J. Munson, R. Roderick, D. McAllister, L. French, J. Vetelino, C. Watson, J. Foley, M. Bruce, A. Bruce, “Electrochemical Piezoelectric Sensors for Trace Ionic Contaminants”, *Proceedings IEEE International Frequency Control Symposium*, 429-434, 1997.

31. M. Schweyer, J. Andle, D. McAllister, L. French, J. Vetelino, “An Acoustic Plate Mode Sensor for Aqueous Mercury”, *Proceedings IEEE Ultrasonics Symposium*, 355-358, 1996.

32. J. Caron, R. Haskell, P. Benoit and J. Vetelino, “SAW Mercury Vapor Sensor”, *IEEE Transactions on Ultrasonics, Ferroelectrics, and Frequency Control* 45 (5), 1392-1397, 1998.

33. R. Haskell, J. Caron, M. Duplisea, J. Ouellette, J. Vetelino, “Effects of Film Thickness on Sensitivity of SAW Mercury Sensors”, *Proceedings IEEE Ultrasonics Symposium*, 429-434, 1999.

34. D.P. Morgan, “Surface-Wave Devices for Signal Processing”, Elsevier Science Publishers, 1991.

35. K. Hashimoto, “Surface Acoustic Wave Devices in Telecommunications”, Springer-Verlag, 2000.

36. B.A. Auld, “Acoustic Fields and Waves in Solids”, Vol II, Wiley Interscience Publication, 1973.

37. R. Lec, R.S. Falconer, Z. Xu, J.F. Vetelino, “Macroscopic Theory of Surface Acoustic Wave Gas Microsensors”, *Proceedings IEEE Ultrasonics Symposium*, 585-589, 1988.

38. J.D. Galipeau, "An Experimental Study of a Surface Acoustic Wave Hydrogen Sulfide Microsensor", Masters Thesis, Univ. of Maine, 1996.

39. D.S. Ballantine, R.M. White, S.J. Martin, A.J. Ricco, E.T. Zellers, G.C. Frye, H. Wohltjen, "Acoustic Wave Sensors : Theory, Design, and Physico-Chemical Applications", Academic Press, 225-228, 1997.

40. A. D'Amico, A. Palma, E. Verona, "Hydrogen Sensor Using a Palladium Coated Surface Acoustic Wave Delay-Line", *Proceedings IEEE Ultrasonics Symposium,* 308-311, 1982.

41. H.F. Tiersten, B.K. Sinha, *Journal of Applied Physics*, 49(1), 87-95 1978.

42. Discussions with Dr. Brian G. Frederick, Thesis committee member and Assistant Professor of Chemistry, Department of Chemistry, University of Maine, Orono.

43. L.J. LeGore, R.J. Lad, J.F. Vetelino, B.G. Frederick, E.A. Kenik, "Aggregation and Sticking Probability of Gold on Tungsten Trioxide Films", Sensors and Actuators B, Vol. 76, No. 1-3, 373-379, 2001.

44. M. Ohring, "The Material Science of Thin Films", Academic Press, 1992.

45. C. Chen, A. Gewirth, "AFM Study of the Structure of Underpotentially Deposited Ag and Hg on Au(111)", *Ultramicroscopy*, 42-44, 437-444, 1992.

46. A. Savitzky, M.J.E. Golay, "Smoothing and Differentiation of Data by Simplified Least Squares Procedures", *Anal. Chem.*, 36, 1627, 1964.

47. F.H. Merkle, C.A. Discher, "Controlled-Potential Coulometric Analysis of N-Substituted Phenothiazine Derivatives", *Anal. Chem.*, 44, 1905, 1972.

48. J.J. Caron, R.B. Haskell, J.C. Andle, J.F. Vetelino, "Temperature Stable Piezoelectric Substrates for SAW Gas Sensors", *Sensors and Actuators, B,* v B35 n (1-3) pt 1, 141-145, 1996.

49. R.B. Haskell, J.J. Caron, "Temperature Compensated Surface-Launched Acoustic Wave Sensor", U.S. Patent 6,378,370, April, 2002.

Appendix A. The Complete Data Set

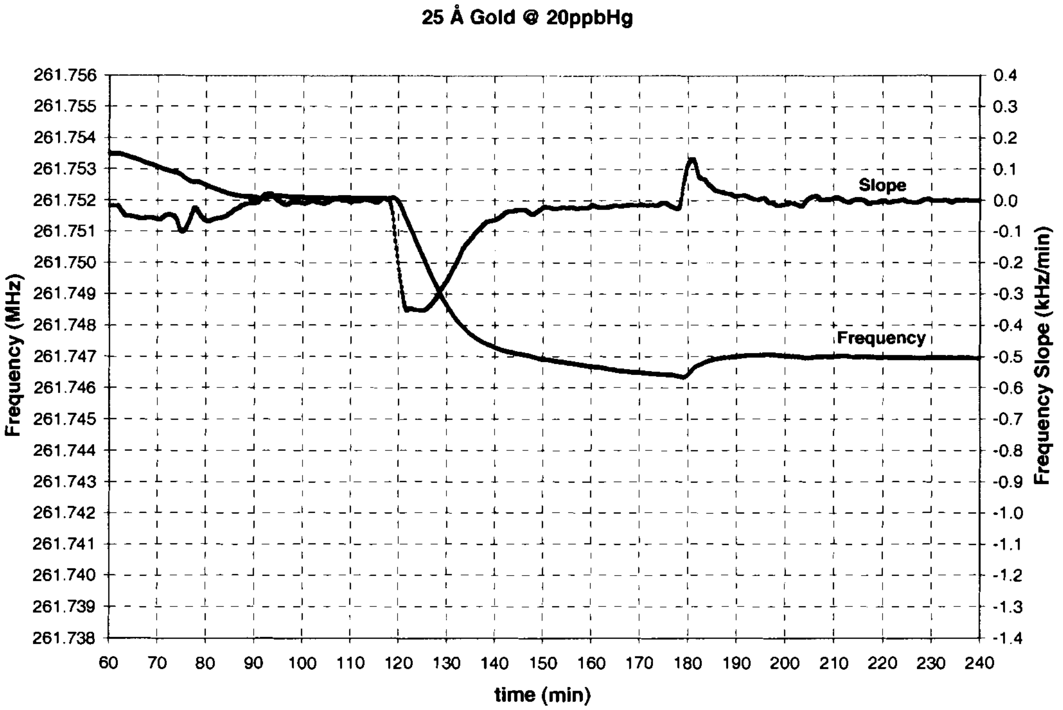

Figure A.1 25 Å gold film exposed to 20 ppb mercury.

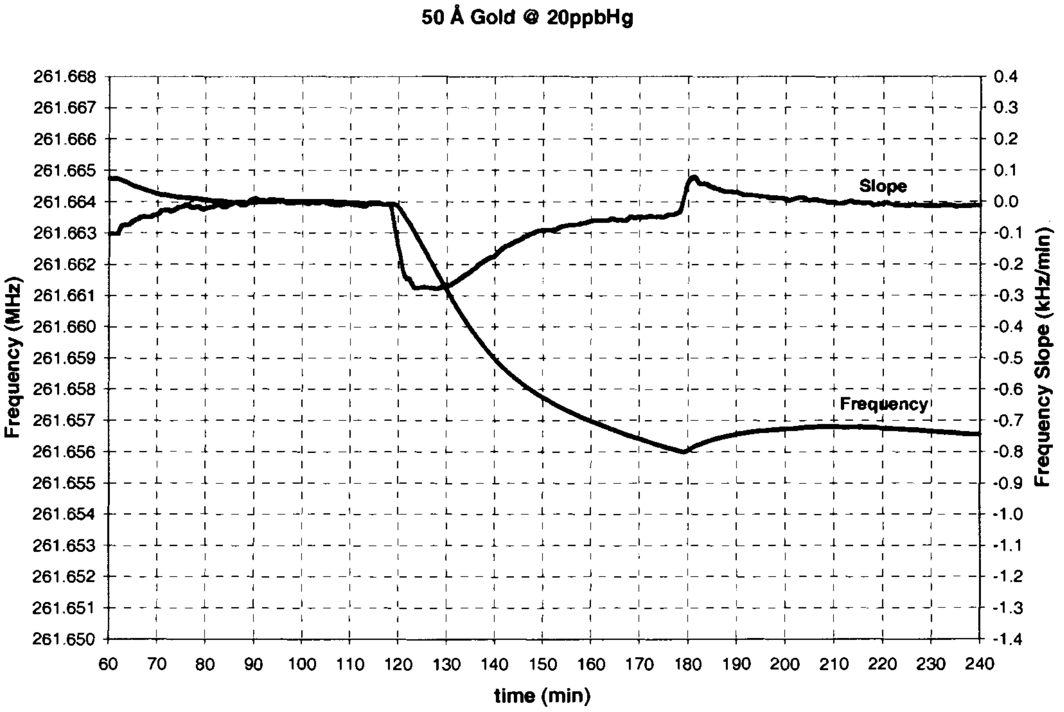

Figure A.2 50 Å gold film exposed to 20 ppb mercury.

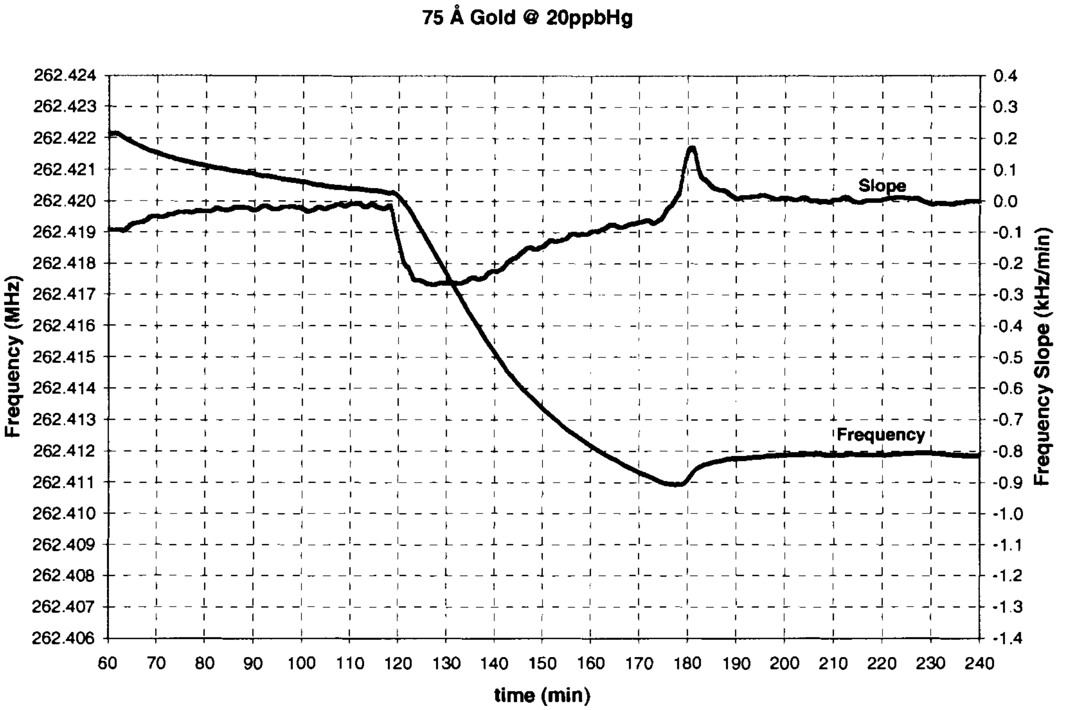

Figure A.3 75 Å gold film exposed to 20 ppb mercury.

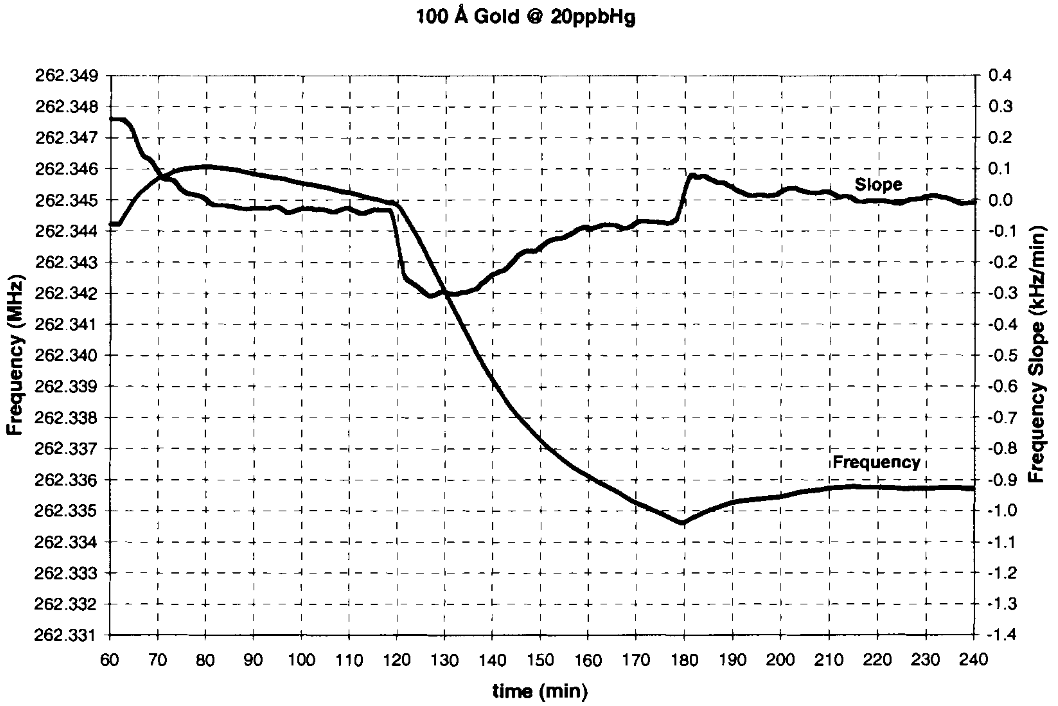

Figure A.4 100 Å gold film exposed to 20 ppb mercury.

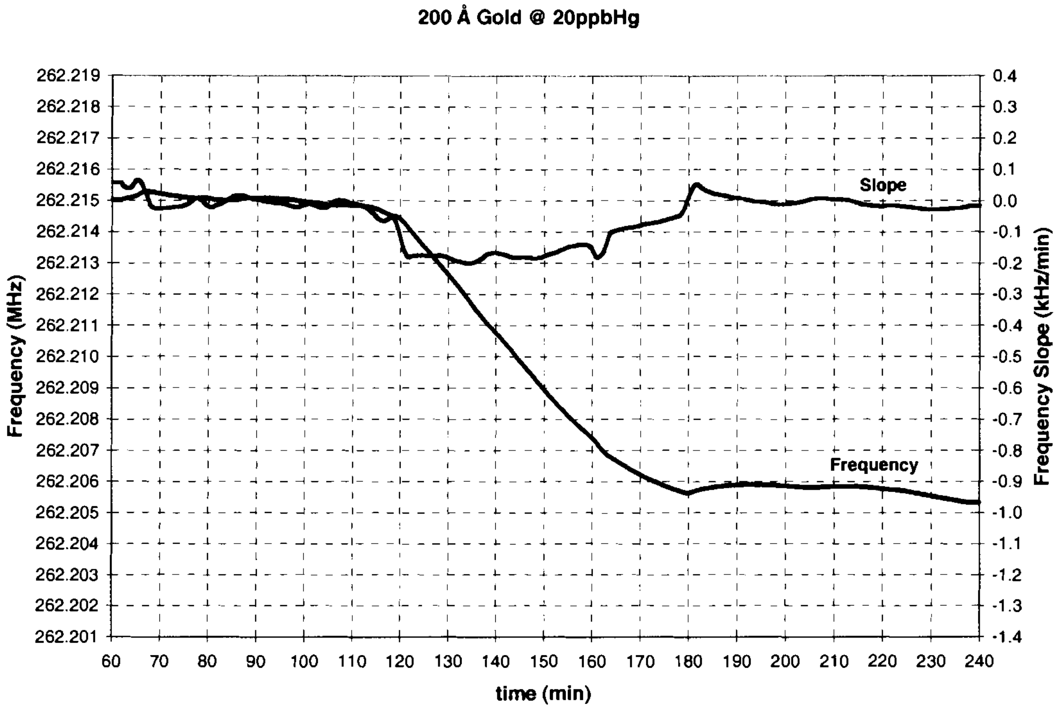

Figure A.5 200 Å gold film exposed to 20 ppb mercury.

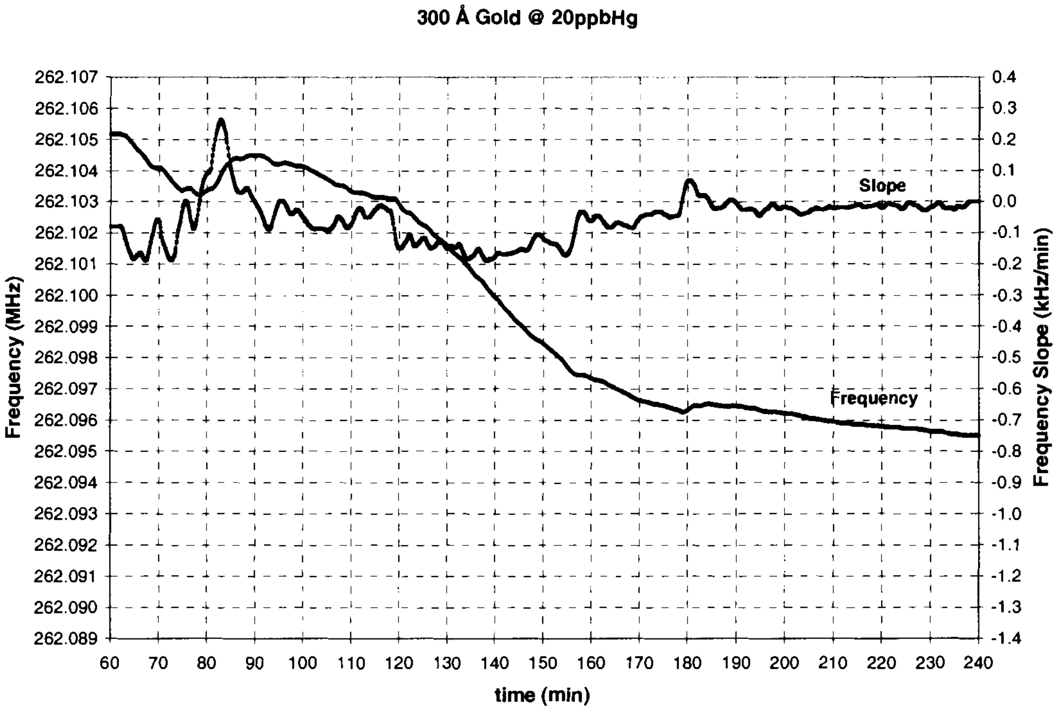

Figure A.6 300 Å gold film exposed to 20 ppb mercury.

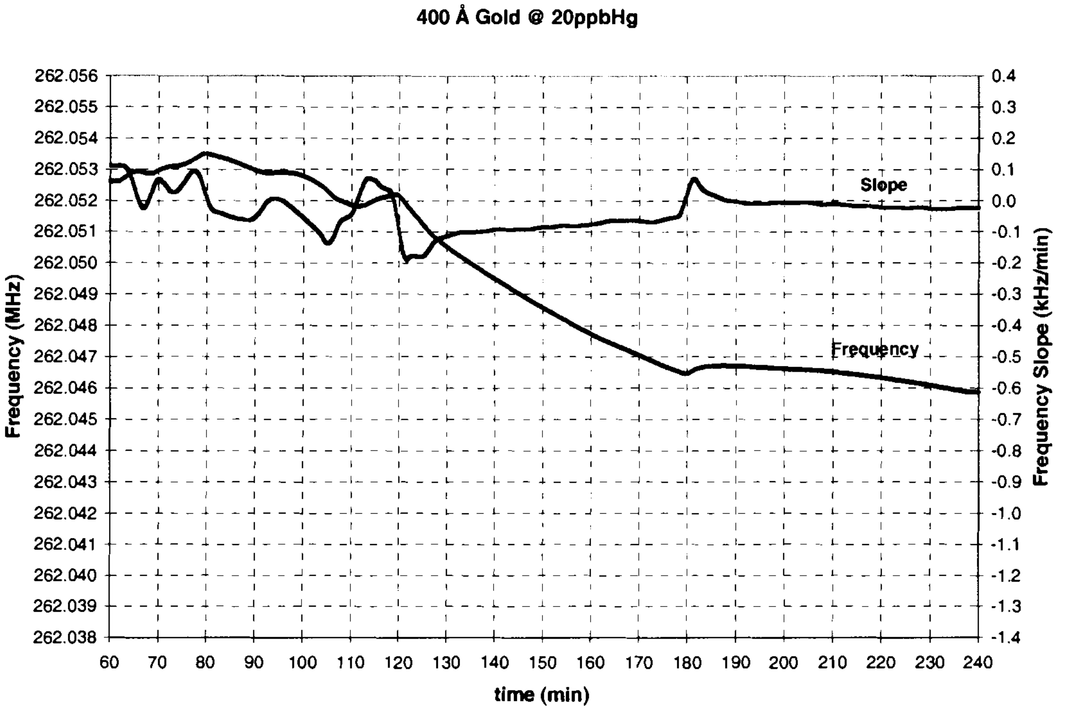

Figure A.7 400 Å gold film exposed to 20 ppb mercury.

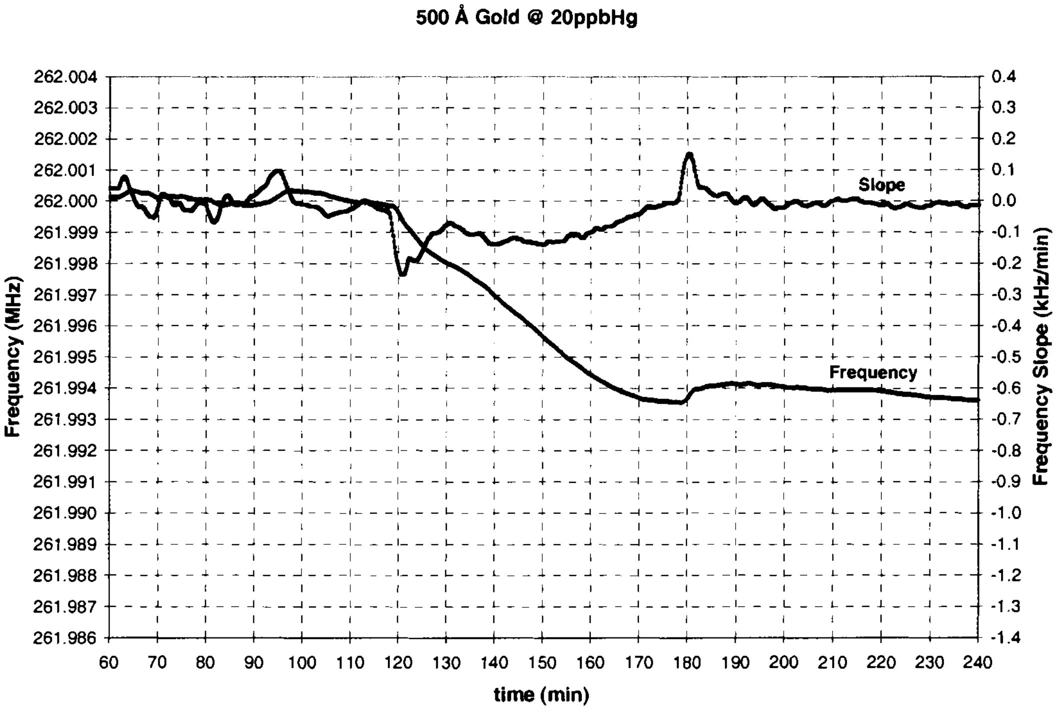

Figure A.8 500 Å gold film exposed to 20 ppb mercury.

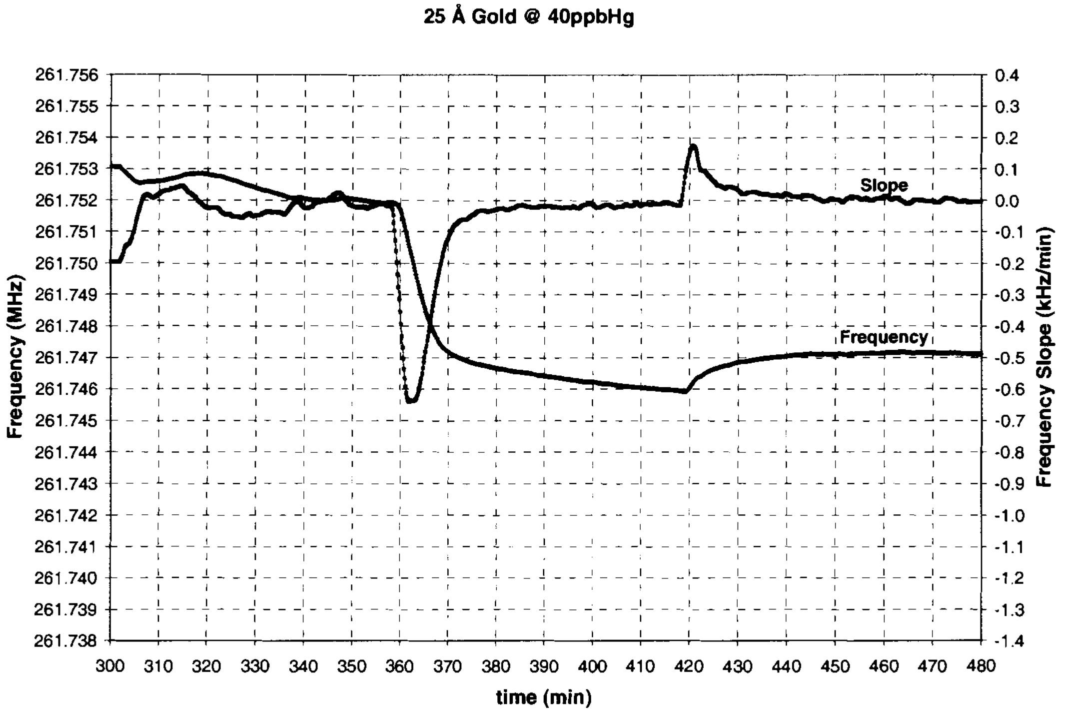

Figure A.9 25 Å gold film exposed to 40 ppb mercury.

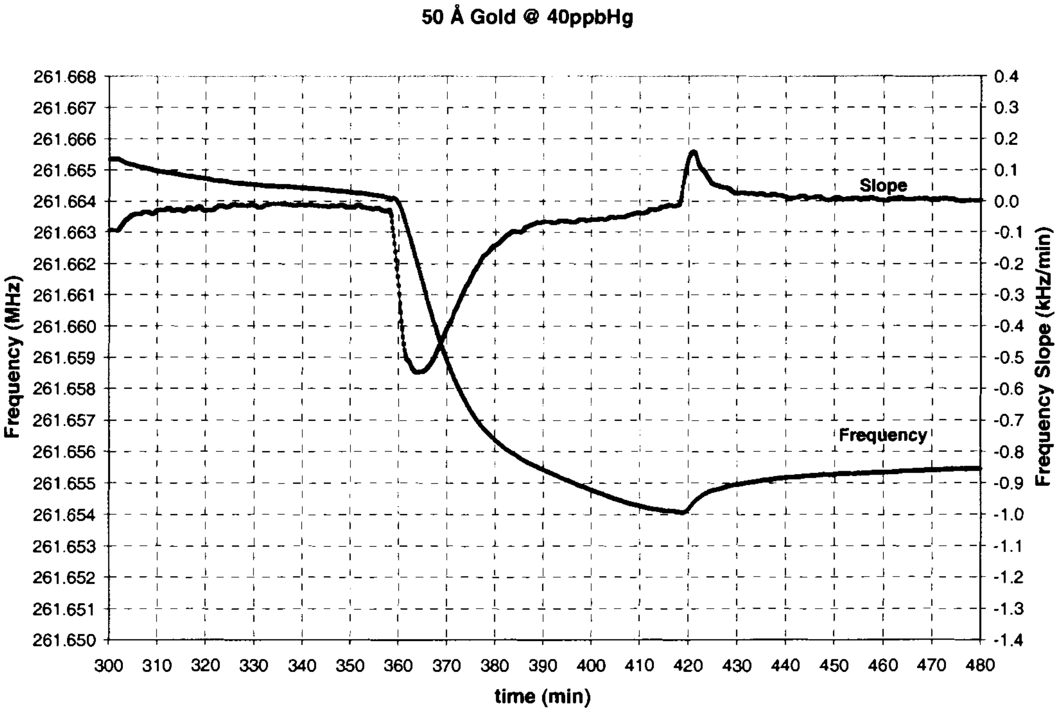

Figure A.10 50 Å gold film exposed to 40 ppb mercury.

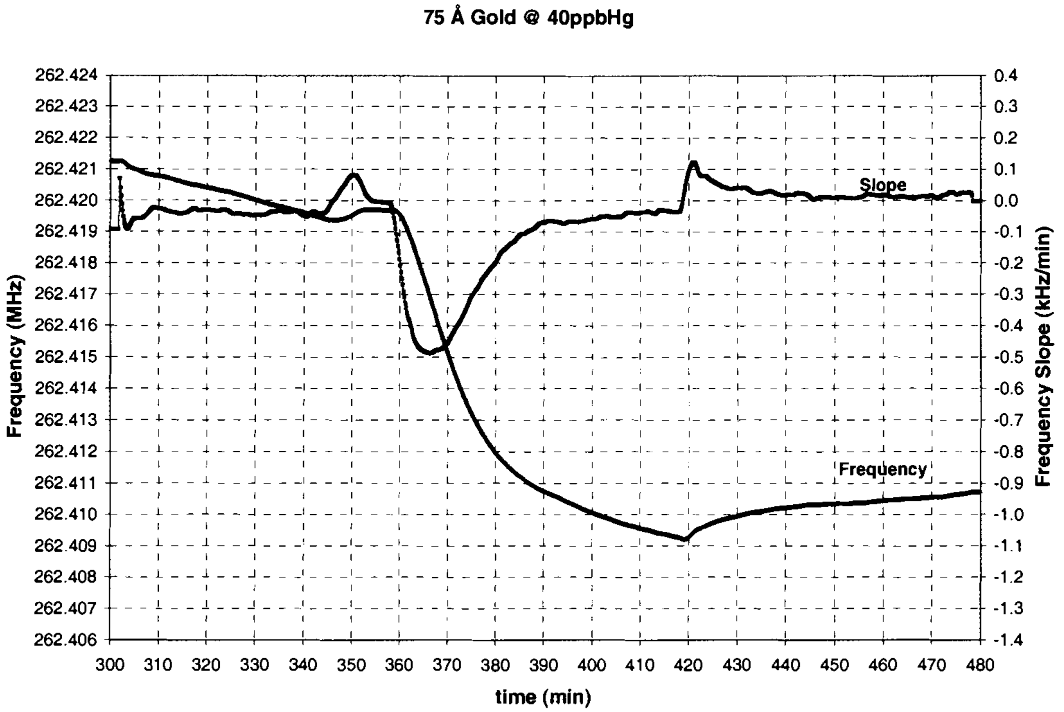

Figure A.11 75 Å gold film exposed to 40 ppb mercury.

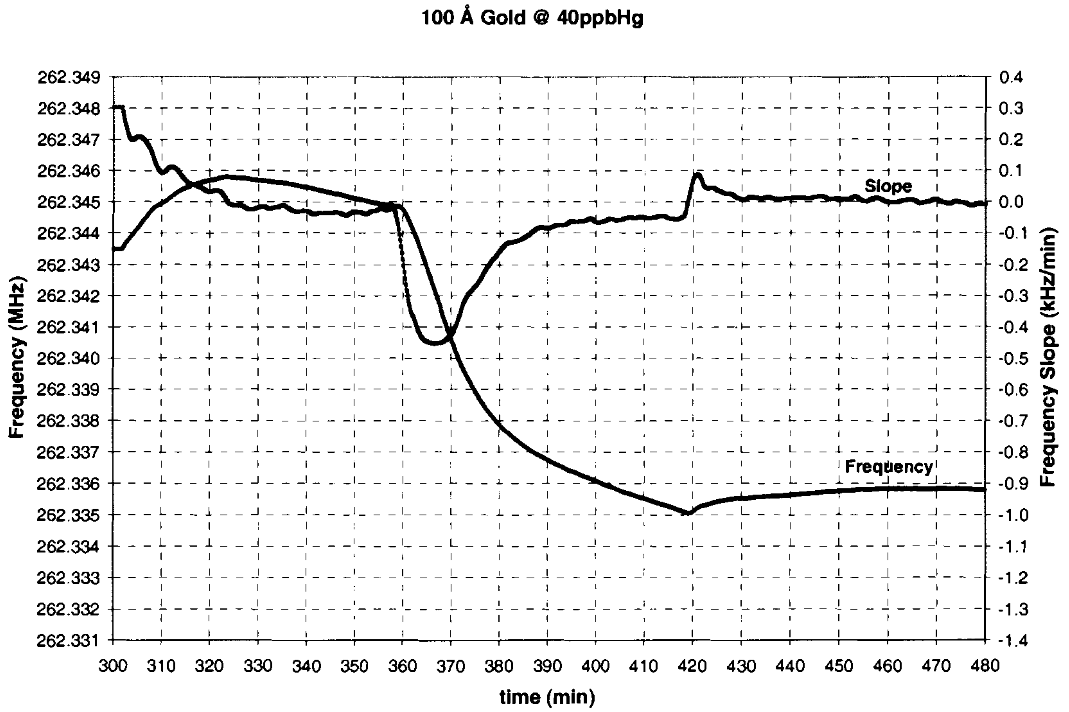

Figure A.12 100 Å gold film exposed to 40 ppb mercury.

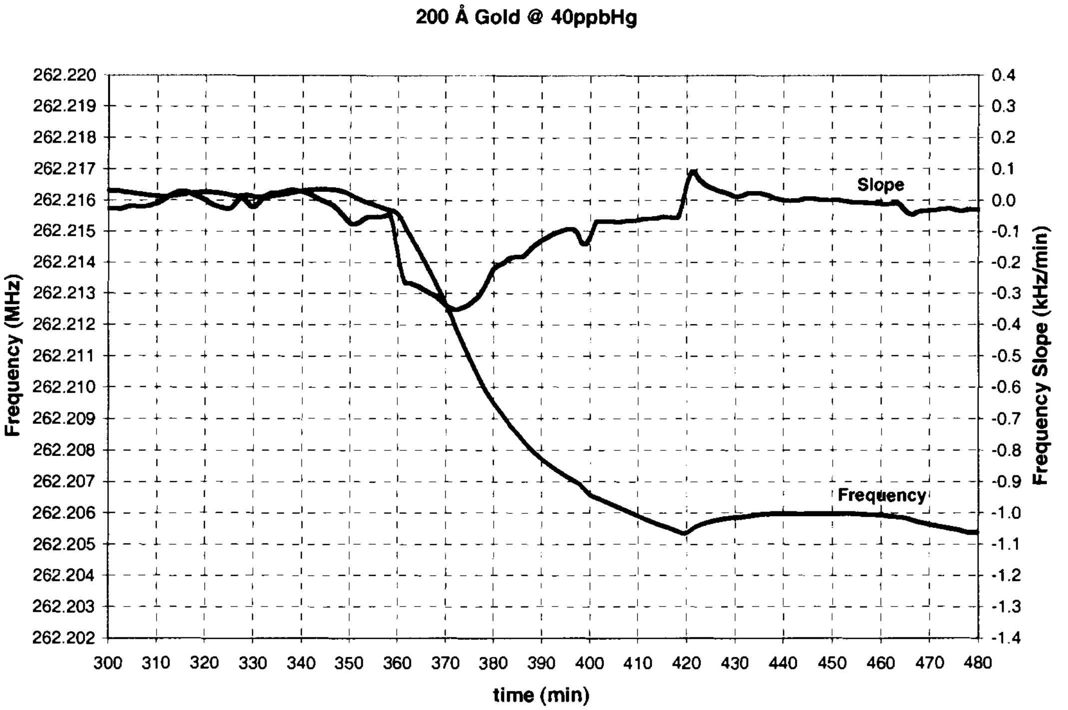

Figure A.13 200 Å gold film exposed to 40 ppb mercury.

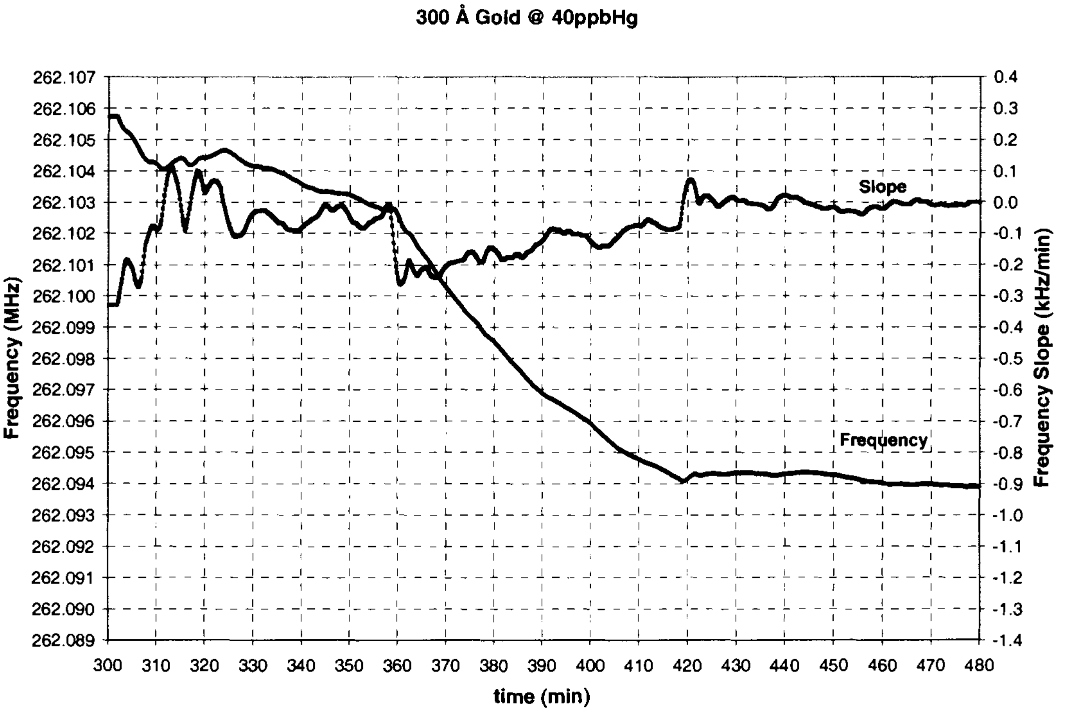

Figure A.14 300 Å gold film exposed to 40 ppb mercury.

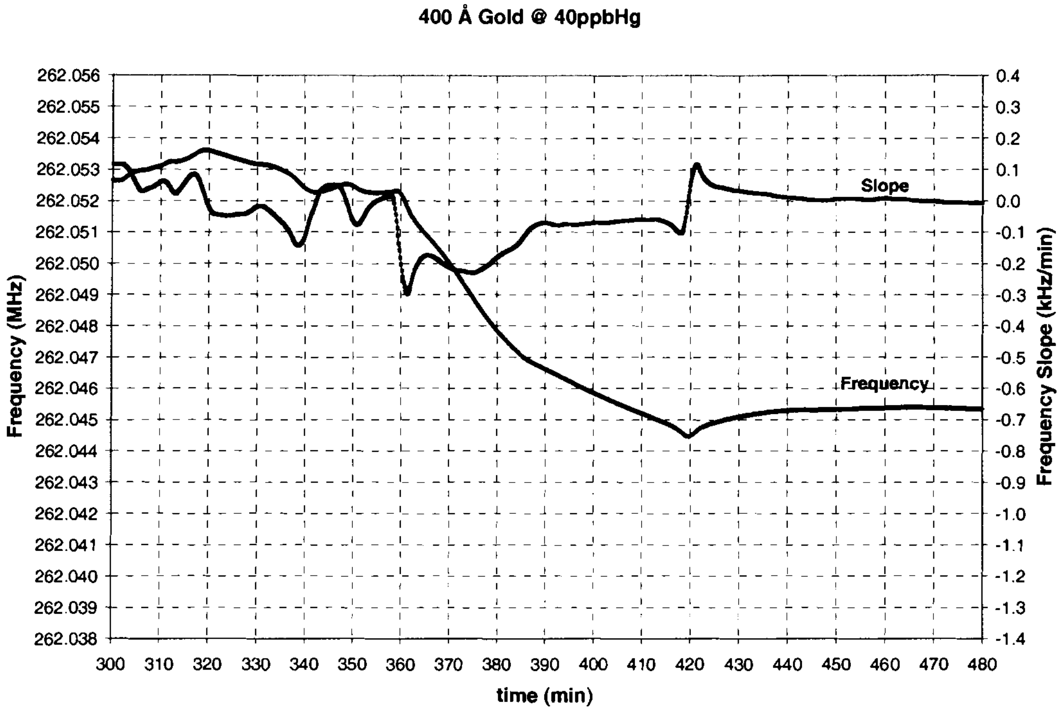

Figure A.15 400 Å gold film exposed to 40 ppb mercury.

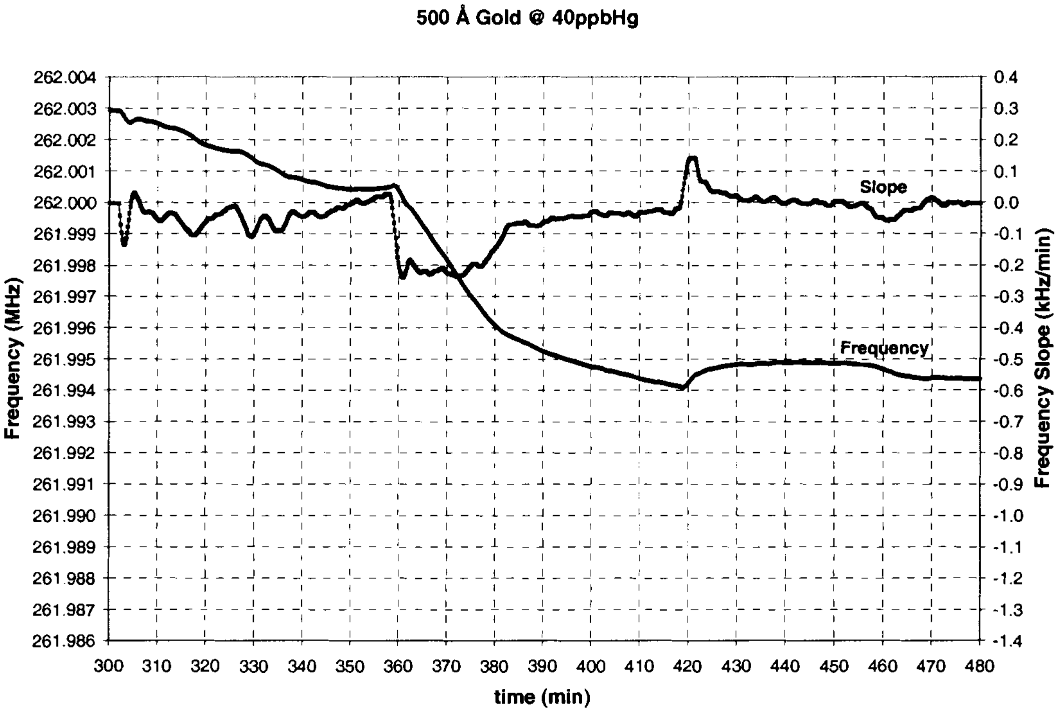

Figure A.16 500 Å gold film exposed to 40 ppb mercury.

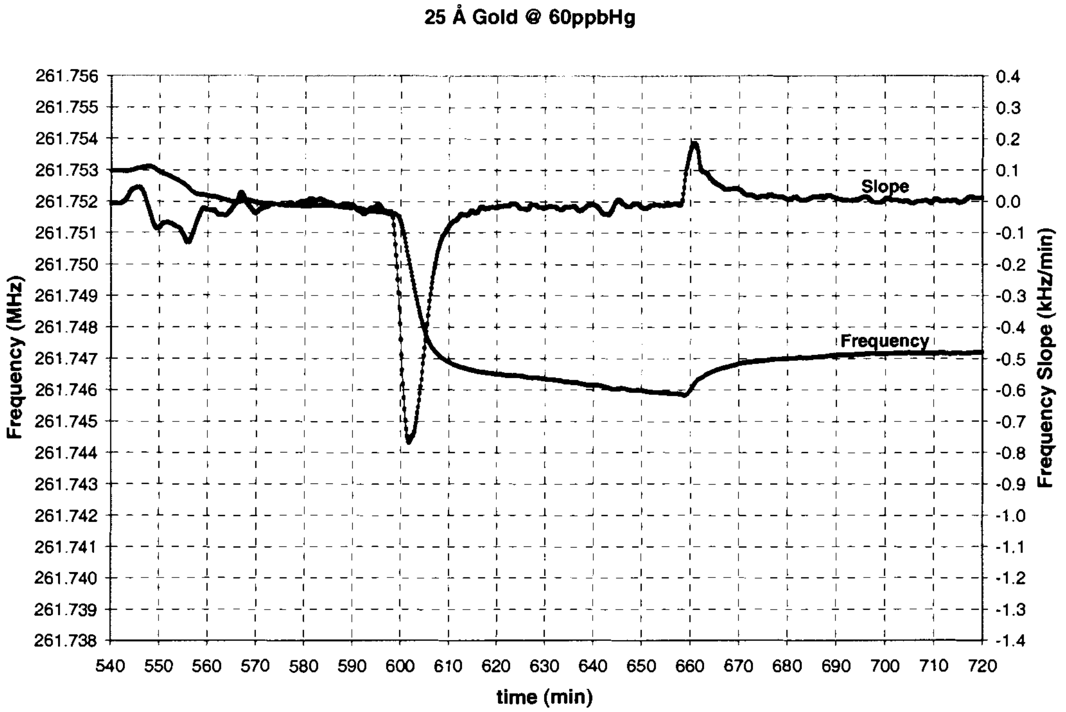

Figure A.17 25 Å gold film exposed to 60 ppb mercury.

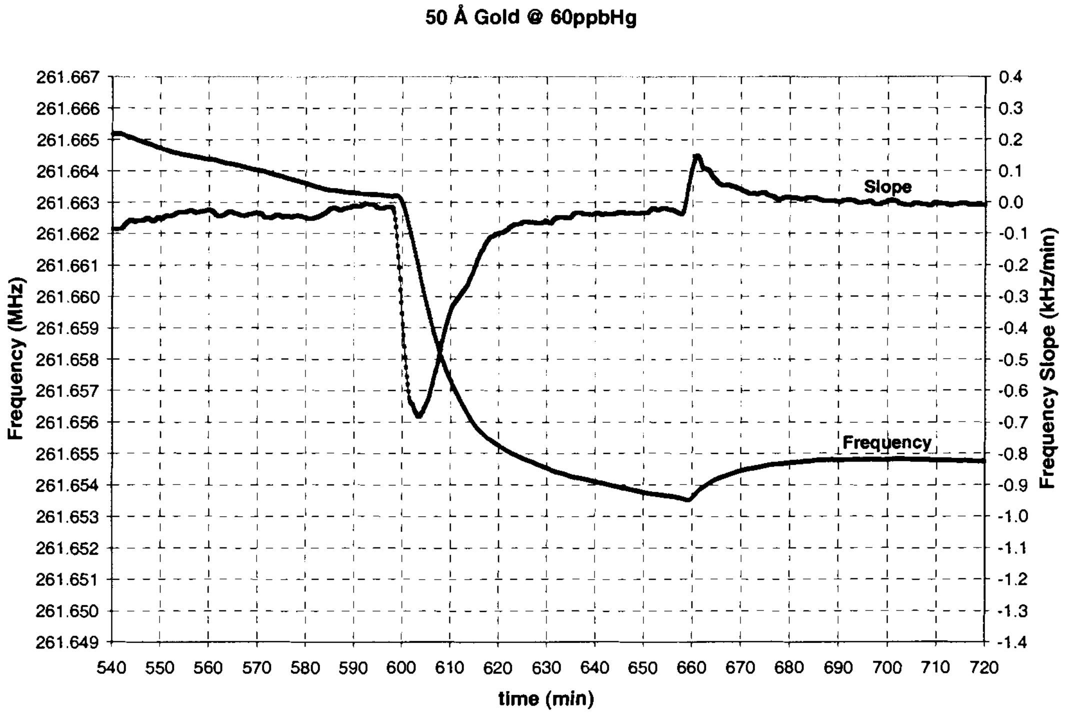

Figure A.18 50 Å gold film exposed to 60 ppb mercury.

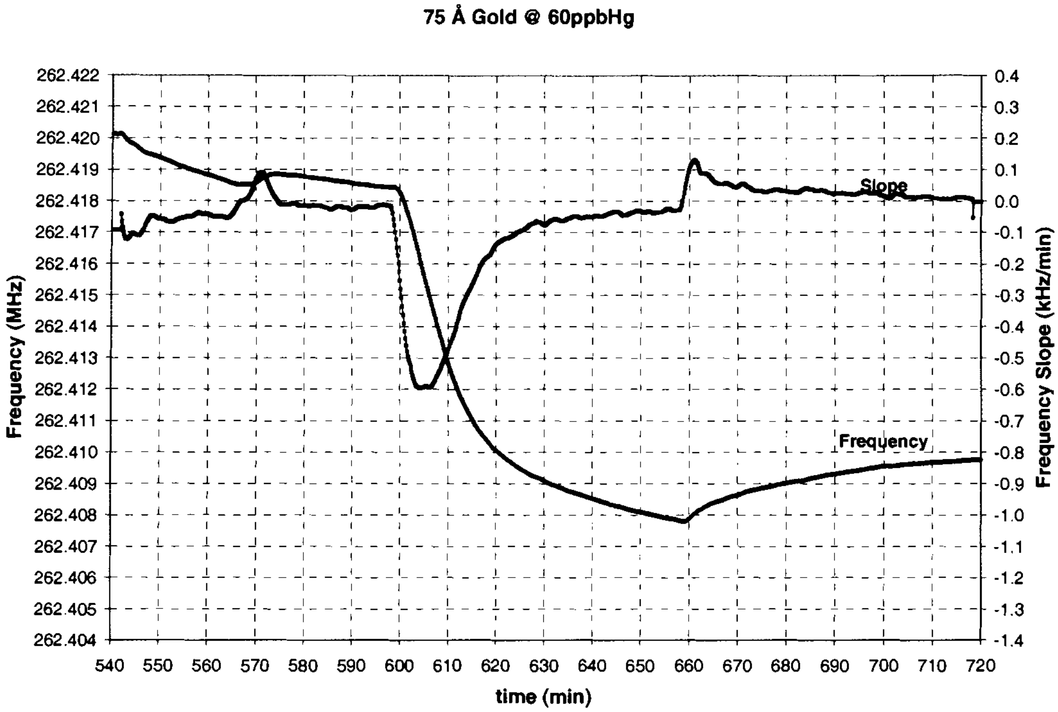

Figure A.19 75 Å gold film exposed to 60 ppb mercury.

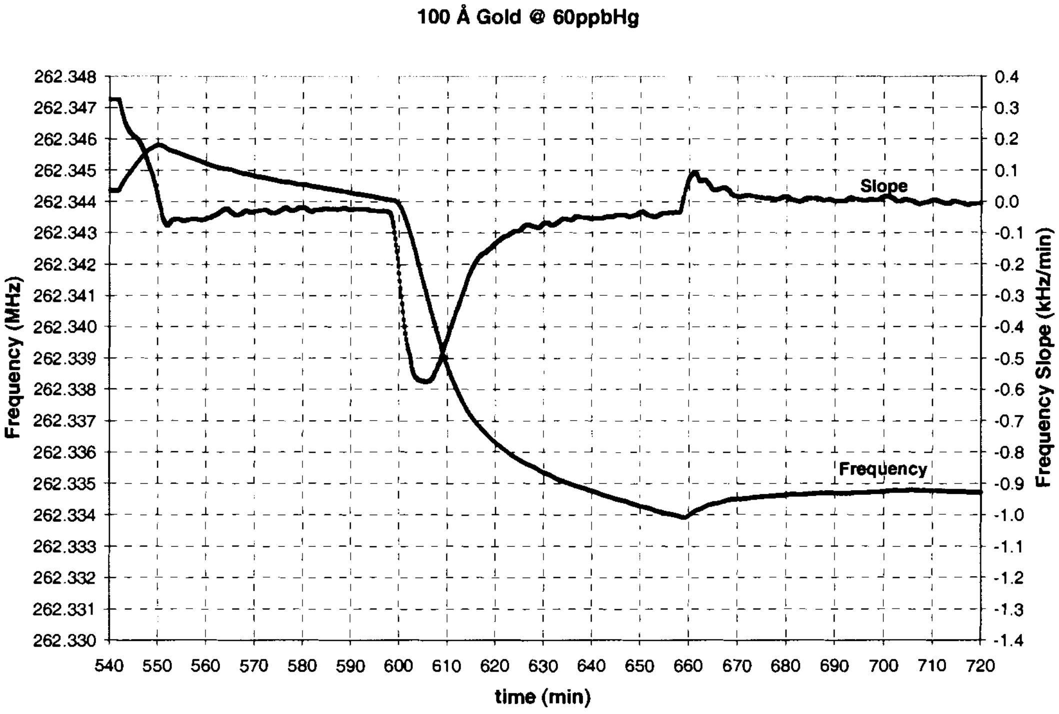

Figure A.20 100 Å gold film exposed to 60 ppb mercury.

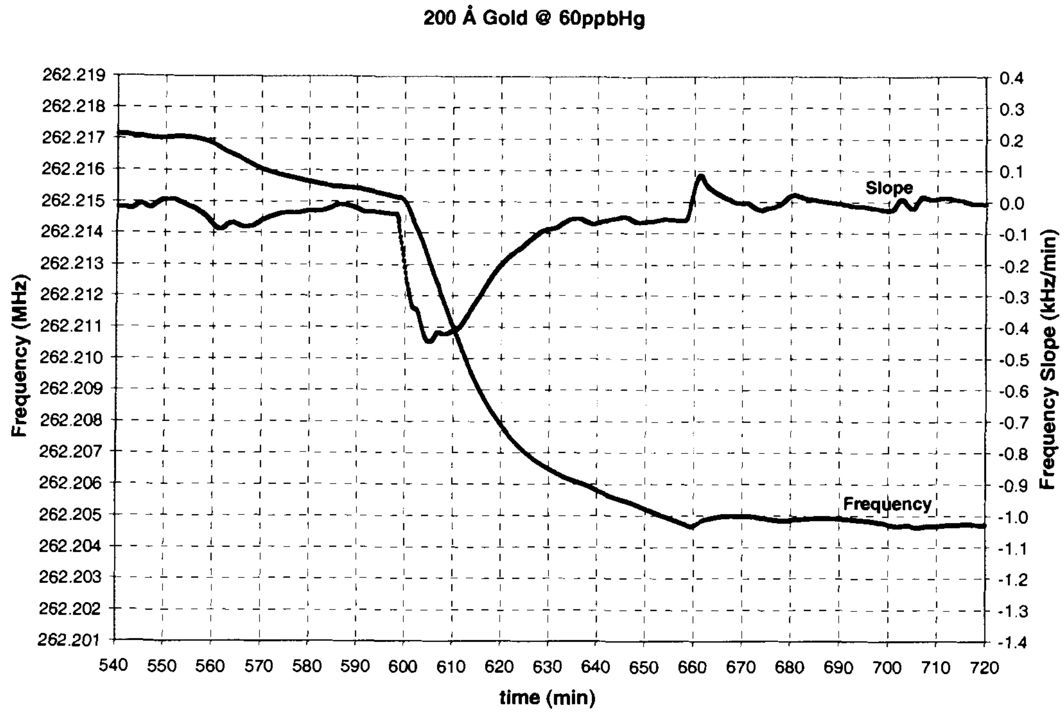

Figure A.21 200 Å gold film exposed to 60 ppb mercury.

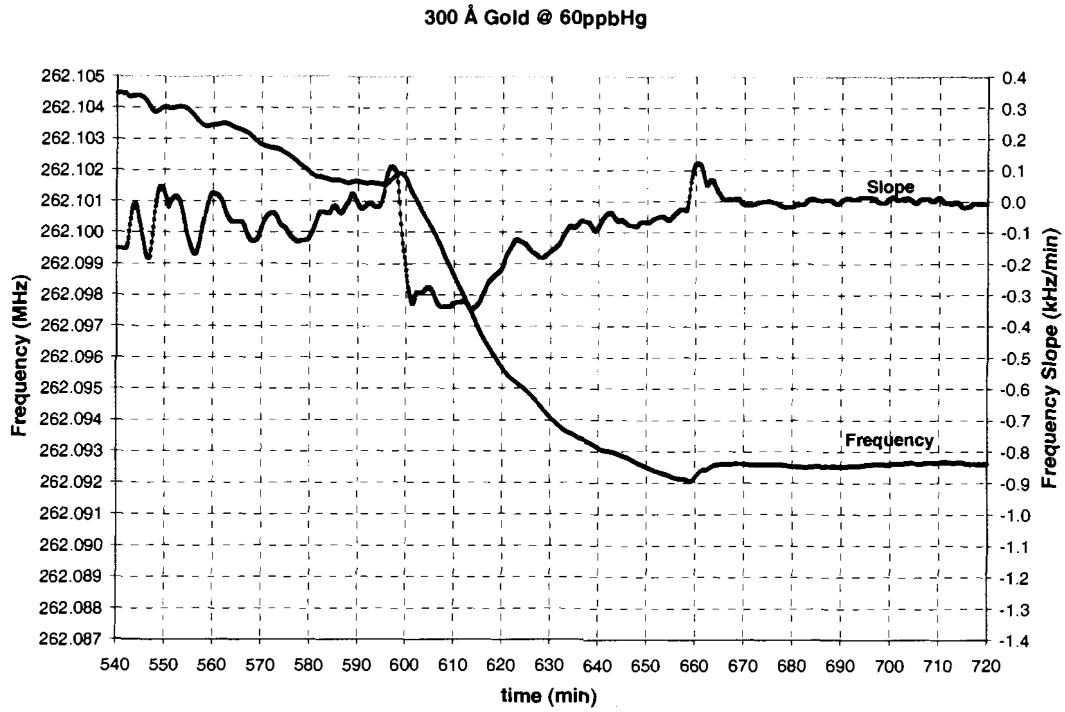

Figure A.22 300 Å gold film exposed to 60 ppb mercury.

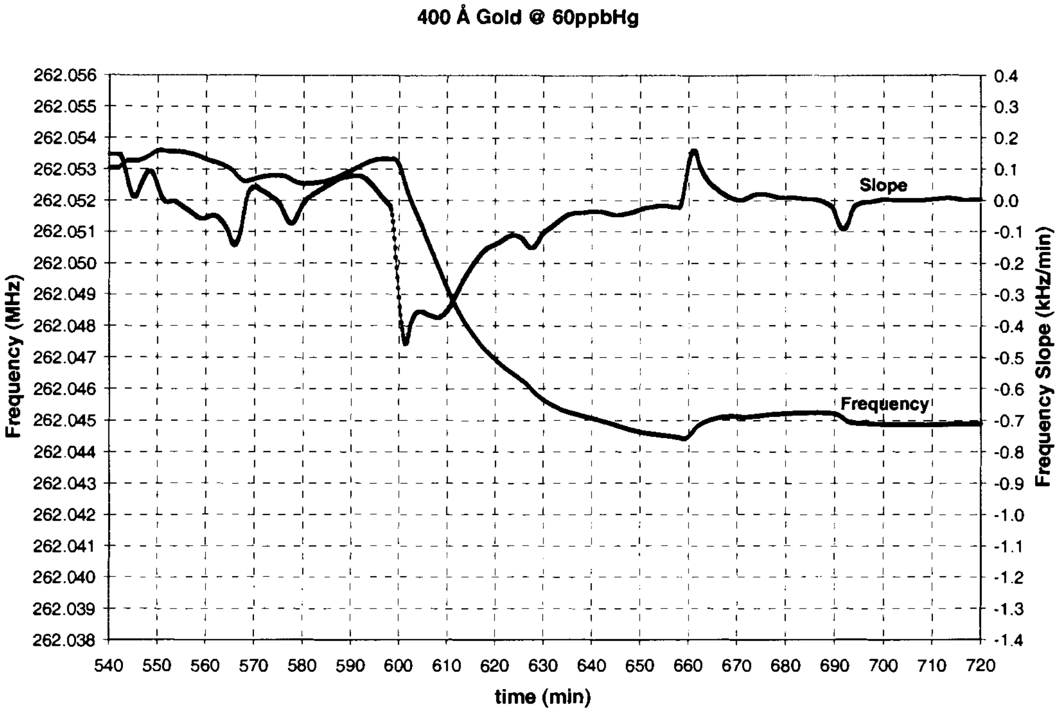

Figure A.23 400 Å gold film exposed to 60 ppb mercury.

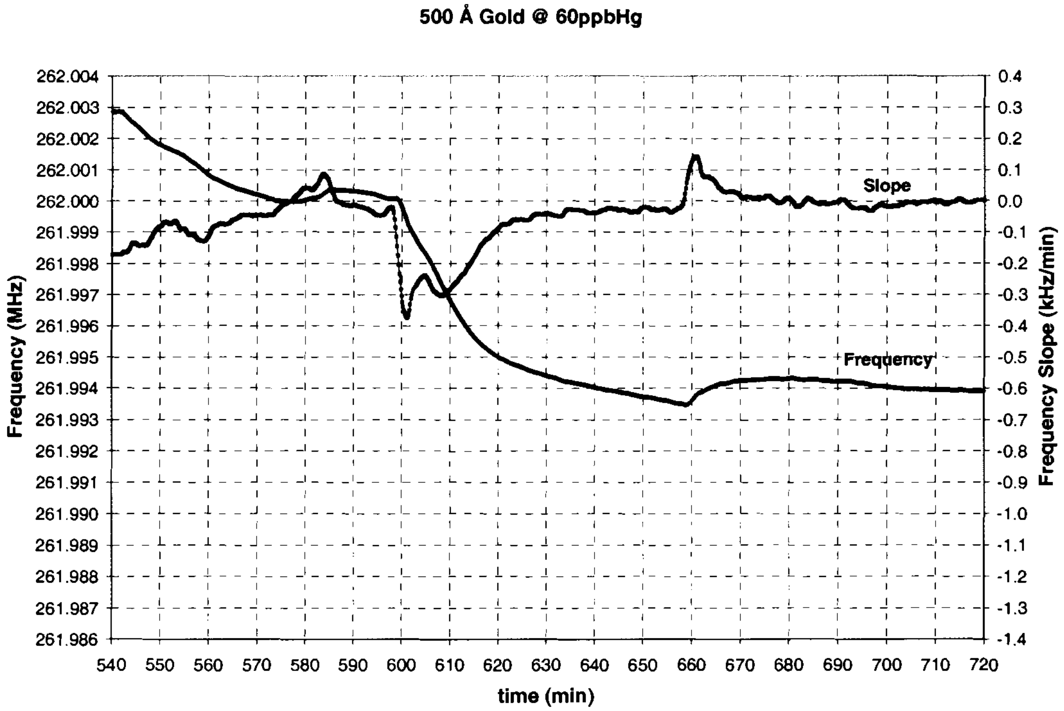

Figure A.24 500 Å gold film exposed to 60 ppb mercury.

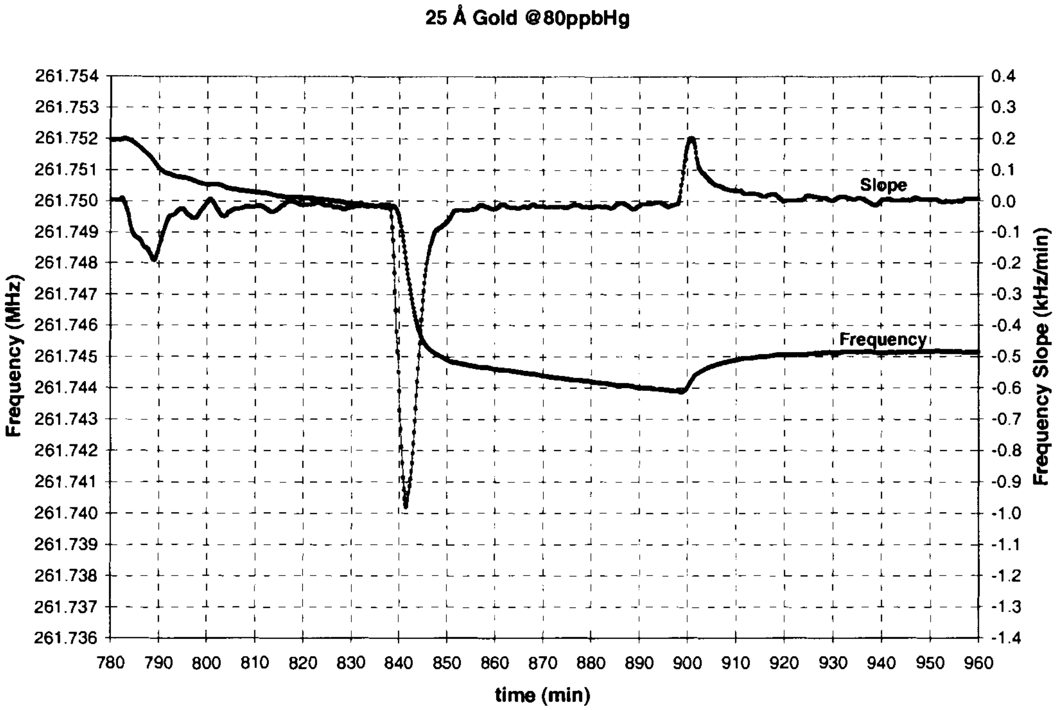

Figure A.25 25 Å gold film exposed to 80 ppb mercury.

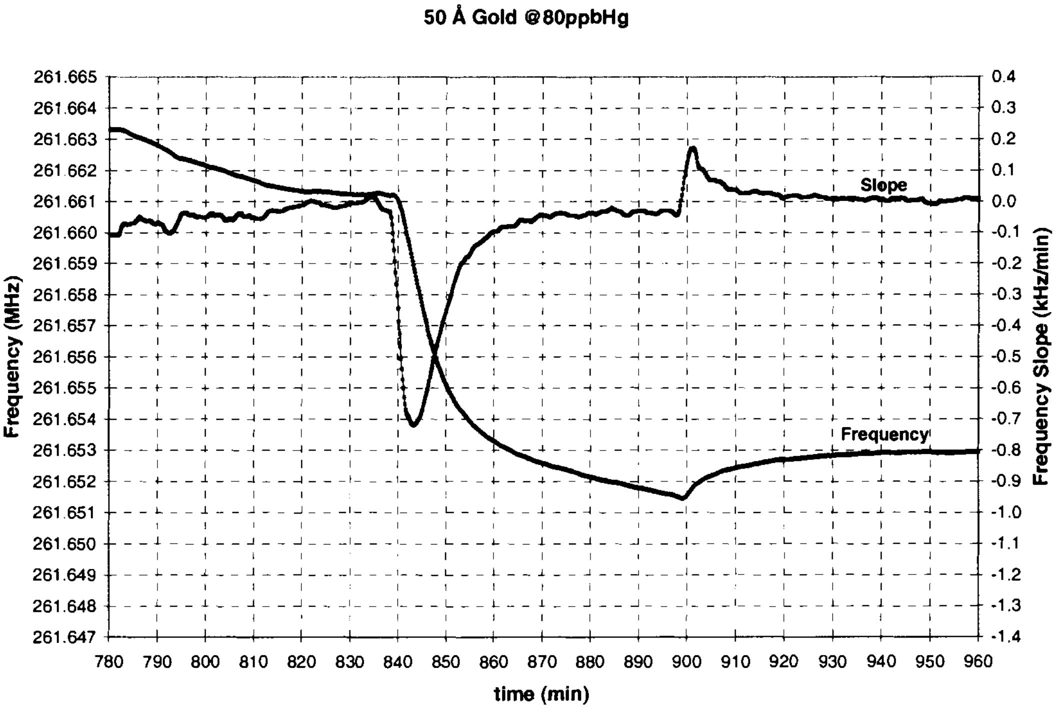

Figure A.26 50 Å gold film exposed to 80 ppb mercury.

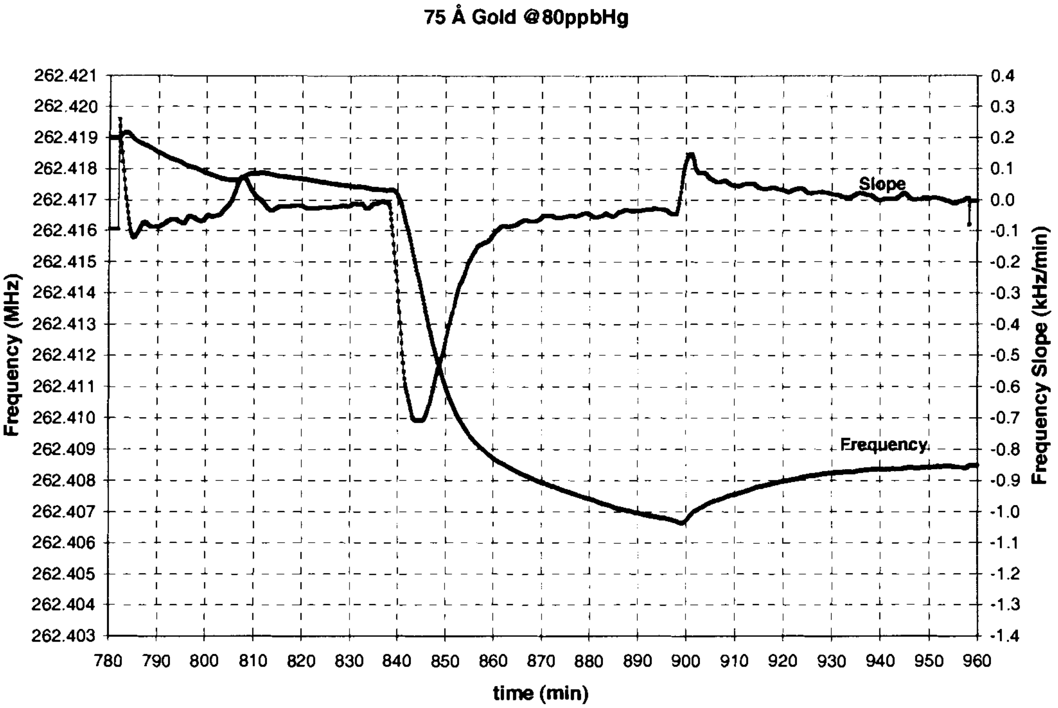

Figure A.27 75 Å gold film exposed to 80 ppb mercury.

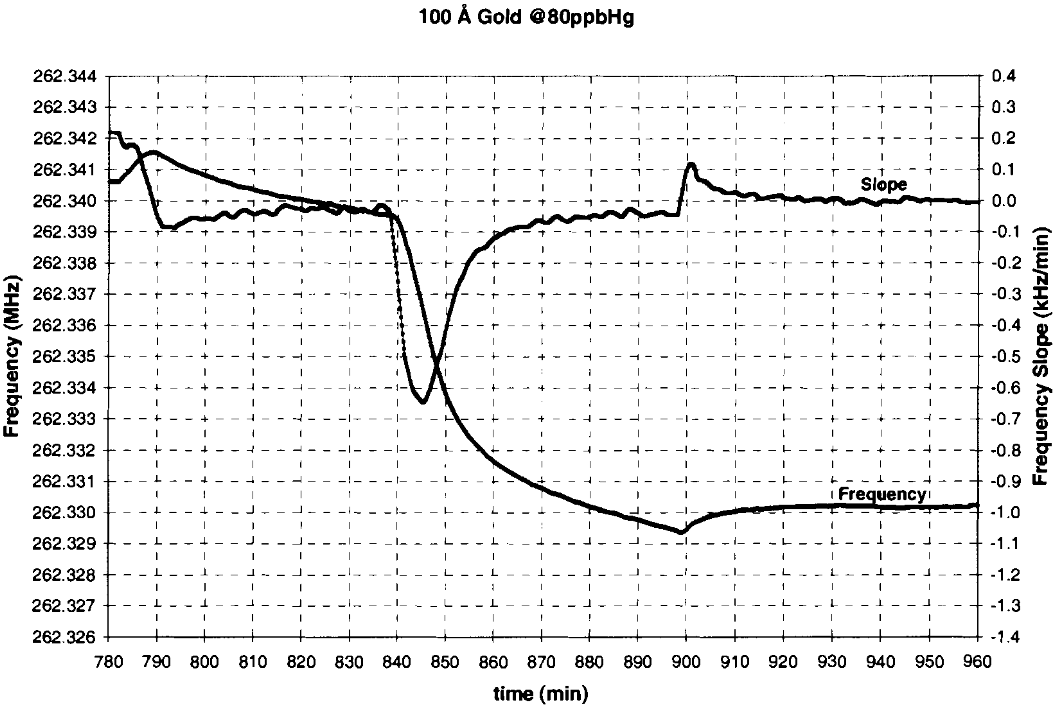

Figure A.28 100 Å gold film exposed to 80 ppb mercury.

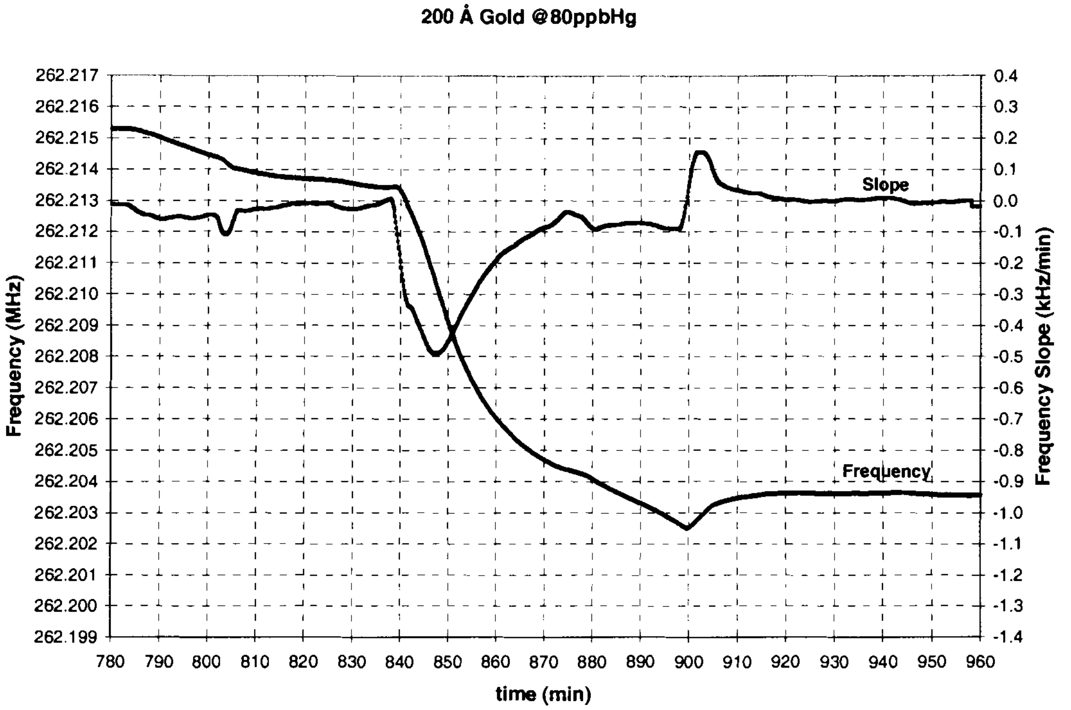

Figure A.29 200 Å gold film exposed to 80 ppb mercury.

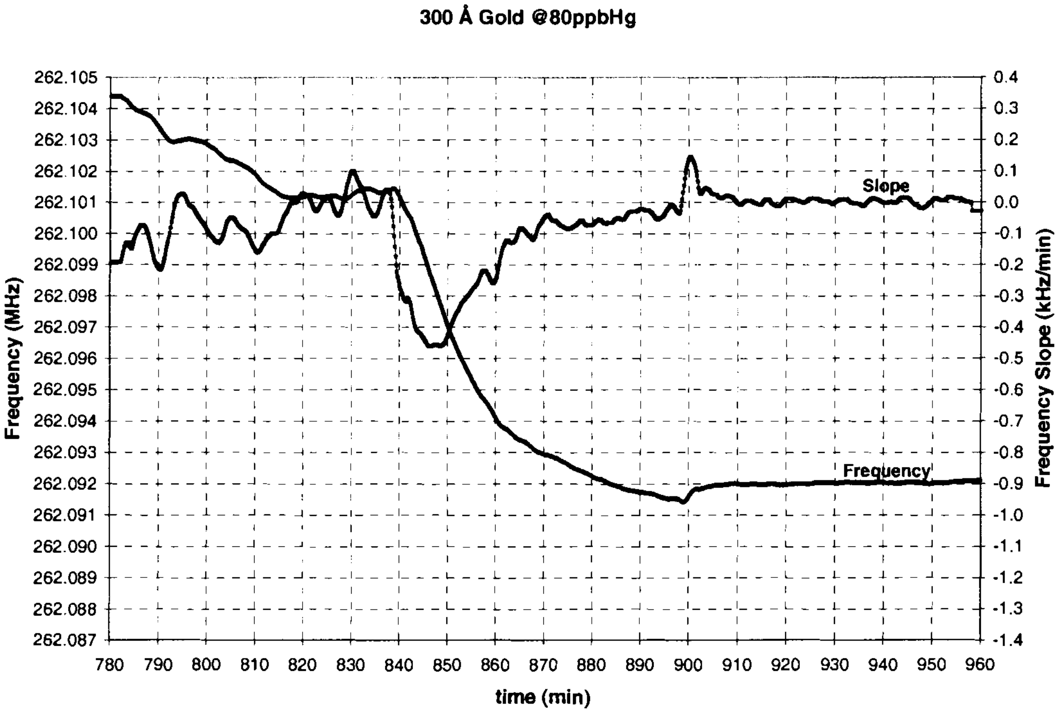

Figure A.30 300 Å gold film exposed to 80 ppb mercury.

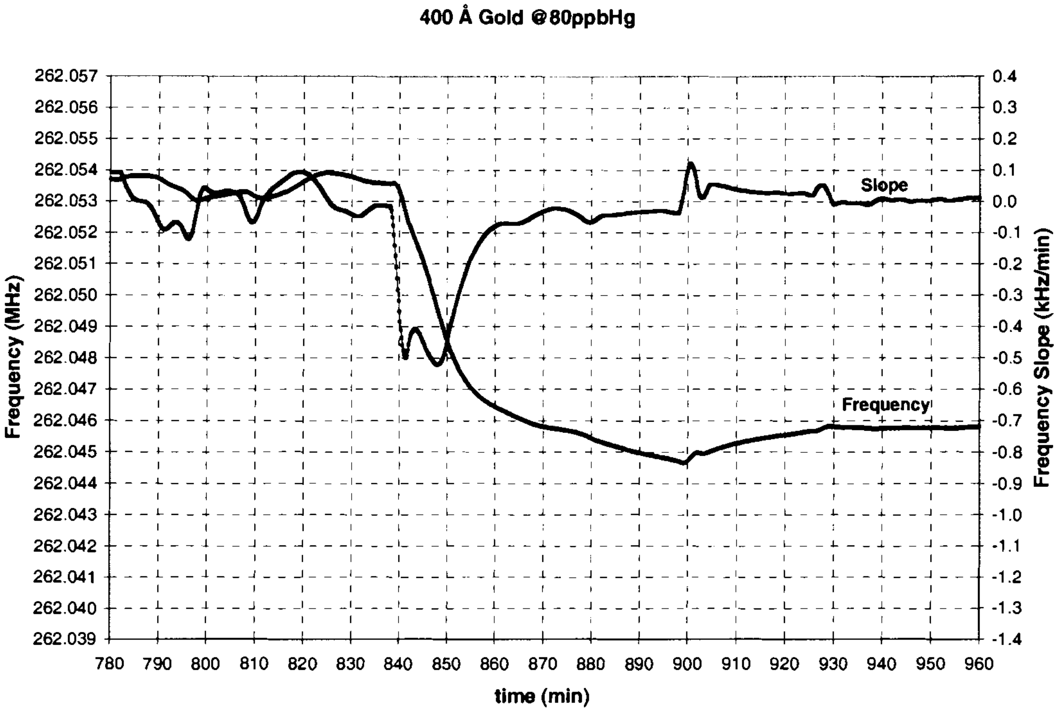

Figure A.31 400 Å gold film exposed to 80 ppb mercury.

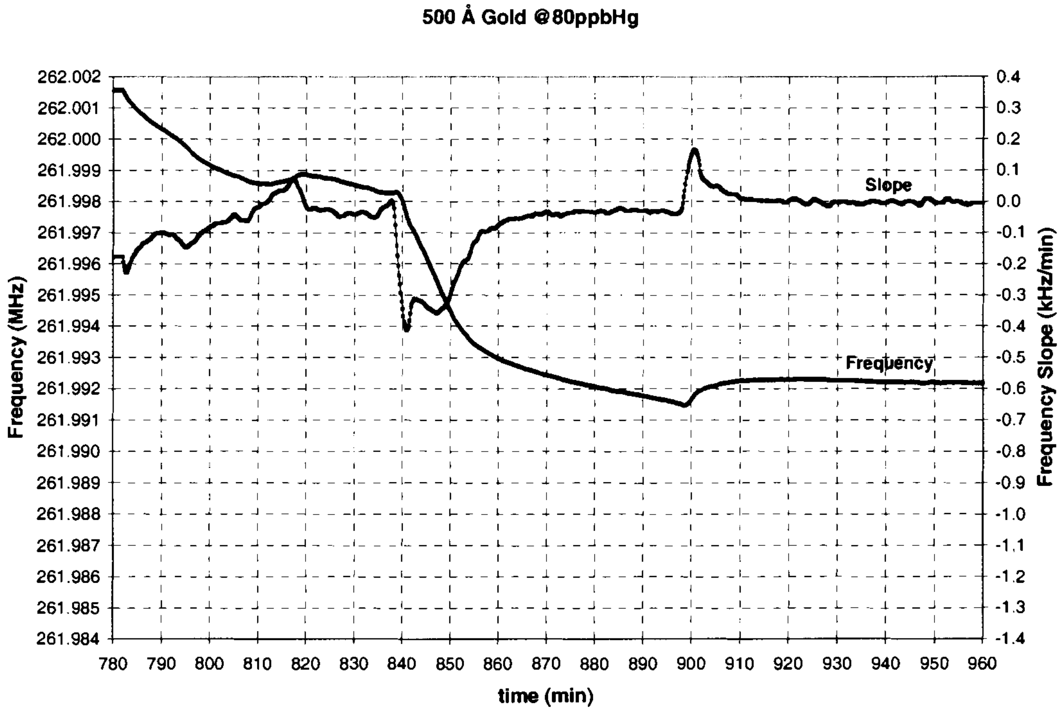

Figure A.32 500 Å gold film exposed to 80 ppb mercury.

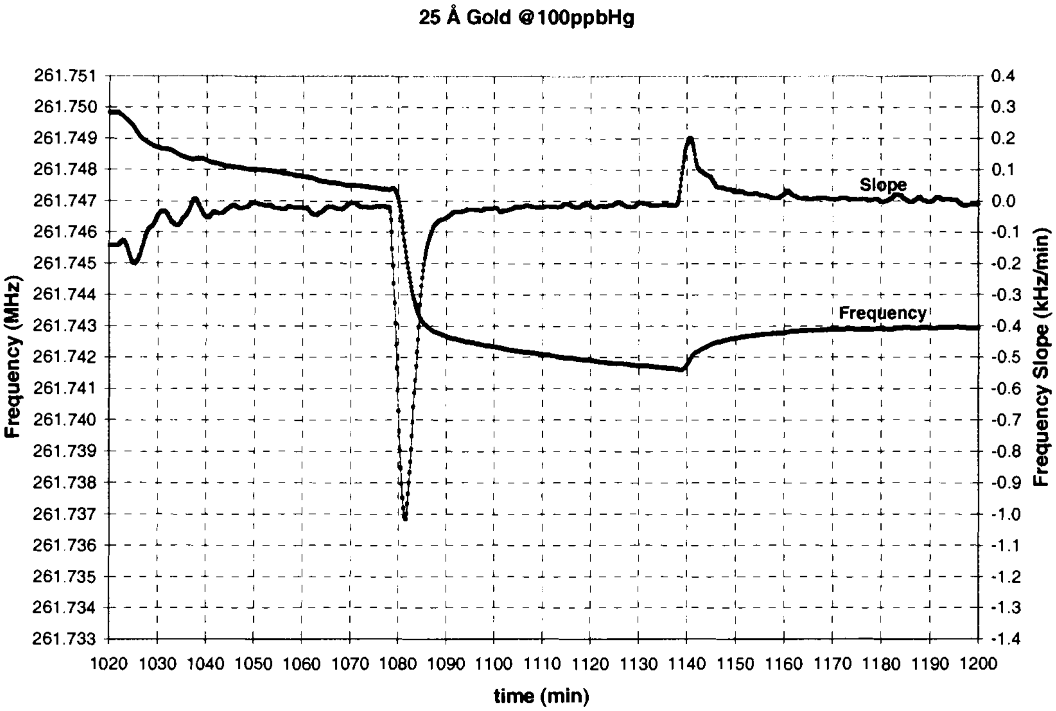

Figure A.33 25 Å gold film exposed to 100 ppb mercury.

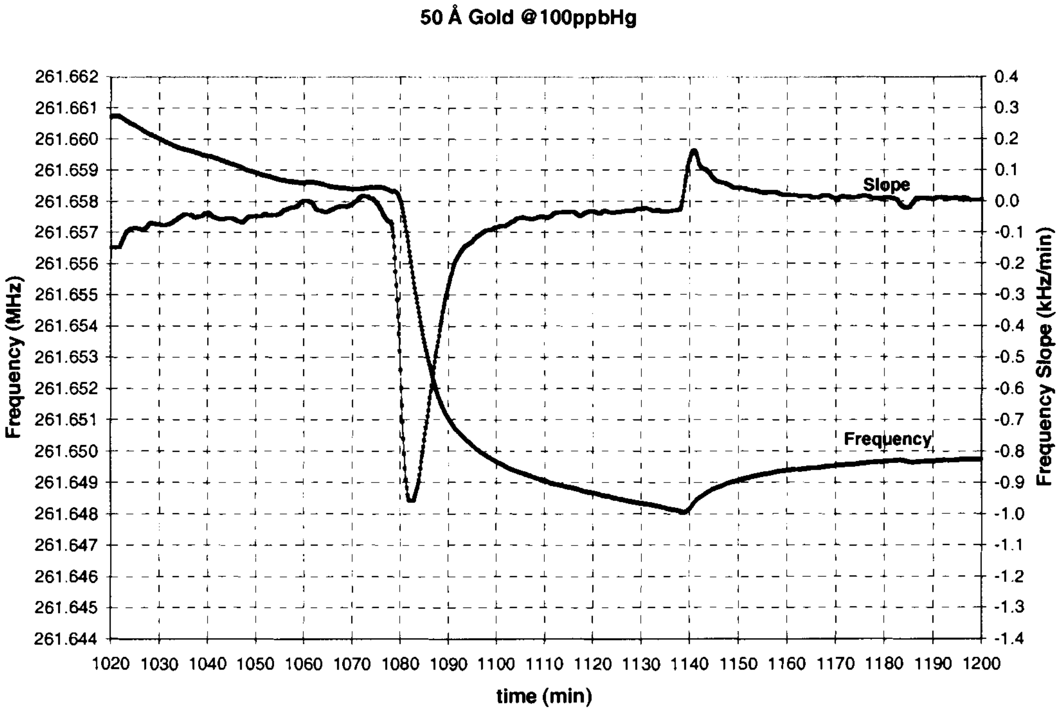

Figure A.34 50 Å gold film exposed to 100 ppb mercury.

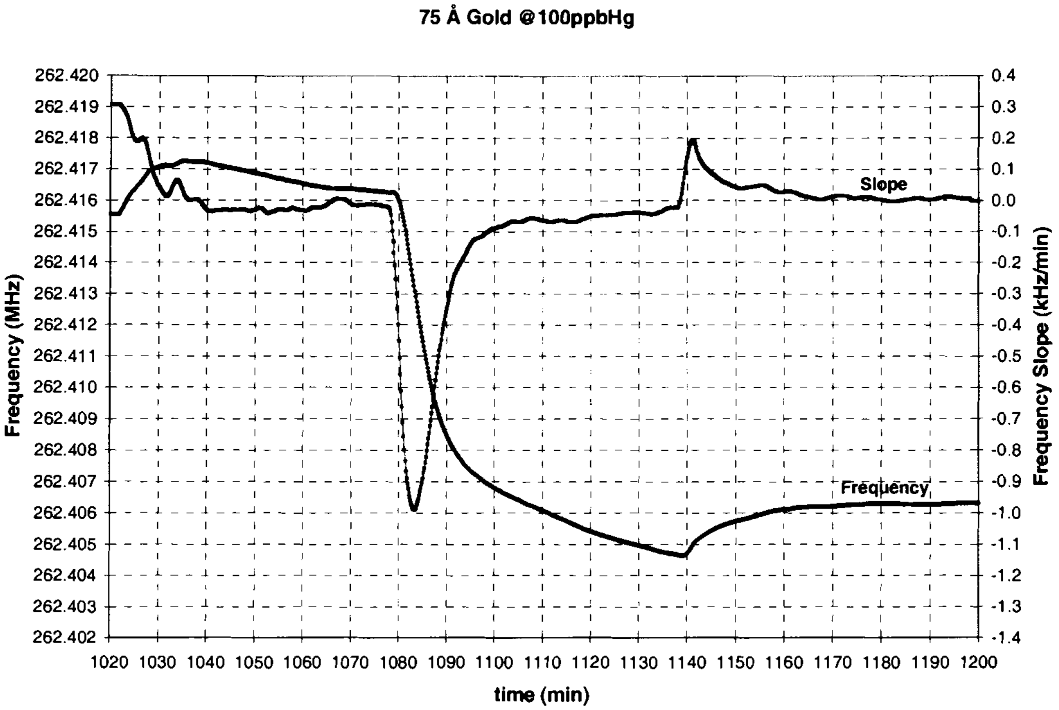

Figure A.35 75 Å gold film exposed to 100 ppb mercury.

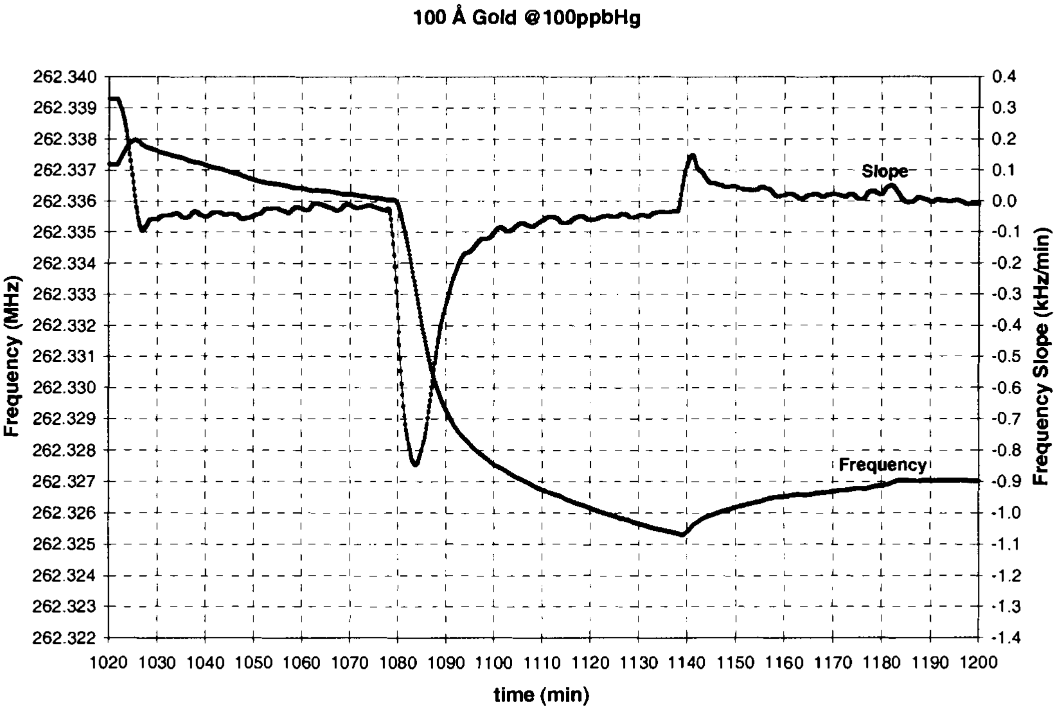

Figure A.36 100 Å gold film exposed to 100 ppb mercury.

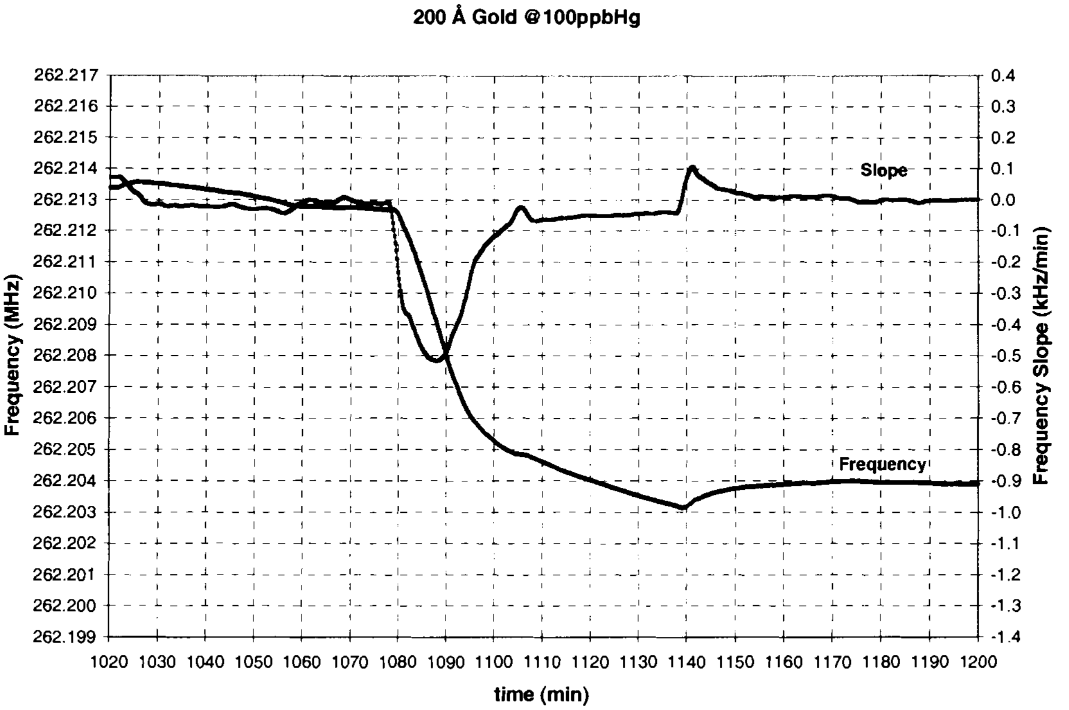

Figure A.37 200 Å gold film exposed to 100 ppb mercury.

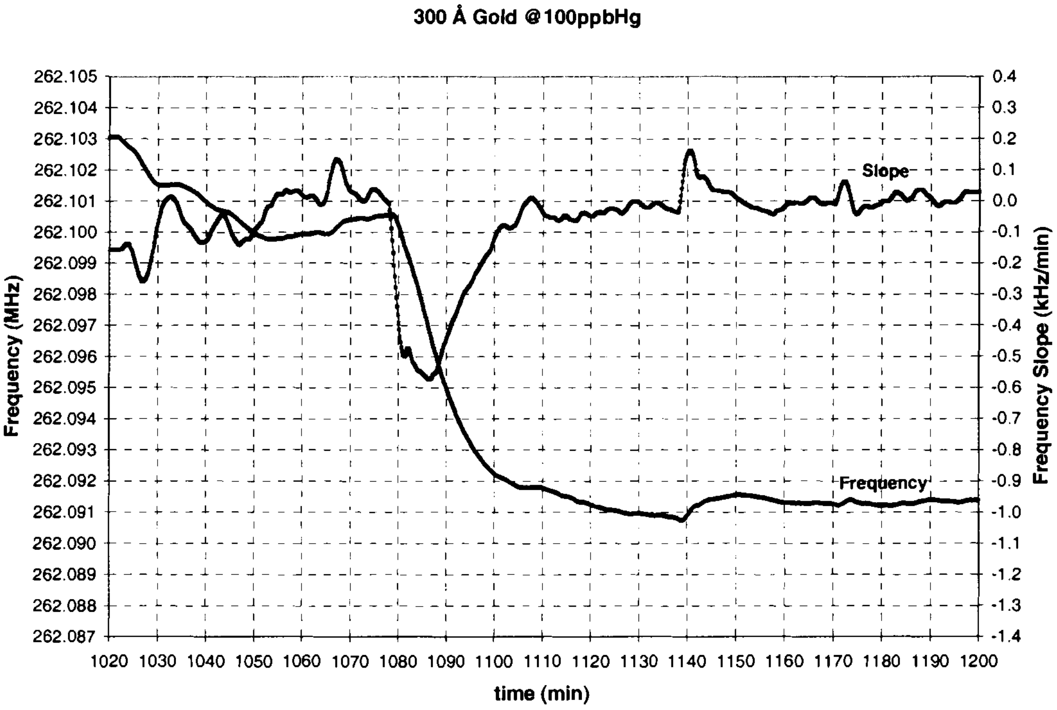

Figure A.38 300 Å gold film exposed to 100 ppb mercury.

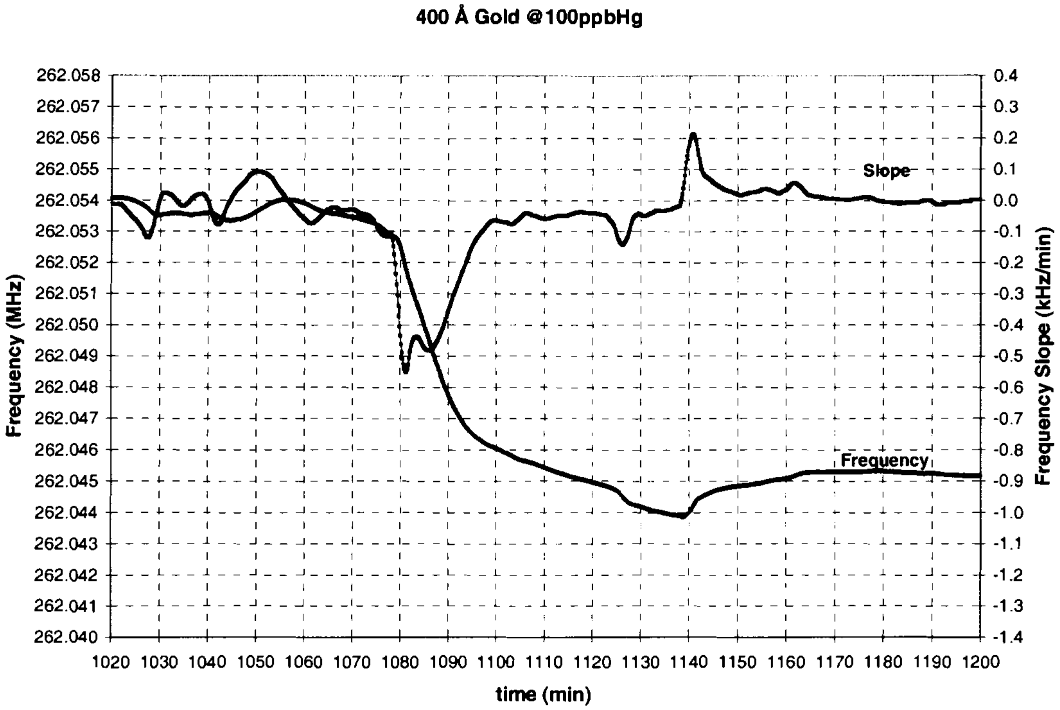

Figure A.39 400 Å gold film exposed to 100 ppb mercury.

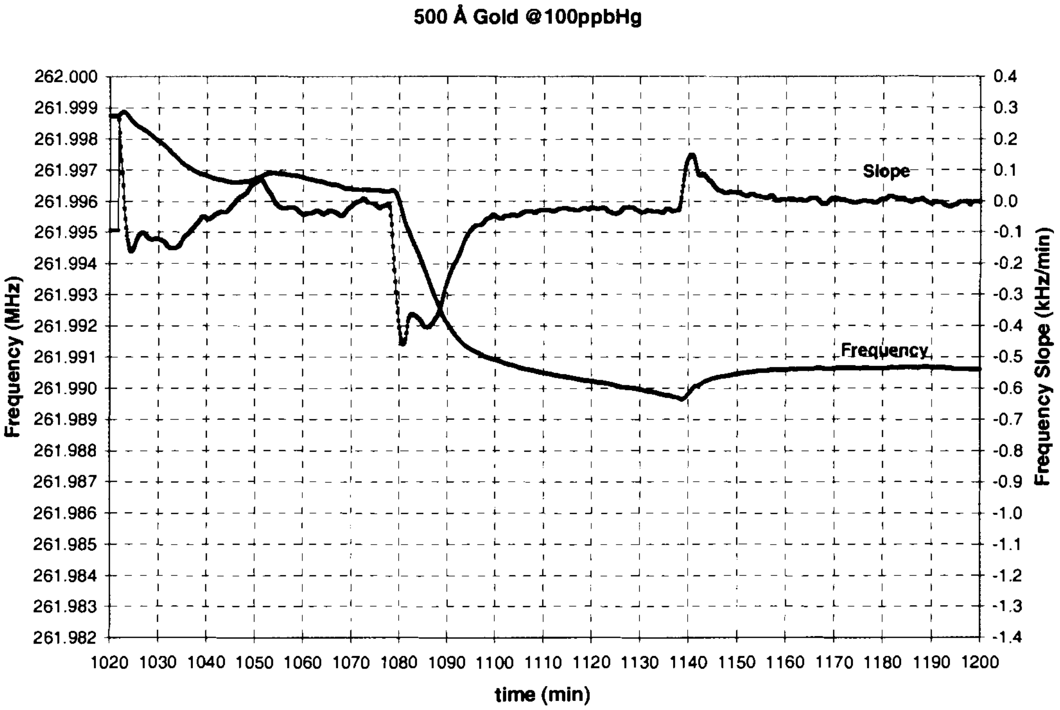

Figure A.40 500 Å gold film exposed to 100 ppb mercury.

BIOGRAPHY OF THE AUTHOR

Reichl B. Haskell was born at Fort Meade, Maryland on January 29, 1973. He attended public schools in Frankfort and Searsport, Maine and graduated from Searsport District High School in 1991.

He went to college at the University of Maine and graduated with a Bachelor of Science degree in Electrical Engineering Technology in 1997. While in school, he began working for Sensor Research and Development Corporation as a research engineer in the area of microelectronic sensors. He continued his education at the University of Maine. He is currently employed by Vectron International as a crystal process and design engineer. Reichl is a candidate for the Master of Science degree in Electrical Engineering from The University of Maine in August 2003.